

NANOFLUID THERMAL CONDUCTIVITY

“A THERMO-MECHANICAL, CHEMICAL STRUCTURE AND COMPUTATIONAL APPROACH”

by

Angelos Yiannou

A thesis submitted to the

University of Pretoria

in partial fulfilment of the requirements

for the degree of

MASTER OF ENGINEERING

in

Mechanical and Aeronautical Engineering

Supervisor: Prof Johan F.M. Slabber

Department of Mechanical and Aeronautical Engineering

University of Pretoria

Co-supervisor: Prof Josua P. Meyer

Department of Mechanical and Aeronautical Engineering

University of Pretoria

Co-supervisor: Dr Jan A. Pretorius

Department of Chemistry (Computational Chemistry)

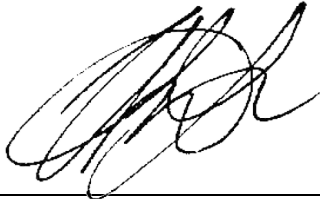
and

Centre for the Advancement of Scholarship

University of Pretoria

January 2015

I, Angelos Yiannou, student number 28095962, declare that this thesis, which I hereby submit for the degree of Master of Philosophy in Mechanical and Aeronautical Engineering at the University of Pretoria, is my own work and has not been previously submitted by me for a degree at this or any other tertiary institution.



Angelos Yiannou

Date:

ACKNOWLEDGEMENTS

To my family:

I would like to thank my mother and father, who have supported me and believed in me throughout my education. May I make you proud. I would also like to thank my brother, for bragging on my behalf!

Prof Johan Slabber (Mechanical and Aeronautical Engineering Department, UP):

I would like to thank Prof Slabber, for inspiring me and believing in me. Your guidance throughout these last few years, as my superior and as a friend, is truly appreciated. It is an honour to have been taught and guided by you.

Dr Heidi Rolfes (Chemical Engineering Department, UP):

I would like to thank Dr Rolfes for going out of her way to assist me in particle size measurements made in my thesis.

Dr Linda Prinsloo (Physics Department, UP):

I would like to thank Dr Prinsloo for going out of her way to assist me in the spectroscopic measurements made in this thesis.

Mrs Wiebke Grote (Geology Department, UP):

I would like to express a great deal of thanks to Mrs Grote, who dedicated a great deal of time to X-ray diffraction measurements made in this thesis. Without her dedication (and reluctance to say no to my many demands), none of this would have been possible.

Mr Andrew Pienaar (NECSA):

I would like to thank Mr Pienaar for dedicating so much of his time to performing a great deal of calorimetric work for us and for keeping an open mind!

Dr J Pretorius (Computational Chemistry, UP)

I would like to express the upmost gratitude towards my supervisor, Dr Pretorius, who refused to give up and always believed in the significance of the work that was done. His dedication to this thesis is unparalleled. You have imparted onto me a wealth of knowledge, but most importantly, have taught me to question even the most absolute theories of science. I have the upmost respect for you, not only as my mentor, but also as my friend. May you continue to do great things! May you one day get the recognition that you truly deserve!

ABSTRACT

Multiple papers have been published which attempt to predict the thermal conductivity or thermal diffusivity of graphite “nanofluids”¹⁻⁶. In each of the papers empirical methods (with no consideration of quantum mechanical principles or a structural reference) are employed in an attempt to understand and predict the heat transfer characteristics of a nanofluid. However, the results of each of these papers vary considerably. The primary reason for this may relate to the inability to construct a representative material model (based on the chemical structure), that can accurately predict the thermal enhancement properties based on the intercalated adsorption of a fluid with a noticeable heat capacity³.

This project has strived to simulate the interaction of (nano-scale) graphite particles “dispersed” in water (at the structural level of effective surface “wetting”). The ultimate purpose is to enhance the heat conduction capacity. The strategy was to initially focus on the structural properties of the graphite powder, followed by incremental exposure to water molecules to achieve a representative model. The procedure followed includes these experimental steps:

- a) Molecular resolution porosimetry (i.e. BET) experiments, to determine the graphene “platelet” surface area to correlate with the minimum crystallite size (where a single graphite crystal is made up of multiple unit cells) of the graphite powder samples.
- b) Powder X-ray diffraction (PXRD) analyses of the graphite powder samples each supplied by different manufacturers in order to determine their respective crystallographic structures.
- c) Infrared (IR) and Raman vibrational spectra characterisation of all of the graphite powder samples for further structure confirmation.
- d) Thermo-gravimetric analysis (TGA) of graphite powder and water mixture samples, to try and determine the point at which the bulk water has separated and evaporated away from the graphite powder/water mixture, resulting in a minimum layer of water adsorbed on the graphite surface and inter-/intra-particle graphite spaces.
- e) Differential scanning calorimetry (DSC) of the “dry” and “surface-wetted” graphite samples to determine their specific heat capacities.
- f) Laser flash analysis (LFA) of the “dry” and “surface-wetted” graphite samples to determine their thermal diffusivity and thermal conductivity.
- g) The computer simulated analysis of the graphite powder exposed to water by means of computational modelling, to elucidate the various conformational approaches of water onto the graphite surface and the associated thermodynamic behaviour of water molecules ad/absorbed at the graphite surface.

Data from the TGA measurements allowed for the determination of the appropriate amount of water required in order to not only experimentally prepare graphite “surface-wetted” samples, but also to determine the effective amount of absorbed water to be considered in the computational models. For experimental verification, both dry and wet graphite samples should then be used in a laser flash analysis (LFA), in order to elucidate the effect the interfacial layer of water has on the thermal properties of graphite.

A computerised model of a single graphite crystal exposed to water was created using the MedeA (v. 2.14) modelling software. The conformational behaviour and energy states of a cluster of water molecules on the graphite surface were then analysed by using the VASP 5.3 software (based on a periodic solid-state model approach with boundary conditions), to determine the energetics, atomic structure and graphite surface “wetting” characteristics, at the atomistic level. The results of the computerised model were correlated to the physical experiments and to previously published figures.

Only once a clear understanding of the way in which water molecules interact with the graphite surfaces has been obtained, can further investigation follow to resolve the effect that exposure of larger graphite surfaces to polar solvents (such as water and lubricants) will have on the heat conductance of such ensembles. This scope of further work will constitute a PhD study.

Chair:

Signature_____

MSENG Programme: Mechanical Engineering

Date_____

Preface

Solvent adsorption on material surfaces forms a crucial component of catalysis studies, lubrication analysis (in the natural sciences and engineering) and prediction of adhesion properties (glues) and requires extended model simulations to predict grander scale material properties normally employing finite element, thermo-flow or discrete element analyses (in the engineering fields).

It is the objective of this study to demonstrate the underlying scientific components that represent the building blocks of atomic moieties, structural restrictions, group symmetry conditioning and thermodynamic conditions involved in the solvent adsorption on graphite surfaces as an initial approach, to eventually move into a macro-scale of heat conductance derivation. The aim is to utilise existing advanced scientific computational software systems to study the underlying conditions and material structural extents, to achieve representative models in direct correlation with experimental observations (then already at the macro-scale level).

The results achieved in this study could well become the ground rules for moving into more flexible graphene type nano-surfaces exposed to a variety of solvent molecules, which could lead to effective mechanisms to “feed” engineering simulations and offer a unique suite of model conditions to derive material properties of this nature.

CONTENTS

List of figures.....	9
List of tables.....	10
Abbreviations.....	12
1. Motivation for research.....	13
2. Introduction.....	14
3. Literature review.....	15
3.1 Graphite.....	15
3.1.1 Crystallographic structure.....	15
3.1.2 Computational modelling of the graphite structure.....	17
3.2 Fabrication of graphite.....	18
3.3 Nano-structured surfaces.....	19
3.3.1 Adsorption.....	19
3.3.2 Structure and size determination.....	21
3.3.3 Material properties.....	26
3.3.4 Modelling of material surface interactions.....	27
3.3.5 Modelling of interfacial thermal behaviour.....	30
3.3.6 Physical measurement of thermal properties.....	32
3.3.7 Surface wettability.....	32
3.4 References.....	35
4. Experimental methods.....	48
4.1. Molecular resolution porosimetry analysis.....	49
4.2. Powder X-ray diffraction (XRD) analysis.....	49
4.3. Fourier transform infrared (FTIR) and Raman vibrational spectra characterization.....	49
4.4 Thermo-gravimetric analysis (TGA).....	50
4.5 Differential scanning calorimetry (DSC).....	50
4.6 Laser flash analysis (LFA).....	51
5. Experimental results and discussion.....	52
5.1. Molecular resolution porosimetry analysis.....	52
5.2. Powder X-ray diffraction (XRD) analysis.....	52
5.3. Fourier transform infrared (FTIR) and Raman vibrational spectra characterisation.....	66
5.4. Thermo-gravimetric analysis (TGA).....	68
5.5. Differential scanning calorimetry (DSC).....	71
6. Computational modelling.....	77
6.1 Graphite crystal surface.....	80

6.1.1	Structure selection	80
6.1.2	Model size	81
6.1.3	Partial charges.....	83
6.2	Bulk water	87
6.3	“Wetted” graphite model	88
6.4	Thermo-physical analysis	89
6.5	Computational results and interpretation.....	91
6.6	Sources of discrepancy.....	96
7.	Conclusion.....	97
8.	Recommendations	98
9.	References	99
	Annexure.....	102
	Part A – calculated thermal conductivities	102
	Part B – differential thermo-gravimetric analysis (DTGA) data plots	104
	Part C – laser flash apparatus laboratory parameters	107
	Part D – brief outline of the EMD approach	115

LIST OF FIGURES

Figure 3-1: Comparison between the simple hexagonal (a), hexagonal/bernal (b), rhombohedral (c) graphitic structures and the face-centred cubic diamond structure ¹³ (d). The interlayer distance is c and the distance between nearest-neighbours is a ^{5,6} (see Figure 3-1 a)	16
Figure 3-2: An SEM micrograph of foliated graphite ²⁰	17
Figure 3-3: An illustration of the construction of a single graphite nanoparticle	17
Figure 3-4: The graphitic crystallite assembly model ⁵¹	20
Figure 3-5: Infra-red spectra of natural graphite after grinding for 96 hours. The top curve is scale-expanded ⁵⁸	22
Figure 3-6: (a) Comparison of Raman spectra at 514 nm for bulk (AB stacked) graphite and graphene. They are scaled to have similar height of the 2D peak at approximately 2700cm^{-1} . (b) Evolution of the spectra at 514nm excitation with the number of layers ⁶¹	22
Figure 3-7: XRD patterns of different graphite powders. (a) As-received; (b) Ball-milled for 20 h; (c) Ball-milled for 20 h and then annealed at $1700\text{ }^\circ\text{C}$ for 9 h ²¹	24
Figure 3-8: Experimental and simulated XRD patterns of a sonicated sample of graphite ¹⁰	24
Figure 3-9: Neutron diffraction patterns for diamond and graphite powder.	25
Figure 3-10: Typical density of states of graphite ¹⁹	27
Figure 3-11: Definition of contact angle, Θ , used to define the wettability of solid surfaces.	33
Figure 3-12: TGA curves of synthesised hydrozincite intermediate and the corresponding first-order differential (DTG) of the TGA curve ¹⁷⁰	34
Figure 5-1: XRD Analysis of all graphite powder samples (top), followed by the calculated diffraction pattern (bottom) produced using PowderCell	52
Figure 5-2: $\text{Cu-K}\alpha$ XRD powder pattern calculated using PowderCell, for both unrefined space groups.	56
Figure 5-3: Basal plane of hexagonal unit cell	61
Figure 5-4: Assumed shape of graphite crystallite	62
Figure 5-5: Two hexagonal unit cells, stacked vertically on top of one another	63
Figure 5-6: FTIR patterns of the four graphite powders supplied by (i)US Research Nanomaterials Inc. (ii)mkNANO Inc. (iii)Nanostructured & Amorphous Materials Inc. and (iv)PBMR SA	66
Figure 5-7: Raman patterns of the four graphite powders supplied by the PBMR SA, US Research Nanomaterials Inc., mK NANO and Nanostructured and Amorphous Materials Inc	67
Figure 5-8: Results of TGA analysis for samples 1 through to 6. NGG concentrations are also indicated (by weight percentage). T^* and W^* indicates the final point of release of bulk water.	69
Figure 5-9: Results of TGA analysis of samples 7 through to 12. NGG concentrations are also indicated (by weight percentage). T^* and W^* indicates the final point of release of bulk water.	69
Figure 5-10: Graph indicating the relationship between the fraction of graphite present within the graphite-water mixture and the point at which the expulsion of water (indicated by W^* in Figure 5-9) from the mixture is delayed	70
Figure 5-11: Relationship between ζ (mass ratio) and T^*	71
Figure 5-12: Calculated heat capacitance values of sapphire from DSC analysis, with referenced heat capacitance values indicated (red)	73
Figure 5-13: Calculated heat capacitance values for clean and wet NGG samples of various specific wetting values (ζ)	74
Figure 5-14: Heat capacitance values measured/calculated for dry and wet samples of NGG	75
Figure 6-1: Methodology followed in the modelling process	79
Figure 6-2: The majority of voids within the crystal are shown to pass through the centre of the planes defined when considering a $2\times 2\times 1$ supercell built using the hexagonal unit cell	81
Figure 6-3: One of two final (orthorhombic shaped) graphite surface models, built using the hexagonal unit cell, extended to a super cell within MedeA	83

Figure 6-4: (MOPAC) Flow chart used to produce partial atomic charges.	84
Figure 6-5: Average partial charges calculated for oxygen and hydrogen contained in a bulk water model, using MOPAC	87
Figure 6-6: Hexagonal-based, “wetted” graphite surface models	89
Figure 6-7: Flow chart used to determine the thermal conductivity of each “wetted” graphite surface	90
Figure 6-8: Thermal conductivity results obtained for the dry and wet, hexagonal (i.e. 194), graphite model with lattice vectors $a[5,0,0]$, $b[3,6,0]$ and $c[0,0,4]$. Only the direct integral values for intra-planar thermal conductivities along the “X-axis” are shown for the wet graphite models.	91
Figure 6-9: Thermal conductivity results obtained for the dry and wet, hexagonal (i.e. 194), graphite model with lattice vectors $a[5,0,0]$, $b[3,6,0]$ and $c[0,0,4]$. Only the direct integral values for intra-planar thermal conductivities along the “Y-axis” are shown for the wet graphite models.	91
Figure 6-10: Thermal conductivity results obtained for the dry and wet, hexagonal (i.e. 194), graphite model with lattice vectors $a[5,0,0]$, $b[3,6,0]$ and $c[0,0,4]$. Only the direct integral values for inter-planar thermal conductivities along the “Z-axis” are shown for the wet graphite models.	92
Figure 6-11: Thermal conductivity results obtained for the dry and wet, rhombohedral (i.e. 166), graphite model with lattice vectors $a[5,0,0]$, $b[3,6,0]$ and $c[0,0,3]$. Only the direct integral values for intra-planar thermal conductivities along the “X-axis” are shown for the wet graphite models.	92
Figure 6-12: Thermal conductivity results obtained for the dry and wet, rhombohedral (i.e. 166), graphite model with lattice vectors $a[5,0,0]$, $b[3,6,0]$ and $c[0,0,3]$. Only the direct integral values for intra-planar thermal conductivities along the “Y-axis” are shown for the wet graphite models.	93
Figure 6-13: Thermal conductivity results obtained for the dry and wet, rhombohedral (i.e. 166), graphite model with lattice vectors $a[5,0,0]$, $b[3,6,0]$ and $c[0,0,3]$. Only the direct integral values for inter-planar thermal conductivities along the “Z-axis” are shown for the wet graphite models.	93
Figure C-1: Samples prepared for LFA measurement	113
Figure C-2: Low viscosity liquid sample holder utilised in LFA measurements	114
Figure D-1: Flowchart outlining the computational and mathematical approach to calculating the thermal conductivity of crystal structures, using Equilibrium Molecular Dynamics	115

LIST OF TABLES

Table 4-1: Details of graphite nanopowder samples purchased	48
Table 5-1: Experimentally determined surface area of graphite nanopowder samples	52
Table 5-2: Experimentally observed diffraction indices for all four graphite samples applying Cu $K_{\alpha 1}$ -radiation at $\lambda=1.5406 \text{ \AA}$. Reflections with a relative intensity >0.4 are listed	53
Table 5-3: Phase compositions of four graphite samples, derived from Rietveld analysis (2H refers to hexagonal phase, 3R refers to rhombohedral phase)	54
Table 5-4: Two-Theta (2θ) X-ray diffraction peak positions for the hexagonal and rhombohedral graphite phases from Cu $K_{\alpha 1}$ -radiation at $\lambda=1.5406 \text{ \AA}$, calculated using the PowderCell software. Only symmetry unique reflections with a relative intensity >0.2 are listed	57
Table-5-5: Calculated (mean) crystallite size and inter-layer distance of each graphite powder sample using XRD	59
Table-5-6: Calculated X-ray lattice parameters of each graphite powder sample using XRD (Rietveld refinement)	59
Table-5-7: Percentage errors between experimentally determined and published lattice parameters	60
Table-5-8: Data used in the calculation of the crystallite surface area	61
Table 5-9: Calculated crystallite surface areas for the four graphite powder samples	64
Table 5-10: Raman frequency lists for each of the graphite powder samples	67
Table 5-11: Sample compositions and instrumental parameters used in the TGA analysis	68

<i>Table 5-12: Processed data indicating how much demineralised water, per milligram of NGG, is required in order to prepare samples of only "surface wetted" graphite and its dependence on temperature.</i>	70
<i>Table 5-13: Prepared sample compositions (containing de-ionised water and nuclear grade graphite) and instrumental parameters used in DSC. It must be noted that only a fraction of each of the (wet) samples listed below was used</i>	72
<i>Table 5-14: Calculated specific (isobaric) heat capacities for "wetted" graphite samples, containing various concentrations of de-ionised water (with an average heat capacitance of approximately 4.18 J/g.K)</i>	74
<i>Table 6-1: Unit cells selected from the crystallographic databases provided by the MedeA software suite</i>	80
<i>Table 6-2: Result of structure optimisation simulation</i>	80
<i>Table 6-3: Graphite model sizes utilised for computational modelling</i>	82
<i>Table 6-4: (MOPAC) Calculated partial charges of carbon atoms comprising a single hexagonal unit cell within the orthorhombic - shaped supercell graphite surface (figures presented to four decimal places)</i>	85
<i>Table 6-5: (MOPAC) Calculated partial charges of carbon atoms comprising a single rhombohedral unit cell within the orthorhombic - shaped supercell graphite surface (figures presented to four decimal places)</i>	86
<i>Table 6-6: Calculated size (using TGA data) of bulk water super cells required to represent graphite "wetted" surfaces</i>	87
<i>Table 6-7: Average partial charges calculated for oxygen and hydrogen contained in a bulk water model, using MOPAC</i>	88
<i>Table 6-8: Predicted thermal conductivities, for all dry hexagonal and rhombohedral models. The values reported below are the average values, calculated over the entire temperature range (refer to Annexure A for detail)</i>	94
<i>Table 6-9: Correlation of calculated (dry graphite) thermal conductivities (averaged over both space groups) to published figures also produced using computational modelling techniques</i>	95
<i>Table 6-10: Correlation of calculated (dry graphite) thermal conductivities (averaged over both space groups) to published figures, produced using experimental techniques</i>	95
<i>Table C-1: Sample compositions (containing de-ionised water and nuclear grade graphite) and measurement temperatures used in thermal conductivity measurement</i>	109

ABBREVIATIONS

BET	Brunauer–Emmett–Teller analysis provides precise specific <i>surface area</i> and <i>pore size</i> distribution evaluation of materials by nitrogen multilayer adsorption measured as a function of relative pressure using a fully automated analyser
BFDH	Bravais, Friedel, Donnay and Harker-Crystal morphologies
IR	Infrared spectroscopic analysis
LAMMPS	Large-scale A tomic/ M olecular M assively P arallel S imulator --- <i>software</i>
LEED	Low energy electron diffraction
MedeA	A computational modelling software suite embedding a collative set of material-based and solid-state scientific functional packages used in this study – developed and distributed by: <i>Materials Design Inc.</i> Paris, France
MOPAC	M olecular O rbital P ACKage
Nano-material	– Particles with a size between 1 and 100 nm (> 1 nm)
NECSA	Nuclear Energy Corporation South Africa, Pelindaba
NGG	Nuclear grade graphite “natural graphite” (of very high purity) intended for use in nuclear applications
PBEsol	Perdew-Burke-Ernzerhof functional (PEB), adapted for solids (PEB sol), employed in the MedeA software suite, used to study all models in this project, applying the VASP software
PXRD	Powder X-ray diffraction
Raman	Raman spectroscopy provides characteristic fundamental vibrations that are employed to reveal the molecular structure of a sample
SAXS	Small Angle X-ray scattering, X-ray diffraction in the small angle region ($2\theta < 5^\circ$)
SEM/TEM	Scanning/transmission electron microscopy
TGA	Thermo-gravimetric Analysis
DSC	Digital scanning calorimetry
VASP	Vienna <i>Ab Initio</i> simulation package (density functional based software)
vdW	van Der Waal’s forces, the weak electric forces that attract neutral molecules to one another

1. MOTIVATION FOR RESEARCH

The objective of this research will be to correlate experimental findings with solid-state modelling (entailing computational structure and vibrational analyses) and refine a practical model to be employed in future applications, involving larger nano-material/solvent moieties, to predict thermal properties of higher orders. Natural graphite has been selected as *adsorbent* material with water as *adsorbate*.

The following practical considerations are but a few crucial steps to contemplate in this MEng study:

- a) Derive the appropriate surface size of the nano-material (graphite) to be applied in the modelling step, which is essentially a scaling consideration.
- b) Define (through a semi-empirical approach) adsorption criteria and the intermittent chemical state of the water species adsorbed on the graphene (extended graphite) surface, required to accurately predict the thermal interfacial chemical association between the aqueous medium and the graphite particle surface.
- c) Highlight the useful relation between experiment and theoretical concepts.

These principles will form the basis for a wider scope (larger nanomaterial surfaces exposed to larger organic species) as an extension into a PhD project.

The results of this research have direct relevance to the feasibility of graphite nanofluids being applied in commercialised thermal power systems.

2. INTRODUCTION

This project has strived to simulate the interaction of graphite powder particles “dispersed” in semi-electrolytic fluids to predict (but also enhance) the heat conduction capacity. The strategy was to initially focus on the structural properties of the graphitic powder by performing supportive physical experiments such as Infrared (IR) and Raman spectroscopic analyses, molecular resolution porosimetry and X-ray powder diffraction.

These were followed by thermo-gravimetric analysis (TGA) measurements, in order to determine the appropriate amount of water necessary to prepare graphite “surface-wetted” samples. Finally, both dry and wet graphite samples were analysed using differential scanning calorimetry (DSC), to study the relationship between specific heat capacitance and the intercalated (inter-planar) adsorption of water. The same samples should then be used in a laser flash analysis (LFA) to determine thermal conductivity enhancement as a result of the intercalated adsorption of water molecules.

Once the structural properties of the graphite powder were obtained, modelling of the graphite surface in an aqueous medium was attempted. The modelling was carried out using the VASP 5.3 (density functional) and LAMMPS (semi-empirical) software. This software (which utilises periodic electronic computational methods to determine the energetics of molecular structures) and associated modules were then used to analyse the thermodynamic properties of the computer-generated graphite-water interface, the results of which were compared to those produced by physical experimentation.

3. LITERATURE REVIEW

A literature review on work already undertaken, exposing graphite particles to fluids was performed. The review commences with a brief on graphite structures and concludes with known computational models, used for the simulation and calculation of the intercalated graphite-water properties.

3.1 GRAPHITE

3.1.1 CRYSTALLOGRAPHIC STRUCTURE

Graphite is an allotrope of carbon that exhibits multiple properties that are appealing to the engineering industry such as a high thermal conductivity, excellent lubrication properties¹⁻³, a resistance to oxidation and allowing the formation of intercalation compounds. Graphite exists in many different forms, such as flake, vein, amorphous and synthetic graphite. Each of these forms exhibit different properties³.

Different shapes of crystals, such as rhombohedral, trapezoidal and hexagonal etc., arise from the close packing together of spheres and their underlying space symmetry relations. These spheres represent the effective space occupied by a single atom within the solid. The term “unit cell” refers to the fewest number of atoms (in crystallographic notation) closely packed at the highest space group, and smallest volume, which demonstrates the essential structure and group symmetry of the crystal lattice⁴.

In the case of natural graphite, two crystal structures are present. These are classified as the bernal (or hexagonal) and the rhombohedral structures^{5,6}. Purely hexagonal graphite crystals, also referred to as highly-orientated pyrolytic graphite (HOPG), can be produced by means of heat treatment processes utilising temperatures greater than 2000°C and is referred to as synthetic graphite⁷. A third possibility is that of simple hexagonal graphite, which can be found within graphite intercalation compounds^{5,12}. Mechanical milling of natural graphites has been said to increase the rhombohedral content within the graphite structure^{3,5,8-11}.

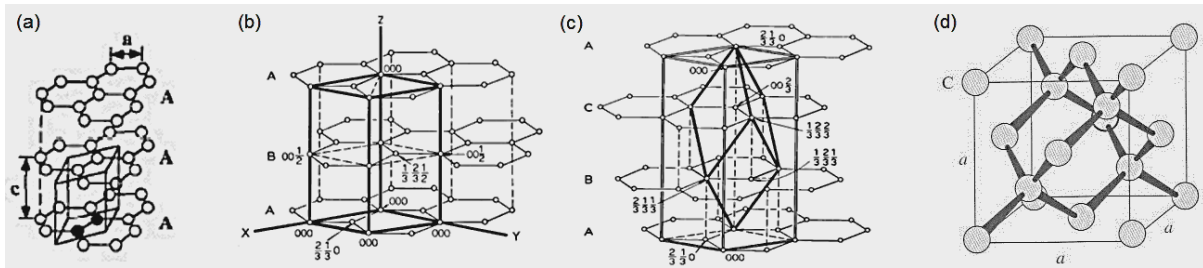


Figure 3-1: Comparison between the simple hexagonal (a), hexagonal/bernal (b), rhombohedral (c) graphitic structures and the face-centred cubic diamond structure ¹³(d). The interlayer distance is c and the distance between nearest-neighbours is a ^{5,6} (see Figure 3-1 a)

The two-dimensional sheets of carbon atoms are known as graphene. In this two-dimensional structure, each carbon atom can donate an electron through a p_z -orbital (which lies perpendicular to the graphene surface and is defined along the Z-axis), forming π -bond interactions above and below the hexagonal ring with an interlayer distance of 3.33 to 3.35Å ^{14,17,68}. This three-dimensional structure is what is known as graphite. These sheets align in such a way that their two-dimensional hexagonal lattices are staggered, either (in the case of natural graphite) as an ABAB pattern or an ABCABC crystal stacking order pattern ^{4,5,7,15,16}. The ABAB pattern is the most common form of natural graphite ^{3-5,17,18}. Rhombohedral graphite is present in small amounts in highly crystalline natural graphite or after extensive grinding of natural graphite in ball mills ³.

A single graphite nanoparticle (ranging in 0.001 to 0.1 microns in size ¹⁹) will consist of multiple graphitic crystallites (or graphite nano-platelets, the size of which is measured in either microns or nanometres), each of which lies at random orientations in space dependent on the manufacturing process used to create the particle. The contact surface between these crystallites is referred to as a grain boundary. A single crystallite is in turn comprised of multiple unit cells (the dimensions of which are measured in Angströms), all of which are arranged (via special group symmetry rules) such that they (in theory) result in a periodic crystal structure (where perfectly flat-planar-shaped sheets of graphene are arranged parallel to each other).

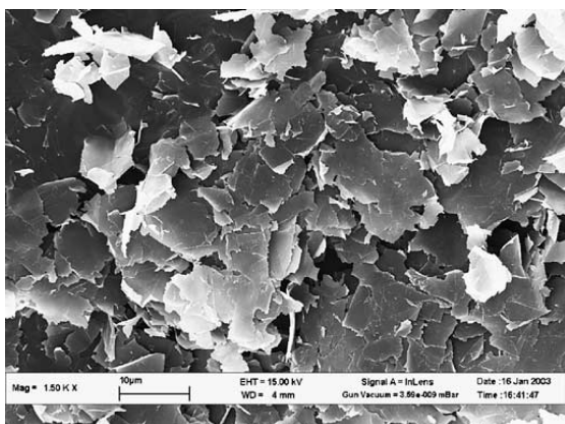


Figure 3-2: An SEM micrograph of foliated graphite ²⁰

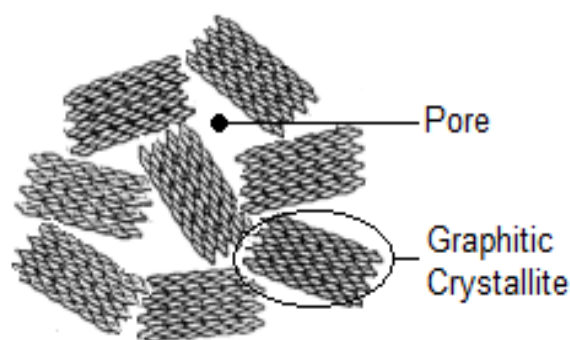


Figure 3-3: An illustration of the construction of a single graphite nanoparticle

This model has become the standard model when used in the computational analysis of graphite ²¹⁻²³. It neglects the fact that, in reality, the nanoparticle may contain distorted microstructures, disordered stacking of graphene layers, increased interlayer spacing at the edges of flakes, curved graphene layers and other structural defects ²¹. Also, the peripheries of the graphene sheets contained in the nanoparticle form dangling σ -bonds to which foreign chemical species may react ²². When considering a collection of nanoparticles, the degree of crystallinity of each individual particle (even if from the same sample) has been known to vary substantially ²⁴. However, recent publications suggest that nanoparticles may at least exhibit a local graphitic arrangement of adjacent layers which includes preserving the ...ABAB... stacking and spacing order ¹⁶.

3.1.2 COMPUTATIONAL MODELLING OF THE GRAPHITE STRUCTURE

As computer modelling of a very large plane of C-atoms is too computationally intensive, as is the case with graphite or graphene, compromises in the modelling of structures such as these would need to be made. A further detraction from the real world scenario would be the neglect of certain features within the crystal lattice, such as various point defects. However, attempts must be made to emulate these deviations from a perfect structure, as accurately as possible.

Hence, in most simulations (from literature references) involving graphene or graphite, where the energetics of the graphene plane or graphite crystal, relative to their atomic structures are not of primary concern, a model consisting of periodic, flat, and defect-free sheets of graphene with no variation in C-C bond length (referred to as ideal graphene or graphite for the purposes of this text) is used ^{23,25-34}.

The most recent and extensive *ab initio* (MP2, Moller Plesset perturbation approach) study of the interaction of water with a graphite surface was based upon the extrapolation of the

interaction energies of water complexes with benzene, coronene (C₂₄H₁₂), circumcoronene (C₅₄H₁₈), and dicircumcoronene (C₉₆H₂₄), from which it was concluded that the water-graphene energy was too large in view of experimental results³⁵. However, there has been an extensive use of molecules such as benzene and coronene in order to represent the (ideal) surfaces of graphene and graphite^{14,27,35-37}.

A study performed by Lamari and Levesque (2011)³⁸ focused on the adsorption of hydrogen on the basal planes of graphite by means of molecular modelling and the utilisation of two different graphene structures. The first structure utilised was that of ideal graphene, while the second structure was that of non-ideal graphene, with the C-atoms of the graphene sheet arranged in a chair conformation and the C-C bond length being chosen as 1.516 Angstrom.

Hasegawa and Nishidate (2004)³⁹ have also studied the inter-layer binding energy of (ideal) graphite by utilising a semi-empirical method in which *ab initio* calculations (based on DFT) were used in conjunction with an empirical van der Waals interaction.

3.2 Fabrication of graphite

Natural graphite particles are normally too large to be mixed directly with a base fluid without any prior treatment, as the particles will settle out rapidly, hence the reason for investigating the use of nano-scopic particles within base fluids to increase the thermal conductivity of the nano-fluid. Treatment methods of natural graphite particles include chemical intercalation and microwave expansion which allow for the production of exfoliated graphite flakes which have an average diameter of several microns and a thickness of a few to several tens of nanometres⁴⁰. More recently, an approach to produce graphite nanoplatelets has been developed that exfoliates natural graphite flakes in formic acid using ultrasonification^{41,42}.

Ball milling of natural graphite particles has also been used to produce nanocrystalline graphite with an average grain (i.e. crystallite) size of 2 nm to 10nm, which is formed during the initial stages of ball milling. Further ball milling results in the formation of turbostratic carbon (in which the graphene sheets may randomly orientate with respect to each other and rotate about the axis normal to the graphene layers). If milling is continued, amorphous carbon will be obtained²¹.

Graphite, if not obtained directly from nature, is commonly produced using a two-step process (resulting in artificial, also referred to as isotropic, graphite). Carbon black (which is pure

elemental carbon in the form of colloidal particles) is produced using liquid or gaseous hydrocarbons which are decomposed at an elevated temperature and under a reduced presence of oxygen^{43,44}. The structure of carbon black represents an intermediary stage between that of graphite and a truly amorphous material²⁴. Currently, the most important carbon black is “furnace black”⁴⁴, derived from hydrocarbons which are partially combusted and immediately quenched with water, resulting in the formation of a primary particle consisting of multiple graphene-like layers³. The graphene layers of furnace black are organised into a graphitic structure in a secondary continuous graphitisation process that takes place in a fluidised bed³.

Another technique used in the production of sub-microscopic graphite particles (crystallite size 4-6 nm) involves the heat treatment of diamond nanoparticles (above $\pm 1000^{\circ}\text{C}$) in an inert Argon atmosphere, converting the diamond nanoparticles into graphite nanoparticles that each form a hollow polyhedron comprising faces of graphene multilayers with an inter-sheet distance of 0.353 nm (which is considerably larger than the inter-sheet distance for bulk graphite, 0.3354 nm)²².

Gui-lei et al. (2007)⁴⁵ have also developed a detonation technique for the production of micrometre-sized expandable graphite powder, with particle sizes ranging from 1 to 10 micrometres whose crystal parameters are close to that of ideal graphite.

3.3 NANO-STRUCTURED SURFACES

3.3.1 ADSORPTION

Elucidation of porous structures is necessary in order to understand the physical and chemical properties of a material. The International Union of Pure and Applied Chemistry (IUPAC) recommends the simple classification of pores.

Zeolites (which have a composition of Al, Si and O) for instance contain intrinsic intraparticle pores as the tetrahedral units (formed by the Al-O and Si-O bonds) cannot occupy the space perfectly, due to geometry constraints, and thus produce cavities. All crystalline solids have more or less intrinsic pores and, unlike zeolites, these pores are not as available for adsorption or diffusion, as a result of their isolated state and small size. Modification of intrinsic structures (by say specific evolution, leaching or other reaction procedures) can also create pores in solid materials^{46,47}.

A single layer of (ideal) graphite is predicted as having a maximum specific surface area in the range of 2600 to 2700 m^2g^{-1} ^{20,48-50}. However this is true when only a single side of the graphitic

crystallite sheet is considered. A study performed by Kaneko et al. (1992)^{51,52} attempted to develop a geometrically-derived relationship between the microcrystalline graphitic structures and specific surface area on the basis of structural data. The graphitic crystallite assembly model utilised in their study consists of pore walls formed by the (002) planes and a cube with n graphitic crystallites.

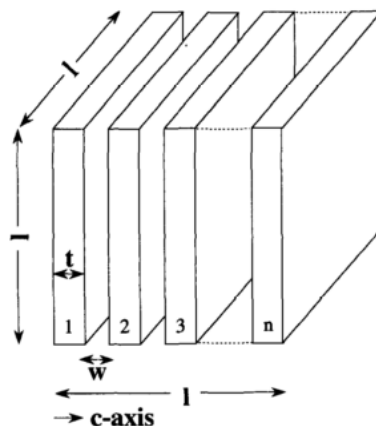


Figure 3-4: The graphitic crystallite assembly model⁵¹

A slight variation of the above model will be utilised as a basis for the size determination of the periodic structure of a graphite crystallite.

It has been shown that the overall pore surface area is inversely proportional to the particle size^{24,53}. Furthermore, Spalaris (1958)⁵³ showed that the surface area of all artificial graphites used in his study (which were of high purity and Acheson type) was found to increase with an increase in outgassing temperature, specifically in the range of 25°C to 500°C. The artificial graphite used was also shown to have an intrinsic microporous structure, with pore radii in the range of 20 to 35 Angstroms, present due to the binding of crystallites with the various binding materials used in the manufacture of graphite. Oxidation of the graphite samples also lead to the enlargement of existing pores (with pore radii in the range of 110 to 170 Angstroms)^{53,54}.

Nitrogen adsorption isotherm characteristics of nuclear graphites have been investigated and have been used to study the average pore size of graphites prior to and after oxidation⁵⁵. A study performed by Pierce (1959)⁵⁶ showed that interparticle (capillary) condensation usually occurs in powder samples, the extent of which is decided by the size, shape and spacing of the particles. If for instance the particle size is greater than 500 nm, interparticle condensation may not be detected.

Powder X-ray diffraction (PXRD) in the small angle region ($2\theta < 5^\circ$) results in two different types of phenomena being observed:

- (i) Sharp maxima due to long-range periodicity in solids,
- (ii) A decrease in intensity with increasing angle.

It has been proposed that this second phenomenon is due to electron density heterogeneities (i.e. pores, the size of which are in the range of 0.5 to 1000 nm) of the material. This X-ray scattering is referred to as small angle X-ray scattering (SAXS). The SAXS method supposedly provides information on open and closed pores, with sizes ranging towards that of micro and mesopores ⁴⁶. However, Nishikawa et al. (1991) ⁵⁷ showed that micrographites can also cause the small-angle scattering in the SAXS study of activated carbon fibres.

3.3.2 STRUCTURE AND SIZE DETERMINATION

Infrared (IR) and Raman spectroscopy

Infrared (IR) and Raman spectroscopy provide characteristic fundamental vibrations that are employed to reveal the molecular structure of a sample. Both mid-IR and Raman spectroscopy are necessary in order to completely measure the vibrational modes of the molecule. Raman spectroscopy is most suitable for symmetric vibrations of non-polar groups. The opposite is true for IR spectroscopy. Due to the vibrational modes being unique to each molecule, the IR and Raman spectrum provide a “fingerprint” of a molecular entity.

IR spectroscopy measures transitions between molecular vibrational energy levels which are a result of the absorption of infrared radiation. This is essentially a resonance condition that involves the electric dipole-mediated transition between vibrational energy levels. An IR analysis of a graphite sample is capable of indicating whether or not the sample is of pure graphite. If for instance the graphite sample has been oxidised (as a result of the manufacturing process) ²⁰, bands due to the presence of carboxyl functional groups at approximately 1650 cm⁻¹ will be observed. In the past multiple attempts were made to obtain the IR spectrum of graphite. Most of these attempts were unsuccessful as absorption was essentially constant throughout the entire IR wavelength range⁵⁸. Work done by Friedel and Carlson (1972) ⁵⁸ attempted to measure the IR spectra of ball milled natural graphite (non-crystalline) using the transmission infra-red method. The study produced good IR spectra, shown in the figure below.

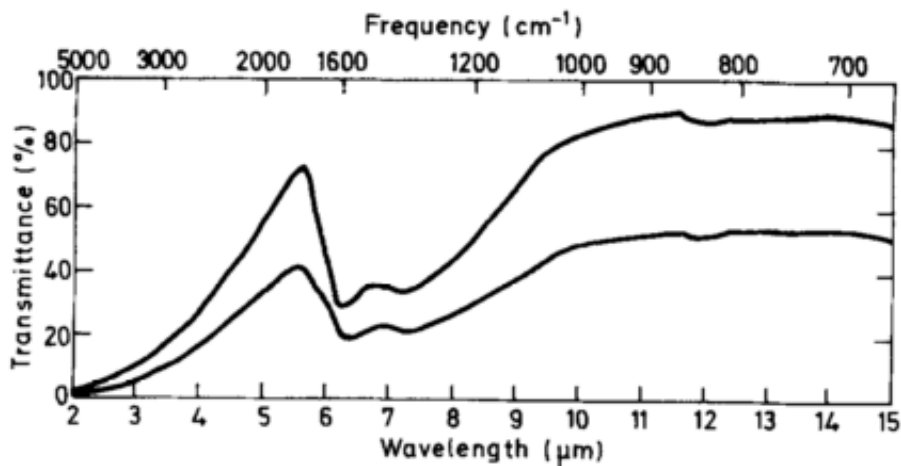


Figure 3-5: Infra-red spectra of natural graphite after grinding for 96 hours. The top curve is scale-expanded⁵⁸

A recent study has shown that infrared extinction properties of columnar nano-graphite particles are related to the shape and size of particles and wavelength⁵⁹.

Raman spectroscopy is a two-photon inelastic light scattering event in which the incident photon is of a much greater energy than the vibrational quantum energy. Radiation is then produced by the molecule, by induced oscillating dipoles brought about in the molecule by the electromagnetic fields of the incident radiation⁶⁰. The Raman spectrum for graphene and bulk graphite is shown in the figure below.

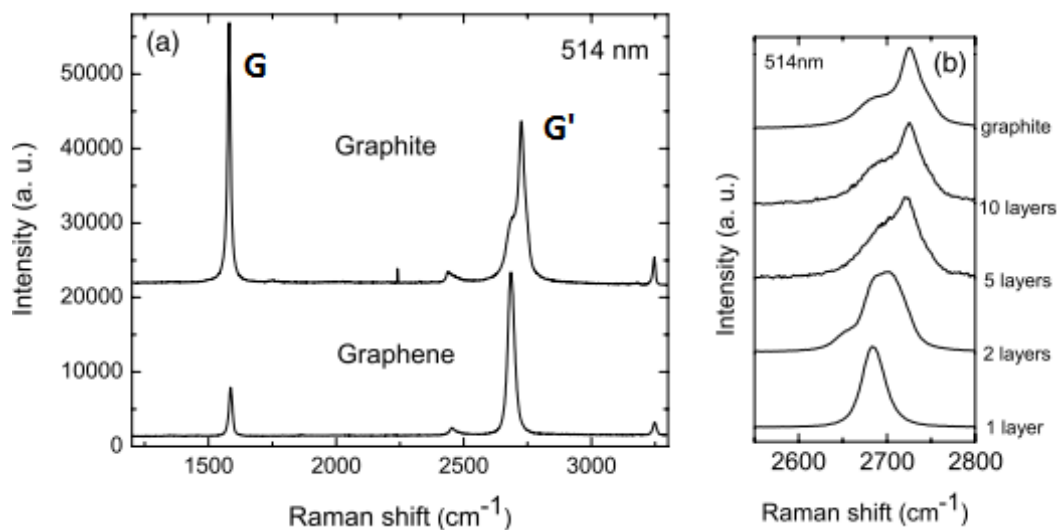


Figure 3-6: (a) Comparison of Raman spectra at 514 nm for bulk (AB stacked) graphite and graphene. They are scaled to have similar height of the 2D peak at approximately 2700cm^{-1} . (b) Evolution of the spectra at 514nm excitation with the number of layers⁶¹

The two most prominent features are the G and G' bands at approximately 1580 cm⁻¹ and 2700 cm⁻¹ respectively and are always observed in graphite samples⁶². Defects within the graphite structure (such as finite particle size effects or lattice distortion, resulting in disorder-induced Raman modes) are thought to give rise to a peak at ±1350 cm⁻¹, known as the D-band^{12,63-67}.

Due to an increased interest in graphite in recent years the IR and Raman finger-print spectrum of unorientated and highly-orientated graphite has been fully characterised^{12,58,61,62,66-78}. The disorder in a graphite sample results in multiple Raman peaks with strange properties⁷⁹. For instance, the disorder-induced Raman modes of graphite (such as the D-band) have been found to depend on the energy of the incident laser beam^{62,69,74,75,77}. Wang et al. (1990)⁷⁷ observed the D-band laser wave-length dependence and suggested that it was a result of scattering from different populations of phonons (which are quantised energy states of collective vibrational modes), possibly through some form of resonance enhancement mechanism. Thomsen and Reich (2000)⁷⁵ were able to show that the energy dependence of the graphite D-mode is in fact due to a double resonance Raman process. Other authors have also attributed the existence of the D-band to a “breathing” vibrational mode^{73,80}. However, the theory of double resonance proposed by Thomsen and Reich (2000) has been used far more extensively and has been applied successfully in a number of papers^{12,61,67,71}.

X-ray diffraction

Powder X-ray diffraction patterns, like the Infrared and Raman spectra, provide a “finger-print” pattern of the sample being analysed, with the positions and intensities of the peaks dependant on the unit cell size and atomic positions within the unit cell, respectively. The widths in combination with the positions of the peaks produced by the pattern are attributed to the crystallite size. If different compound or material phases are present, the resultant plot is created by a super-positioning of the individual patterns. X-ray diffraction allows one (using either Braggs' Law or the Scherrer equation, which is sufficient for small grains in the absence of significant lattice micro-strain¹⁹, along with the Rietveld refinement method), to obtain a great deal of information with regards to the structural, physical and chemical make-up of the material being investigated^{4,81,82}.

It is known that small crystallites (usually smaller than approximately 1 micron) and/or the presence of lattice strain may result in a substantial broadening of the peaks^{19,82-85}. Also, peaks resulting from smaller particles are observed at marginally higher diffraction angles, indicating lattice contraction¹⁹. Both strain and size effects are considered in the two approaches, each specified by Williamson and Hall (1953)⁸⁶.

Li et al. (2007) ²¹ published X-ray diffraction patterns of graphitic and turbostratic carbon. In this paper an attempt was made to study the effects of the microstructure on the X-ray diffraction patterns by incorporating distortion factors into the general Debye equation used to calculate the diffraction pattern. These distortion factors were created to account for the rotation, translation and curvature of the graphene layers in turbostratic carbon. This study also showed that the diffraction peak's full width at half maximums (FWHMs) increases while the diffraction angles decrease with decreasing crystallite size ^{21,87}. The diffraction pattern of graphite powder (with an average particle size of 5µm) before and after it underwent ball milling is shown in Figure 3-7 and Figure 3-8.

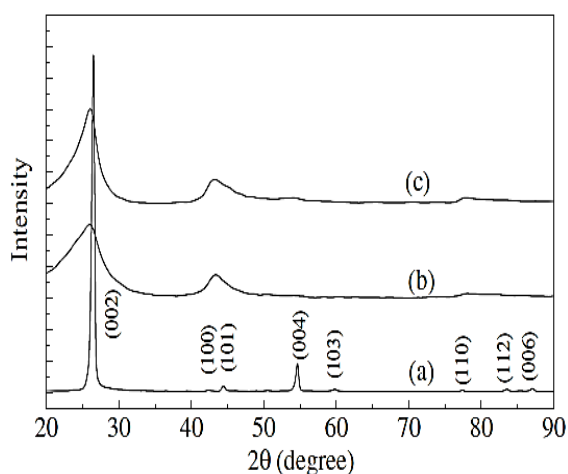


Figure 3-7: XRD patterns of different graphite powders. (a) As-received; (b) Ball-milled for 20 h; (c) Ball-milled for 20 h and then annealed at 1700 °C for 9 h ²¹

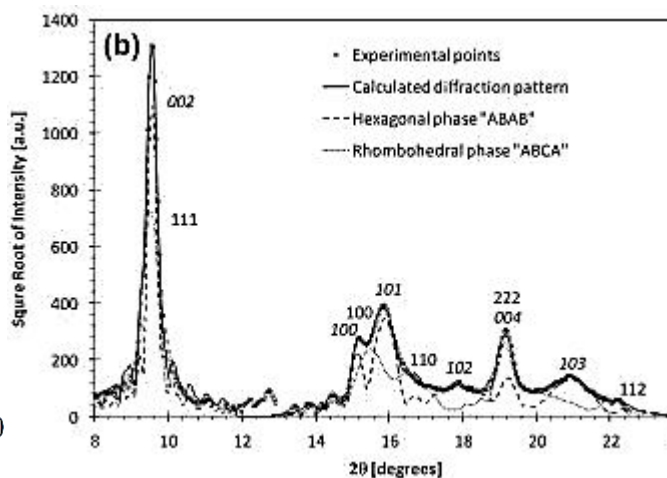


Figure 3-8: Experimental and simulated XRD patterns of a sonicated sample of graphite ¹⁰

All Cu-K_α (incident radiation) X-ray diffraction patterns obtained for graphite produce a high intensity peak at a Bragg angle (2θ) of approximately 27 degrees ^{9,10,17,21,22,83,84,87-109}.

Neutron diffraction

Neutron diffraction involves the elastic atomic scattering of neutrons in the material, while X-ray diffraction involves the atomic scattering of electrons. Like X-ray diffraction, the sample is placed in a beam of (either thermal or cold) neutrons and the intensity pattern around the sample gives information about its structure. If different material phases are present, the resultant plot is created by a super-positioning of the individual patterns ^{90,110,111}.

The neutron diffraction pattern produced by graphite is shown in the image below. All neutron diffraction analyses of graphite produce a high intensity (002) peak at an angle of approximately 18 degrees (2θ) ^{90,110,112}. This peak (and others) have been known to shift when

the graphite sample is irradiated by neutrons (such as in a nuclear reactor environment) for extended periods of time ⁸⁵. The major part of diffuse scattering in these patterns arises from multiple scattering in the sample ¹¹². It was also postulated that, both the bending and randomising of the basal planes orientation are the origin for the large volume expansion of irradiated graphite. Furthermore, it was found that graphite easily loses its lattice ordering in the basal planes, while managing to retain its layered structure (i.e. the (002) peaks are not destroyed) ⁸⁹.

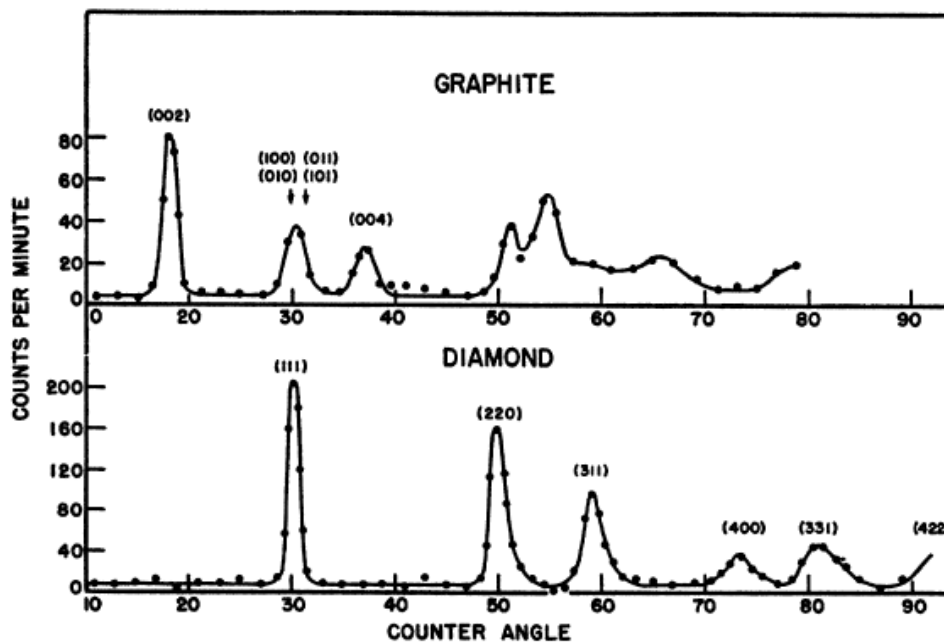


Figure 3-9: Neutron diffraction patterns for diamond and graphite powder.

In a study done by Burian et al. (1999) ¹¹³, wide-angle neutron scattering was used to study multiwall carbon nanotubes. It was found that the (002) and (004) peaks of the nanotubes appear at smaller angles than graphite and that, at small-scale lengths, the nanotube structure resembles that of graphite.

More recently a study was performed that examined the behaviour of reactor-grade graphite under operating conditions using neutron powder diffraction. From the collected diffraction patterns an intense broadening of several of the reflections was observed, attributed to the presence of turbostratic carbon. A Rietveld-refinement approach was then applied in an attempt to quantify this disorder structurally ⁸⁵.

Attempts have also been made to utilise Brunauer–Emmett–Teller (BET) measurements together with other optical characterisation techniques (such as SEM, TEM and laser counting) to develop a relationship between the microcrystalline graphitic structures and specific surface

area ^{20,49}. By comparing the specific surface area of a hypothetical graphitic crystallite (2600 to 2700 m²g⁻¹) to that of a foliated graphite particle, the average thickness of the particle can be determined and correlated to results obtained by electron microscopy (EM) observations ²⁰.

Low energy electron diffraction (LEED) has been used in the study of surface reconstruction of silicon. The surface was found to lower its energy through structure reconstruction, by saturating the dangling bonds which result from the missing nearest neighbours. The surface relaxation effects were found to extend three to four atomic layers into the bulk. A phenomenon - known as surface segregation, in which atoms or molecules which lower the surface free energy accumulate at the surface - is also observed during the energy reduction process of clean high energy surfaces. This phenomenon may also lead to adsorbate-induced restructuring ¹⁹.

3.3.3 MATERIAL PROPERTIES

An important consideration with regards to nano-scopic particles is the change of bulk parameters and loss of perfect periodicity near the surface. When the size of a cluster of atoms falls below a dimension of 100nm (or more specifically for the case of semi-conductors, becomes comparable to the electron's de Broglie wavelength), quantisation effects occur and properties such as melting point, hardness and conductivity etc. are no longer constant and depend strongly on the size and packing structure ^{19,114}. An unperturbed periodicity is necessary for the presence of a delocalised state which in turn results in efficient quantum mechanical transport (i.e. superconductivity, magnetism etc.).

Two types of variations as a function of size include scalable effects (such as the surface to volume ratio) and quantum effects (such as molecular cluster energy levels) ¹⁹.

Due to the resultant anisotropic bonding between the graphene sheets of graphite a weak electron and phonon dispersion along the Z-axis of the graphite structure exists, which gives rise to the semi-metallic behaviour of three dimensional graphite ^{5,67}. Charlier et al. (1994) ⁵ concluded in their study of the stacking effect on the electronic properties of graphite that the bonding between graphene sheets is not uniquely dominated by van der Waals interactions (which are weak electric forces that attract neutral molecules to one another and reduces proportionally to r^{-6} , where r is the interatomic distance).

Sir Neville Mott theorised that a material may exhibit metallic, semi-metallic or insulator properties, depending on the temperature of that material. This is due to the variability of the Kubo gap (δ) that lies within the density of states (DOS) ¹⁹. The DOS in the region of the Fermi level (i.e. the energy level of the highest occupied state at 0°K), determines the electronic nature

of a structure. It essentially provides the total concentration of available (quantised) energy states that electrons may occupy within a specific energy range. Also, the contribution of the electrons to the specific heat of the material is proportional to the DOS at the Fermi energy ^{19,115}.

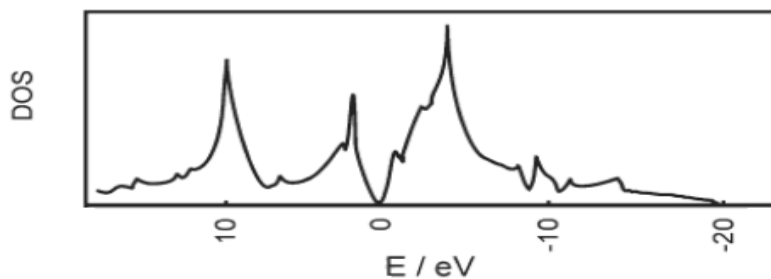


Figure 3-10: Typical density of states of graphite ¹⁹

3.3.4 MODELLING OF MATERIAL SURFACE INTERACTIONS

Multiple approaches to the computational modelling of (periodic) atomic structures and their interactions with foreign chemical species exist. The theories/models necessary for the purpose of this thesis includes thermodynamic models, continuum mean field models, molecular dynamics and electronic structure theory (which include density functional theory, the Hartree-Fock approach and Monte Carlo application). Each of these theories (and modifications thereof) has been used repeatedly in an attempt to understand the interaction of foreign molecules with graphite surfaces.

Dolejs and Manning (2010) ¹¹⁶ proposed a thermodynamic model for mineral dissolution in aqueous fluids, such as H₂O, at elevated temperatures and pressures. This model was shown to describe the energetics of solvation more accurately than does the Born electrostatic theory. In recent years the underlying structure of water (i.e. hydrogen bonding) and other hydrogen-bonded species has also been investigated ^{117,118}.

Continuum mean-field models (which utilise statistical mechanics to reduce a N-body problem to a 1-body problem by approximating the effect of all other entities on any single entity by a single averaged effect), one of the most recent being the SM8 model, attempt to mimic the multiple electrostatic and non-electrostatic interactions that arise between a molecule and a surrounding medium. The SM8 model may be combined with density functional theory (DFT) or Hartree-Fock theory to describe the electronic structure of the solute and its associated self-consistent field polarisation by the solvent. This model, which is considered to be a universal solvation model, is capable of calculating solvation free energies and other thermodynamic properties in solution ¹¹⁹.

Applying molecular dynamics in the analysis of the energies of atomic structures and molecules is one approach of modelling the interaction of molecules with graphite surfaces ^{34,37,38,120}.

Camellone and Marx (2013) ¹²¹ performed large-scale *ab initio* molecular dynamics (AIMD) simulations, aimed at the investigation of solvation effects at gold nano-clusters (used as nano-catalysts) pinned onto TiO₂ in contact with water. It was found that the aqueous solution induced a pronounced charge transfer and localisation at the nano-catalyst-liquid interface. The same authors also performed PBE+U AIMD simulations to reveal the solvent-induced structure-specific charge rearrangement at the metal-liquid interface. Adisa et al. (2011) ²⁶ also used molecular dynamics to successfully model the adsorption of methane (CH₄) on a graphite surface. Their results were shown to be in good agreement with experiments and also indicated that the adsorption of CH₄ on the graphite surface is more favourable at lower temperatures and higher pressures.

Another study performed by Tran-Duc et al. (2010) ³⁷ investigated the mechanism of adsorption of polycyclic aromatic hydrocarbons on a graphite surface by the application of the continuous atomistic approximation in combination with the Lennard-Jones potential. The graphite surface was modelled using coronene (C₂₄H₁₂). In a more recent study, molecular modelling was utilised to investigate the adsorption of nitrogen on a graphite surface over a range of temperatures below the boiling point ²⁹. The mechanisms of the interfacial layer formation at the neutral graphite monolayer (i.e. graphene)-ionic liquid (1,3-dimethylimidazolium chloride) interface have also been investigated by means of fully atomistic molecular dynamics simulations, suggesting that a significant enrichment of ionic liquid cations at the graphite surface takes place ³⁰.

In recent years multiple papers focusing on the electronic structure of molecules and crystals have been published in an attempt to describe the structure and energetics of graphitic nanomaterials ^{5,39,122-129}, all of which are either based on one of the two following fundamental theories: density functional theory (DFT) and the Hartree-Fock approach. From past work performed on graphite and graphene it has become clear that a conventional DFT approach becomes inadequate if a clear understanding of the adsorption process of gases or polar molecules (such as water) on graphene or graphite surfaces is required. The reason is that DFT fails to describe weak intermolecular interactions (i.e. van der Waals forces) and charge polarisation effects including the long-range dispersion energy between molecules ^{23,25,27,35,37,39,122,123,126,128,130-132}. Hence, multiple extensions of these two fundamental theories have been proposed.

These include computational models such as ^{14,23,25,35,39,122,123,126,128,131-133}

- (i) DFT-CC (density-functional theory/coupled cluster method)
- (ii) DFT-CCSD(T) (density-functional theory/coupled cluster method utilising single and double bonds)
- (iii) DFT-D (semi-empirical addition of dispersive forces to conventional density functionals)
- (iv) DFTB-D (density-functional tight-binding method augmented with an empirical van der Waals correction)
- (v) DFT-SAPT (density-functional theory symmetry-adapted perturbation theory)
- (vi) DFT/vdW-WF (density-functional theory with the inclusion of the van der Waals interactions, based on the use of the maximally localised Wannier functions)

Collignon et al. (2005) ²⁷ performed an *ab initio* study of the adsorption of water on the hydroxylated graphite surfaces, based on a combined semi-empirical and DFT approach. The graphite surface was modelled by fusing 30 benzene rings together (forming a C₈₀H₂₂ cluster). This surface was optimised with the semi-empirical MNDO method, after which the ONIOM method (which utilises DFT) was implemented to place an OH group on either the edge or surface of the graphite cluster and perform geometry optimisations and energy calculations. The structure was also optimised for the case of five water molecules interacting with the OH site. It was shown that these OH groups can act as nucleation centres for small water aggregates. The adsorption of hydrogen and extended hydrogen dimer (amalgamation of two hydrogen atoms) configurations on top of a (0001) graphite surface has also been investigated by means of electronic structure calculations ^{32,36}, indicating substantial surface reconstruction due to the re-hybridisation of the carbon atoms valence orbitals ³² and decreased barriers to the sticking of the second H-atom ³⁶. In the study performed by Slijivancanin et al. (2009) ³⁶ the graphite surface was modelled by periodically repeated rhombohedral supercells containing one graphite sheet, separated by a 15 Angstrom vacuum.

Monte Carlo simulations (and variations thereof) have also been used extensively in the investigation of adsorption on the graphite surface and in graphite slit-like pores ^{28,29,31,33,134,135}. Nguyen et al. (2008) ³³ have proposed a hybrid reverse Monte Carlo (HRMC) procedure for the atomistic modelling of the microstructure of activated carbons. In this approach the initial atomic configuration is estimated using pore size and pore wall thickness distribution characterisation results.

Although a large number of models have been proposed, the (relative) accuracy of each of these models for the use of the adsorption of polar molecules on the surface of graphite is not yet

clear as the amount of research and physical experimentation performed for such a scenario is limited ^{14,23,25,35,131,133,136}.

3.3.5 MODELLING OF INTERFACIAL THERMAL BEHAVIOUR

The thermal behaviour of solids is based from the Schrodinger equation which uses a nuclear wave function and Hamiltonian, and is known as the second adiabatic approximation equation. This approximation considers the kinetic energy of nuclei and the effects that are concerned with their atomic dynamics.

$$\hat{H}_n(\mathbf{R})X_{\xi K}(\mathbf{R}) \equiv [\hat{T}_n(\mathbf{R}) + U_\xi(\mathbf{R}) + \Lambda_{\xi\xi}(\mathbf{R})]X_{\xi K}(\mathbf{R}) = EX_{\xi K}(\mathbf{R}) \quad (1)$$

(From “*Quantum Theory of the Solid State*”, by L. Kantorovich, 2004 ¹³⁷)

\mathbf{R} = Universal coordinate system

$X_{\xi K}$ = Nuclear wave function

\check{T}_n = Kinetic energy contribution

U_ξ = Potential energy contribution

$\Lambda_{\xi\xi}$ = Entropy contribution

By assuming that atoms simply oscillate around their (equilibrium) lattice positions, one is able to obtain a very good approximation of the equilibrium properties of the crystal structure at low temperatures. It is these (quantised) vibrations, i.e. phonons, in crystals which play a crucial role in nearly all their properties, including their transport properties such as thermal conductivity ¹³⁷.

The Debye model was created to estimate the contribution of these phonons towards the transport properties of the crystal. It estimates that the contribution to the heat capacity, at low temperature, is directly proportional to the (temperature)³ of the crystal. Mathematical approaches such as this are used to build (solid-state) computational modelling packages, such as the “large-scale atomic/molecular massively parallel simulator” (LAMMPS). Molecular dynamics (MD) simulations are often used to predict thermal properties of nano-sized crystals, and have been used extensively in the thermal characterisation (with regards to thermo-physical properties and thermal stability) of graphite ¹³⁸⁻¹⁴¹. In general, MD simulations predict the intra-layer/in-plane thermal conductivity of natural graphite to lie in the range of 450 to 5800 W/m.K, while inter-plane thermal conductivities are predicted to be orders of magnitude lower ¹⁴¹⁻¹⁴⁴.

Khadem and Wemhoff (2013) ¹³⁸ applied equilibrium molecular dynamics (EMD) to various graphite structures (ABA,ABC and AAA) of a size no larger than 5 nm x 5 nm. The Green-Kubo (GK) relation was also used in conjunction with EMD to predict the thermal conductivity of each of the graphite structures. The authors noted that size effects on the thermal conductivities calculated with these simulations were inevitable, due to the long phonon mean-free paths within graphite. This study, along with many others, concluded that the interlayer thermal conductivity values were significantly lower than the intralayer values, due to the weak phonon dispersion along the Z-axis ¹⁴⁵⁻¹⁴⁹, with a calculated intra-layer and inter-layer thermal conductivity of 450 to 800 W/m.K and 9 to 55 W/m.K, respectively.

Wei et al. (2010) ¹⁵⁰ also studied the interfacial thermal resistance in multi-layer graphene structures using molecular dynamics, but utilised a non-equilibrium molecular dynamics (NEMD) approach. The study concluded that the interfacial thermal resistance depended heavily on the number of layers present in the structure and decreased with an increasing layer number, tending towards a limiting value. The study (among others) also concluded that the increase in the interfacial thermal resistance with an increase in temperature, above room temperature, was attributed to the increase in phonon scattering and the decrease in phonon wavelength ^{150,151}.

A comparison of the EMD (Green-Kubo) and NEMD simulation methods was performed by Schelling et al. (2002) ¹⁵². It was found that, for the Green-Kubo method, one is always assured of lying in the linear-response regime; however, very slow convergence of the auto-correlation function becomes a significant consideration. Both approaches exhibited finite-size effects, which were far more severe when considering the NEMD approach. Also, both methods could be used to calculate the bulk thermal conductivity of perfect crystalline solids, with the Green-Kubo method being more applicable to perfect crystal systems with very long mean-free (phonon) paths. The authors also believed that the results obtained by the direct integration of the auto-correlation function represented the most reliable way to compute the thermal conductivity when using the Green-Kubo method. When considering inhomogeneous systems, the NEMD method was found to be preferable, as the Green-Kubo approach computes an average thermal conductivity over an entire system, making it unsuitable for the study of interfacial effects/defects.

Two approaches applied frequently to the analysis of phonon contributions across an interface include the acoustic mismatch model (AMM) and the diffuse mismatch model (DMM), both of which indicate a higher interfacial conductance if materials of matching vibrational properties are used ¹⁴⁰. Molecular dynamics has also recently been used by Shenogin et al. (2013) ¹⁴⁰ to

study the thermal boundary resistance at carbon-metal interfaces, utilising a polymer consistent force field (PCFF) and a 6-9 Lennard-Jones (non-bonded) potential. The thermal conductance values obtained from the simulations were found to be lower than the values obtained through physical experimentation, by approximately 20%.

3.3.6 PHYSICAL MEASUREMENT OF THERMAL PROPERTIES

The addition of carbon allotropes, such as graphite and carbon fibres, into various materials utilised in industry (such as cement, oils, polyethylene and coolants) has been investigated by multiple authors in an attempt to improve the thermal properties of the “solvent”. Although various models used to try and predict the thermal behaviour of the composite material formed (using graphite) are not completely capable of producing reliable and consistent results, physical experimentation has shown that an increase in the desirability of various thermal properties, such as heat capacitance and thermal conductivity, can be obtained ^{1,2,40,153-160}. Methods used to experimentally determine the thermos-physical properties of these mixtures include the transient hot wire method ,a laser flash apparatus (LFA) and digital scanning calorimetry (DSC) ^{40,154,161-163}. Shawn et al. (2006) ¹⁶⁴ have also developed an optical beam deflection technique for the thermal diffusivity measurement of nanofluids.

The most commonly used device used in the analysis of a material’s thermos-physical properties is the LFA, as it is capable of handling a wide variety of samples, whether they are in the form of a solid, paste, or viscous liquid ¹⁶⁵. An LFA involves the heating of a sample with a short laser pulse, leading to a change in temperature on the receiving side of the sample.

The rate of change in temperature on the reverse side of the sample is measured using a thermo-couple. The in-plane and out-of-plane thermal conductivity of natural polycrystalline graphite (at room temperature) has been estimated to lie in the range of 100 - 600 W/m.K and 5 to 80 W/m.K, respectively ^{144,147,148,150,166}.

3.3.7 SURFACE WETTABILITY

The term “wettability” is used to describe the inclination of a solid surface (the sorbent) to be in contact with one fluid as opposed to another (the adsorbate) and is primarily estimated by means of determining the contact angle, θ . If the contact angle is less than 90° , the liquid is said to wet the surface (illustrated in Figure 3-11). The wettability of a solid surface is dependent on both the properties of the surface and the fluid ^{167,168}.

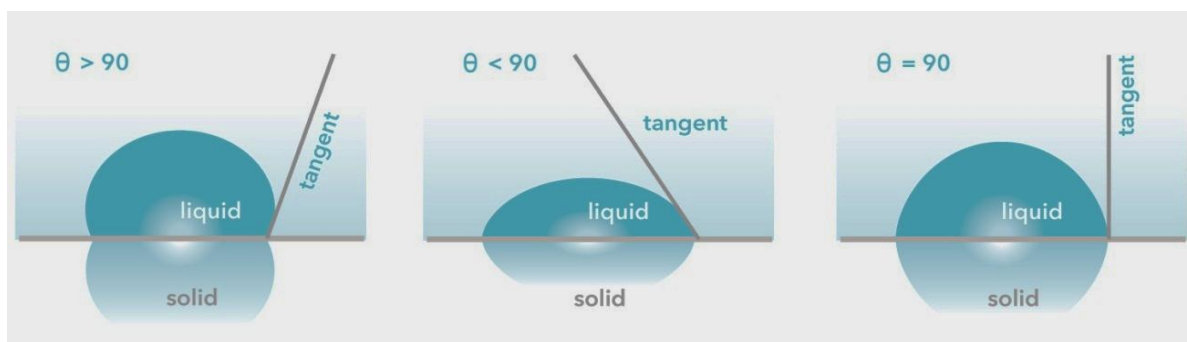


Figure 3-11: Definition of contact angle, θ , used to define the wettability of solid surfaces.

The principle above describes the interaction between a liquid and macro-sized solid surface. For the purposes of this thesis, the term “wettability” is used to describe the affiliation a nano-sized graphite surface has for water molecules very close to the particle surface as opposed to water molecules far away from the particle surface (which constitutes a part of the bulk water surrounding the particle). Also, the term “surface-wetted” is used to refer to graphite particles whose surfaces, inter-/intra-particle and inter-/intra-layer spaces have undergone adsorption of water molecules.

It is possible that a variably different inter-water conformational arrangement exists with the graphite surface than would be observed in bulk water. Hence, the water molecules adsorbed on the surface may require either more or less energy (depending on the nature of their interaction) if they are to be removed from the surface, when compared to the separation of water molecules from a bulk solution. It follows that data produced by an experimental procedure known as a TGA, may provide an indication of the wettability of the graphite surface and may also provide evidence for the presence of “surface wetted” graphite particles.

A TGA is a technique wherein a sample (which could either be a liquid, solid, or combination thereof) is subjected to a computer-controlled (pressure/temperature gradient) program in a controlled atmosphere. The mass of this sample is then continuously monitored as a function of temperature ¹⁶⁹. An example of a typical TGA data plot is given in Figure 3-12, utilising a thermo-gravimetric curve, which simply considers the relationship between mass loss and temperature and utilising a first-order differential thermo-gravimetric curve. This data may then be used to determine the temperature at which significant thermal events take place, indicated by changes in the TG gradient (or peaks in the DTG curves) ¹⁶⁹.

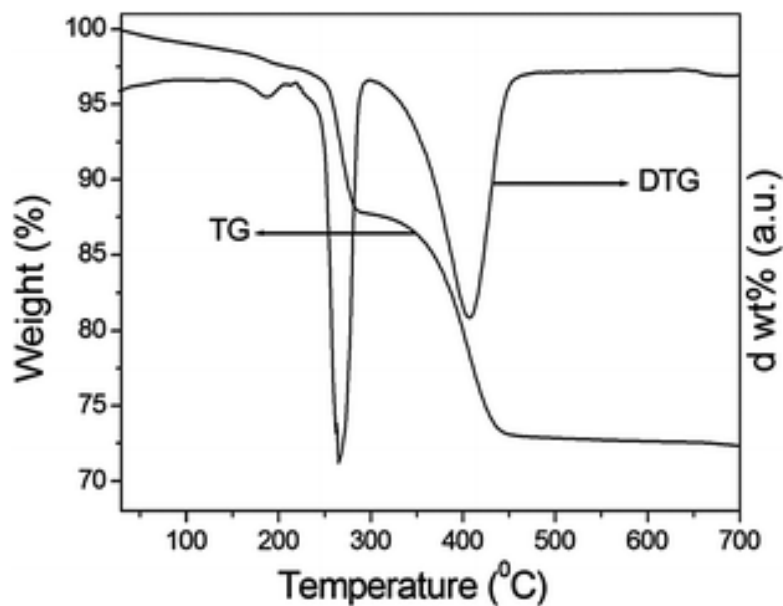


Figure 3-12: TGA curves of synthesised hydrozincite intermediate and the corresponding first-order differential (DTG) of the TGA curve ¹⁷⁰

The investigation into the thermal behaviour of samples containing both (distilled) water and (pure, natural) graphite has not been studied by means of a TGA isothermal desorption cycle. Multiple TGA studies involving combinations of graphite (or graphene), graphite oxide, polyurethane foam, epoxy resins and many other chemical compounds have been performed, all of which utilise a large temperature gradient (with a maximum temperature exceeding 500°C) and high heating rate (with a temperature increase greater than 10°C /min) ^{163,171-177}. Studying the thermal behaviour of water adsorbed on a graphite surface by means of TGA (desorption cycle), requires the use of a small temperature range (almost isothermal time/step intervals) and at a slow heating rate, at constant pressure.

3.4 REFERENCES

1. Choi, C., Jung, M. & Oh, J. Preparation and characterization of lubricating oil-based nanofluids containing carbon nanoparticles. *Korean J. Mater. Res.* **19**, 156–162 (2009).
2. Choi, C., Jung, M., Ahn, K. & Oh, J. Thermal and tribological properties of lubricating oil-based nanofluids. in *Soc. Tribol. Lubr. Eng. - 2008 Annu. Meet. Exhib. Ext. Abstr.* 1 (2008). at <<http://0-www.scopus.com.innopac.up.ac.za/record/display.url?view=basic&eid=2-s2.0-77954894548&origin=resultlist>>
3. Wissler, M. Graphite and carbon powders for electrochemical applications. *J. Power Sources* **156**, 142–150 (2006).
4. Hammond, C. *The Basics of Crystallography and Diffraction*. 331 (Oxford University Press, 2001). at <<http://books.google.com/books?id=NaGLdNHGvPQC&pgis=1>>
5. CHARLIER, J. C., GONZE, X. & MICHENAUD, J. P. FIRST-PRINCIPLES STUDY OF THE STACKING EFFECT ON THE ELECTRONIC PROPERTIES OF GRAPHITE (S). *Carbon N. Y.* **32**, 289–299 (1994).
6. Kwiecińska, B. & Petersen, H. . Graphite, semi-graphite, natural coke, and natural char classification—ICCP system. *Int. J. Coal Geol.* **57**, 99–116 (2004).
7. Chung, D. Review graphite. *J. Mater. Sci.* **7**, 1475–1489 (2002).
8. Wilhelm, H., Croset, B. & Medjahdi, G. Proportion and dispersion of rhombohedral sequences in the hexagonal structure of graphite powders. Supplementary Data. *Carbon N. Y.* **45**, 2356–2364 (2007).
9. Lee, Y. T., Yoon, C. S. & Sun, Y.-K. Improved electrochemical performance of Li-doped natural graphite anode for lithium secondary batteries. *J. Power Sources* **139**, 230–234 (2005).
10. Łoś, S., Duclaux, L., Alvarez, L., Hawełek, Ł., Duber, S., Kempniński, W. Cleavage and size reduction of graphite crystal using ultrasound radiation. *Carbon N. Y.* **55**, 53–61 (2013).
11. Kohs, W., Santner, H. J., Hofer, F., Schrottner, H., Doninger, J., Barsukov, I., Buqa, H., Albering, J. H., Moller, K. C., Besenhard, J. O., Winter, M. A study on electrolyte interactions with graphite anodes exhibiting structures with various amounts of rhombohedral phase. *J. Power Sources* **119-121**, 528–537 (2003).
12. Reich, S. & Thomsen, C. Raman spectroscopy of graphite. *Philos. Trans. R. Soc. Ser. A, Math. Phys. Eng. Sci. R. Soc.* **362**, 2271–88 (2004).
13. (UNSW) University of New South Wales. Functionality from Electronic Materials. at <<http://www.pems.adfa.edu.au/~s9471553/level1/Teaching/ElectronicProperties/Functionality.html>>
14. Sheng, L., Ono, Y. & Taketsugu, T. Ab Initio Study of Xe Adsorption on Graphene. *J. Phys. Chem. C* **114**, 3544–3548 (2010).

15. Gray, D., Mccaughan, A. & Mookerji, B. Crystal Structure of Graphite , Graphene and Silicon. *Phys. Solid State Appl.* **2**, 3–5 (2009).
16. Dimitrakopoulos, G. P., Dravid, V. P., Karakostas, T. & Pond, R. C. The Defect Character of Carbon Nanotubes and Nanoparticles. *Acta Crystallogr. Sect. A Found. Crystallogr.* **53**, 341–351 (1997).
17. Volkova, S., Il'icheva, O. M. & Kuznetsov, O. B. X-ray study of the graphite-bearing rocks from the Pestpaksha ore occurrence and structural features of graphite. *Lithol. Miner. Resour.* **46**, 363–368 (2011).
18. Trucano, P. & Chen, R. Structure of graphite by neutron diffraction. (1975). doi:10.1038/258136a0
19. Roduner, E. *Nanoscopic materials: size-dependent phenomena*. 285 (The Royal Society of Chemistry, 2006).
20. Chen, G., Weng, W., Wu, D., Wu, C., Lu, J., Wang, P., Chen, X. Preparation and characterization of graphite nanosheets from ultrasonic powdering technique. *Carbon N. Y.* **42**, 753–759 (2004).
21. Li, Z. Q., Lu, C. J., Xia, Z. P., Zhou, Y. & Luo, Z. X-ray diffraction patterns of graphite and turbostratic carbon. *Carbon N. Y.* **45**, 1686–1695 (2007).
22. Andersson, O., Prasad, B., Sato, H., Enoki, T., Hishiyama, Y., Kaburagi, Y., Yoshikawa, M., Bandow, S. Structure and electronic properties of graphite nanoparticles. *Phys. Rev. B* **58**, 16387–16395 (1998).
23. Ambrosetti*, A. & Silvestrelli, P. L. Adsorption of Rare-Gas Atoms and Water on Graphite and Graphene by van der Waals-Corrected Density Functional Theory. *J. Phys. Chem. C* 3695–3702 (2011). doi:10.1021/jp110669p
24. Zhu, W., Miser, D. E., Geoffrey Chan, W. & Hajaligol, M. R. HRTEM investigation of some commercially available furnace carbon blacks. *Carbon N. Y.* **42**, 1841–1845 (2004).
25. Silvestrelli, P. L., Benyahia, K., Grubisić, S., Ancilotto, F. & Toigo, F. Van der Waals interactions at surfaces by density functional theory using Wannier functions. *J. Chem. Phys.* **130**, 074702 (2009).
26. Adisa, O. O., Cox, B. J. & Hill, J. M. Modelling the surface adsorption of methane on carbon nanostructures. *Carbon N. Y.* **49**, 3212–3218 (2011).
27. Collignon, B., Hoang, P. N. M., Picaud, S. & Rayez, J. C. Ab initio study of the water adsorption on hydroxylated graphite surfaces. *Chem. Phys. Lett.* **406**, 430–435 (2005).
28. Do, D. D. & Do, H. D. Modeling of adsorption on nongraphitized carbon surface: GCMC simulation studies and comparison with experimental data. *J. Phys. Chem. B* **110**, 17531–8 (2006).

29. Fan, C., Do, D., Nicholson, D., Jagiello, J., Kenvin, J., Puzan, M. Monte Carlo simulation and experimental studies on the low temperature characterization of nitrogen adsorption on graphite. *Carbon N. Y.* **52**, 158–170 (2013).
30. Fedorov, M. V & Lynden-Bell, R. M. Probing the neutral graphene-ionic liquid interface: insights from molecular dynamics simulations. *Phys. Chem. Chem. Phys.* **14**, 2552–6 (2012).
31. Kowalczyk, P., Tanaka, H., Holyst, R., Kaneko, K., Ohmori, T., Miyamoto, J. Storage of hydrogen at 303 K in graphite slitlike pores from grand canonical Monte Carlo simulation. *J. Phys. Chem. B* **109**, 17174–83 (2005).
32. Lanzani, G., Martinazzo, R., Materzanini, G., Pino, I. & Tantardini, G. F. Chemistry at surfaces: from ab initio structures to quantum dynamics. *Theor. Chem. Acc.* **117**, 805–825 (2007).
33. Nguyen, T. X., Cohaut, N., Bae, J.-S. & Bhatia, S. K. New method for atomistic modeling of the microstructure of activated carbons using hybrid reverse Monte Carlo simulation. *Langmuir* **24**, 7912–22 (2008).
34. Riemann, A. & Owens, B. E. Molecular mechanics modeling of the adsorption of methionine on graphite. *Surf. Sci.* **604**, 2084–2090 (2010).
35. Nachtigall, P., Bludsky, O. & Rubes, M. Structure and Stability of the Water-Graphite Complexes. *J. Phys. Chem. C* 8412–8419 (2009). doi:10.1021/jp901410m
36. Slijivancanin, Z., Rauls, E., Hornekaer, L., Xu, W., Besenbacher, F., Hammer, B. Extended atomic hydrogen dimer configurations on the graphite(0001) surface. *J. Chem. Phys.* **131**, 084706 (2009).
37. Tran-Duc, T., Thamwattana, N., Cox, B. J. & Hill, J. M. Adsorption of polycyclic aromatic hydrocarbons on graphite surfaces. *Comput. Mater. Sci.* **49**, S307–S312 (2010).
38. Darkrim Lamari, F. & Levesque, D. Hydrogen adsorption on functionalized graphene. *Carbon N. Y.* **49**, 5196–5200 (2011).
39. Hasegawa, M. & Nishidate, K. Semiempirical approach to the energetics of interlayer binding in graphite. *Phys. Rev. B* **70**, 1–7 (2004).
40. Wang, J. J., Zheng, R. T., Gao, J. W. & Chen, G. Heat conduction mechanisms in nanofluids and suspensions. *Nano Today* **7**, 124–136 (2012).
41. Geng, Y., Wang, S. J. & Kim, J.-K. Preparation of graphite nanoplatelets and graphene sheets. *J. Colloid Interface Sci.* **336**, 592–8 (2009).
42. Cravotto, G. & Cintas, P. Sonication-assisted fabrication and post-synthetic modifications of graphene-like materials. *Chemistry* **16**, 5246–59 (2010).
43. Donnet, J. B., Banasal, R. C. & Wang, M. J. *Carbon Black—Science and Technology*. (Marcel Dekker, 1993).

44. ICBA : What is Carbon Black. at <http://carbon-black.org/what_is.html>
45. Sun, G., Li, X. & Yan, H. Detonation of expandable graphite to make micron-size powder. *New Carbon Mater.* **22**, 242–246 (2007).
46. Kaneko, K. Determination of pore size and pore size distribution 1 . Adsorbents and catalysts. *J. Membr. Sci.* **96**, 59–89 (1994).
47. Maeda, K., Mizukami, F., Watanabe, M., Niwa, S., Toba, M., Shimizu, K. Control with polyethers of pore distribution of alumina by the sol-gel method. *Chem. Ind.* (1989).
48. Rao, C., Subrahmanyam, K., Ramakrishna Matte, H., Abdulhakeem, B., Govindaraj, A., Das, B., Kumar, P., Ghosh, A., Late, D. A study of the synthetic methods and properties of graphenes. *Sci. Technol. Adv. Mater.* **11**, 054502 (2010).
49. KANEKO, K., ISHII, C., RUIKE, M. & KUWABARA, H. ORIGIN OF SUPERHIGH SURFACE AREA AND STRUCTURES OF ACTIVATED CARBONS. *Carbon N. Y.* **30**, 1075–1088 (1992).
50. Li, B. & Zhong, W.-H. Review on polymer/graphite nanoplatelet nanocomposites. *J. Mater. Sci.* **46**, 5595–5614 (2011).
51. Kaneko, K., Ishii, C., Ruike, M. & Kuwabara, H. Origin of superhigh surface area and microcrystalline graphitic structures of activated carbons. *Carbon N. Y.* **30**, 1075 (1992).
52. Kaneko, K. & Ishii, C. Superhigh surface area determination of microporous solids. *Colloid Surfaces* **67**, 203 (1992).
53. Spalaris, C. N. The micropore structure of artificial graphite. **60**, 1480–1483 (1958).
54. Manocha, L. M., Manocha, S., Patel, K. B. & Glogar, P. Oxidation behaviour of Carbon/Carbon Composites impregnated with silica and silicon oxycarbide. *Carbon N. Y.* **38**, 1481–1491 (2000).
55. Choi, W.-K., Kim, B.-J., Kim, E.-S., Chi, S.-H. & Park, S.-J. Oxidation behavior of IG and NBG nuclear graphites. *Nucl. Eng. Des.* **241**, 82–87 (2011).
56. Pierce, C. Effects of Interparticle Condensation on Heats of Adsorption and Isotherm of powdered samples. *J. Phys. Chem.* **63**, 1076–1079 (1959).
57. Fujiwara, Y., Nishikawa, K., Iijima, T. & Kaneko, K. Simulation of small-angle X-ray scattering behavior of activated carbon fibers adsorbing water. *J. Chem. Soc. Faraday Trans.* **87**, 2763 (1991).
58. Friedel, R. A. & Carlson, G. L. Difficult carbonaceous materials and their infra-red and Raman spectra. Reassignments for coal spectra. *Fuel* **51**, 194–198 (1972).
59. Wang, H., Song, Z., Yang, N. & Ma, J. Infrared Extinction Properties of Randomly Oriented Columnar Nano-Graphite Particles. *Adv. Mater. ...* **602-604**, 165–168 (2013).
60. Larkin, P. *Infrared and Raman Spectroscopy; Principles and Spectral Interpretation*. 239 (Elsevier, 2011). at<<http://books.google.com/books?hl=en&lr=&id=KPyV1>>

DRMRbwC&oi=fnd&pg=PP2&dq=INFRARED+AND+RAMAN+SPECTROSCOPY+PRINCIPLES+AND+SPECTRAL+INTERPRETATION&ots=cAaKDX2CM-&sig=BZcvotp_KJ44knp0ETTWvOU97Zg>

61. Ferrari, A., Meyer, J., Scardaci, V., Casiraghi, C., Lazzeri, M., Mauri, F., Piscanec, S., Jiang, D., Novoselov, K., Roth, S., Geim, A. Raman Spectrum of Graphene and Graphene Layers. *Phys. Rev. Lett.* **97**, 1–4 (2006).
62. Vidano*, R. P., Fischbach, O. B., Willis, L. J. & Loehr, T. M. OBSERVATION OF RAMAN BAND SHIFTING WITH EXCITATION WAVELENGTH FOR CARBONS AND GRAPHITES. *Solid State Commun.* **39**, 1–4 (1981).
63. Lue, J. T. in *Encycl. Nanosci. Nanotechnol.* (Nalwa, H. S.) 1–46 (American Scientific Publishers, 2007).
64. Dean, K., von Allmen, P. & Chalamala, B. R. Three behavioral states observed in field emission from single-walled carbon nanotubes. *J. Vac. Sci. Technol. B Microelectron. Nanom. Struct.* **17**, 1959 (1999).
65. Vitali, G., Rossi, M., Terranova, M. & Sessa, V. Laser-induced structural modifications of glassy carbon surfaces. *J. Appl. Phys.* **77**, 4307–4311 (1995).
66. Perraki, M., Proyer, A., Mposkos, E., Kaindl, R. & Hoinkes, G. Raman micro-spectroscopy on diamond, graphite and other carbon polymorphs from the ultrahigh-pressure metamorphic Kimi Complex of the Rhodope Metamorphic Province, NE Greece. *Earth Planet. Sci. Lett.* **241**, 672–685 (2006).
67. Kostic, R., Miric, M., Radic, T., Radovic, M., Gajic, R., Popovic, Z. V. Optical Characterization of Graphene and Highly Oriented Pyrolytic Graphite. *ACTA Phys. Pol. A* **116**, 718–721 (2009).
68. RRUFF. Graphite R050503 - RRUFF Database: Raman, X-ray, Infrared, and Chemistry. at <<http://rruff.info/Graphite/R050503>>
69. Kawashima, Y. & Katagiri, G. Fundamentals, overtones, and combinations in the Raman spectrum of graphite. *Phys. Rev. B* **52**, (1995).
70. Rangappa, D., Jang, J. & Honma, I. Supercritical Fluid Processing of Graphene and Graphene Oxide. *Graphene: Properties, Synthesis and Applications* (2011)
71. Ferrari, A. & Robertson, J. Resonant Raman spectroscopy of disordered, amorphous, and diamondlike carbon. *Phys. Rev. B* **64**, 075414 (2001).
72. Lee, J., Lee, I.-H. & Lee, J. Unbiased Global Optimization of Lennard-Jones Clusters for $N \leq 201$ Using the Conformational Space Annealing Method. *Phys. Rev. Lett.* **91**, 080201 (2003).
73. Mapelli, C., Castiglioni, C., Zerbi, G. & Müllen, K. Common force field for graphite and polycyclic aromatic hydrocarbons. *Phys. Rev. B* **12710** (1999). at <http://prb.aps.org/abstract/PRB/v60/i18/p12710_1>

74. Tan, P., Hu, C., Dong, J., Shen, W. & Zhang, B. Polarization properties, high-order Raman spectra, and frequency asymmetry between Stokes and anti-Stokes scattering of Raman modes in a graphite whisker. *Phys. Rev. B* **64**, 214301 (2001).
75. Thomsen, C. & Reich, S. Double resonant raman scattering in graphite. *Phys. Rev. Lett.* **85**, 5214–7 (2000).
76. Vives, E. & Planes, A. Is Tsallis Thermodynamics Nonextensive? *Phys. Rev. Lett.* **88**, 020601 (2001).
77. Wang, Y., Alsmeyer, D. C. & McCreery, R. L. Raman Spectroscopy of Carbon Materials: Structural Basis of Observed Spectra. *Chem. Masters* 557–563 (1990).
78. Zhou, S. Y., Gweon, G.-H. & Lanzara, a. Low energy excitations in graphite: The role of dimensionality and lattice defects. *Ann. Phys. (N. Y.)*. **321**, 1730–1746 (2006).
79. Tuinstra, F. Raman Spectrum of Graphite. *J. Chem. Phys.* **53**, 1126 (1970).
80. Castiglioni, C., Negri, F., Rigolio, M. & Zerbi, G. Raman activation in disordered graphites of the A1 symmetry forbidden k not equal to 0 phonon: the origin of the D line. *J. Chem. Phys.* 3769 (2001).
81. Introduction to X-ray Diffraction (XRD) | PANalytical. at <<http://www.panalytical.com/index.cfm?pid=135>>
82. Pecharsky, V. & Zavalij, P. *Fundamentals of powder diffraction and structural characterization of materials*. 751 (Springer Science and Business Media, 2008). doi:10.1007/978-0-387-09579-0
83. Petersen, T., Yarovsky, I., Snook, I., McCulloch, D. G. & Opletal, G. Microstructure of an industrial char by diffraction techniques and Reverse Monte Carlo modelling. *Carbon N. Y.* **42**, 2457–2469 (2004).
84. Teplykh, A. E., Bogdanov, S. G., Dorofeev, Yu. A., Pirogov, A. N., Skryabin, Y. N., Makotchenko, V. G., Nazarov, A. S., Fedorov, V. E. Structural state of expanded graphite prepared from intercalation compounds. *Crystallogr. Reports* **51**, S62–S66 (2006).
85. DiJulio, D. D. & Hawari, a. I. Examination of reactor grade graphite using neutron powder diffraction. *J. Nucl. Mater.* **392**, 225–229 (2009).
86. G. K. Williamson, W. H. H. XRAY Line Broadening form Filed Aluminium and Wolfram. 22–31 (1953). at <[http://lib.semi.ac.cn:8080/tsh/dzzy/wsqq/selected_papers/Acta Metallurgica/1-22.pdf](http://lib.semi.ac.cn:8080/tsh/dzzy/wsqq/selected_papers/Acta_Metallurgica/1-22.pdf)>
87. Nagano, K., Wakayama, H., Fukushima, Y., Fukunaga, T. & Mizutani, U. Structural Change of Graphite by Mechanical Milling. *ç²%õõã½“ãŁŠã,ãŁ³ç²%õõææ« ...* (1996). at <<http://scholar.google.com/scholar?hl=en&btnG=Search&q=intitle:Structural+Change+of+Graphite+by+Mechanical+Milling#1>>

88. Kim, D., Hwang, Y., Cheong, S. I., Lee, J.K., Hong, D., Moon, S., Lee, J. E., Kim, H.S. Production and characterization of carbon nano colloid via one-step electrochemical method. *J. Nanoparticle Res.* **10**, 1121–1128 (2008).
89. Tanabe, T., Muto, S. & Niwase, K. On the mechanism of dimensional change of neutron irradiated graphite. *Appl. Phys. Lett.* **61**, 1638–1640 (1992).
90. Wang, S., Newton, J., Wang, R. & Taub, H. Multilayer structure of nitrogen adsorbed on graphite. *Phys. Rev. B* **39**, 331–341 (1989).
91. Sun, G., Li, X., Qu, Y., Wang, X., Yan, H., Zhang, Y. Preparation and characterization of graphite nanosheets from detonation technique. *Mater. Lett.* **62**, 703–706 (2008).
92. Asthana, A., Matsui, Y., Yasuda, M., Kimoto, K., Iwata, T., Ohshima, K. Investigations on the structural disordering of neutron-irradiated highly oriented pyrolytic graphite by X-ray diffraction and electron microscopy. *J. Appl. Crystallogr.* **38**, 361–367 (2005).
93. Aurbach, D., Markovsky, B., Weissman, I., Levi, E. & Ein-Eli, Y. On the correlation between surface chemistry and performance of graphite negative electrodes for Li ion batteries. *Electrochim. Acta* **45**, 67–86 (1999).
94. Fukunaga, T., Nagano, K., Mizutani, U., Wakayama, H. & Fukushima, Y. Structural change of graphite subjected to mechanical milling. *J. Non. Cryst. Solids* **232-234**, 416–420 (1998).
95. Han, J., Cho, K., Lee, K. & Kim, H. Porous graphite matrix for chemical heat pumps. *Carbon N. Y.* **36**, 1801–1810 (1998).
96. Henderson, M. J. & White, J. W. An X-ray Diffraction and Small Angle X-ray Scattering Study of Solvated Li-Graphite Intercalation Compounds. *Int. J. Energy Eng.* **1**, 19–26 (2011).
97. Jang, J., Oh, J. H. & Stucky, G. D. Fabrication of ultrafine conducting polymer and graphite nanoparticles. *Angew. Chemie Int. Ed.* **41**, 4016–4019 (2002).
98. Lee, Y.-T., Yoon, C. S., Prakash, J. & Sun, Y.-K. Effect of Li-Doping on Electrochemical Performance of Natural Graphite Anode for Lithium Secondary Batteries. *J. Electrochem. Soc.* **151**, A1728 (2004).
99. Lexa, D. & Dauke, M. Thermal and structural properties of low-fluence irradiated graphite. *J. Nucl. Mater.* **384**, 236–244 (2009).
100. Li, X., Qiu, X., Yuan, H., Chen, L. & Zhu, W. Size-effect on the activity of anodic catalysts in alcohol and CO electrooxidation. *J. Power Sources* **184**, 353–360 (2008).
101. Inc., C. Graphite Powders - GX Series - Carbonix Inc . Graphite Powders - GX Series Graphite Powders - GX Series - Carbonix Inc . 4–6 (2013). at <http://carbonix.en.ec21.com/Graphite_Powders_GX_Series>
102. Shi, H. Coke vs. graphite as anodes for lithium-ion batteries. *J. Power Sources* **75**, 64–72 (1998).

103. Swain, S. K. & Prusty, G. Characterizing oxygen-barrier polyacrylonitrile / graphite nanocomposites. 2–4
104. Tian, L., Wen, M. & Chen, J. Studies on disintegrating spherical fuel elements of high temperature gas-cooled reactor by a electrochemical method. *J. Nucl. Mater.* **432**, 113–119 (2013).
105. Welham, N. & Williams, J. Extended milling of graphite and activated carbon. *Carbon N. Y.* **36**, 1309–1315 (1998).
106. Yang, X., Zhang, P., Shi, C. & Wen, Z. Porous Graphite/Silicon Micro-Sphere Prepared by In-Situ Carbothermal Reduction and Spray Drying for Lithium Ion Batteries. *ECS Solid State Lett.* **1**, M5–M7 (2012).
107. Zhong, Y. & Shaw, L. A study on the synthesis of nanostructured WC–10 wt% Co particles from WO₃, Co₃O₄, and graphite. *J. Mater. Sci.* **46**, 6323–6331 (2010).
108. Zhou, P., Papanek, P. & Bindra, C. High capacity carbon anode materials: structure, hydrogen effect, and stability. *J. Power Sources* **68**, 296–300 (1997).
109. Zhu, H., Zhang, C., Tang, Y., Wang, J., Ren, B., Yin, Y. Preparation and thermal conductivity of suspensions of graphite nanoparticles. *Carbon N. Y.* **45**, 226–228 (2007).
110. Larese, J., Harada, M., Passell, L., Krim, J. & Satija, S. Neutron-scattering study of methane bilayer and trilayer films on graphite. *Phys. Rev. B* **37**, (1988).
111. Carneiro, K., Passell, L., Thomlinson, W. & Taub, H. Neutron-diffraction study of the solid layers at the liquid-solid boundary in ⁴He films adsorbed on graphite. *Phys. Rev. B* **24**, 1170–1176 (1981).
112. Wollan, E. O. & Shull, C. . The diffraction of neutrons by crystalline powders. *Phys. Rev.* **73**, 830–841 (1948).
113. Burian, A., Dore, J., Fischer, H. & Sloan, J. Structural studies of multiwall carbon nanotubes by neutron diffraction. *Phys. Rev. B* **59**, 1665–1668 (1999).
114. Kuno, M. *Introductory Nanoscience - Physical and Chemical Concepts*. 447 (Garland Science, Taylor & Francis Group, LLC, 2012).
115. Leach, A. R. *Molecular Modelling - Principles and Applications*. 773 (Pearson Education Limited, 2001).
116. Dolejš, D. & Manning, C. E. Thermodynamic model for mineral solubility in aqueous fluids: theory, calibration and application to model fluid-flow systems. *Geofluids* 20–40 (2010). doi:10.1111/j.1468-8123.2010.00282.x
117. Weinhold, F. Resonance Character of Hydrogen-bonding Interactions in Water and Other H-bonded Species. *Adv. Protein Chem.* **72**, 121–55 (2005).
118. Fennell, C. J., Kehoe, C. W. & Dill, K. a. Modeling aqueous solvation with semi-explicit assembly. *Proc. Natl. Acad. Sci. U. S. A.* **108**, 3234–9 (2011).

119. Cramer, C. J. & Truhlar, D. G. A universal approach to solvation modeling. *Acc. Chem. Res.* **41**, 760–8 (2008).
120. Basiuk, V. & Bassioux, M. Nanoassembly of meso-Tetraphenylporphines on Surfaces of Carbon Materials: Initial Steps as Studied by Molecular Mechanics and Scanning Tunneling Microscopy. *J. Nanosci. ...* **8**, 259–267 (2008).
121. Camellone, M. F. & Marx, D. On the Impact of Solvation on a Au/TiO₂ Nanocatalyst in Contact with Water. *J. Phys. Chem. Lett.* 514–518 (2013). at <<http://pubs.acs.org/doi/abs/10.1021/jz301891v>>
122. Silvestrelli, P. L. Van der Waals Interactions in DFT Made Easy by Wannier Functions. *Phys. Rev. Lett.* **100**, 053002:1–4 (2008).
123. Rubeš, M. & Bludský, O. Intermolecular p–p interactions in solids. *Phys. Chem. Chem. Phys.* **10**, 2611–2615 (2008).
124. Ribeiro, R., Peres, N., Coutinho, J. & Briddon, P. Inducing energy gaps in monolayer and bilayer graphene: Local density approximation calculations. *Phys. Rev. B* **78**, 075442 (2008).
125. Perumal, S., Minaev, B. & Ågren, H. Spin-spin and spin-orbit interactions in nanographene fragments: A quantum chemistry approach Spin-spin and spin-orbit interactions in nanographene fragments: **104702**, 10470201–10470215 (2012).
126. Grimme, S., Antony, J., Ehrlich, S. & Krieg, H. A consistent and accurate ab initio parametrization of density functional dispersion correction (DFT-D) for the 94 elements H–Pu. *J. Chem. Phys.* **132**, 154104 (2010).
127. Xiao, R., Tasnádi, F., Koepernik, K., Venderbos, J.W.F, Richter, M., Taut, M. Density functional investigation of rhombohedral stacks of graphene: Topological surface states, nonlinear dielectric response, and bulk limit. *Phys. Rev. B* **84**, 1–15 (2011).
128. Silvestrelli, P. L. Van der Waals interactions in density functional theory using Wannier functions. *J. Phys. Chem. A* **113**, 5224–34 (2009).
129. Baranov, A. I., Kohout, M., Planck, M., Physics, C. & Strasse, N. Electron Localization and Delocalization Indices for Solids. **2**, 12 (2011).
130. Andersson, Y., Langreth, D. & Lundqvist, B. van der Waals interactions in density-functional theory. *Phys. Rev. Lett.* **76**, 102–105 (1996).
131. Kysilka, J., Rubeš, M., Grajciar, L., Nachtigall, P. & Bludský, O. Accurate description of argon and water adsorption on surfaces of graphene-based carbon allotropes. *J. Phys. Chem. A* **115**, 11387–93 (2011).
132. Riley, K. E., Pitonák, M., Jurecka, P. & Hobza, P. Stabilization and structure calculations for noncovalent interactions in extended molecular systems based on wave function and density functional theories. *Chem. Rev.* **110**, 5023–63 (2010).

133. Rubes̆, M., Kysilka, J., Nachtigall, P. & Bludsky, O. DFT/CC investigation of physical adsorption on a graphite (0001) surface. *Phys. Chem. Chem. Phys.* **12**, 6438–6444 (2010).
134. Klomkliang, N., Do, D. D., Nicholson, D., Tangsathitkulchai, C. & Wongkoblaph, A. Multilayer adsorption of benzene on graphitised thermal carbon black—The importance of quadrupole and explicit hydrogen in the potential model. *Chem. Eng. Sci.* **69**, 472–482 (2012).
135. Wongkoblaph, A. & Do, D. D. The effects of curvature and surface heterogeneity on the adsorption of water in finite length carbon nanopores: a computer simulation study. *Mol. Phys.* **106**, 627–641 (2008).
136. Schrader, M. E. Ultrahigh-vacuum techniques in the measurement of contact angles. 5. LEED study of the effect of structure on the wettability of graphite. *J. Phys. Chem.* **84**, 2774–2779 (1980).
137. Kantorovich, L. *Quantum Theory of the Solid State: An Introduction*. 626 (Kluwer Academic Publishers, 2004).
138. Khadem, M. H. & Wemhoff, A. P. Molecular dynamics predictions of the influence of graphite stacking arrangement on the thermal conductivity tensor. *Chem. Phys. Lett.* **574**, 78–82 (2013).
139. Korkut, T. A molecular dynamics study about graphite and boron coated graphite at reactor temperatures. *Ann. Nucl. Energy* **63**, 100–106 (2014).
140. Shenogin, S., Gengler, J., Roy, a., Voevodin, a. a. & Muratore, C. Molecular dynamics studies of thermal boundary resistance at carbon–metal interfaces. *Scr. Mater.* **69**, 100–103 (2013).
141. Berber, S., Kwon, Y. & Tomanek, D. Unusually high thermal conductivity of carbon nanotubes. *Phys. Rev. Lett.* **84**, 4613–6 (2000).
142. Hone, J., Whitney, M., Piskoti, C. & Zettl, a. Thermal conductivity of single-walled carbon nanotubes. *Phys. Rev. B* **59**, R2514–R2516 (1999).
143. Chantrenne, P. & Barrat, J.-L. Analytical model for the thermal conductivity of nanostructures. *Superlattices Microstruct.* **35**, 173–186 (2004).
144. Liu, Z., Guo, Q., Shi, J., Zhai, G. & Liu, L. Graphite blocks with high thermal conductivity derived from natural graphite flake. *Carbon N. Y.* **46**, 414–421 (2008).
145. Wang, L. W., Tamainot-Telto, Z., Metcalf, S. J., Critoph, R. E. & Wang, R. Z. Anisotropic thermal conductivity and permeability of compacted expanded natural graphite. *Appl. Therm. Eng.* **30**, 1805–1811 (2010).
146. Wang, L. W., Metcalf, S. J., Critoph, R. E., Thorpe, R. & Tamainot-Telto, Z. Thermal conductivity and permeability of consolidated expanded natural graphite treated with sulphuric acid. *Carbon N. Y.* **49**, 4812–4819 (2011).

147. Prieto, R., Molina, J. M., Narciso, J. & Louis, E. Thermal conductivity of graphite flakes–SiC particles/metal composites. *Compos. Part A Appl. Sci. Manuf.* **42**, 1970–1977 (2011).
148. Wei, X. H., Liu, L., Zhang, J. X., Shi, J. L. & Guo, Q. G. Mechanical, electrical, thermal performances and structure characteristics of flexible graphite sheets. *J. Mater. Sci.* **45**, 2449–2455 (2010).
149. Yuana, G., Lia, X., Dong, Z., Westwood, A., Cui, Z., Cong, Y., Du, H., Kang, F. Graphite blocks with preferred orientation and high thermal conductivity. *Carbon N. Y.* **50**, 175–182 (2012).
150. Wei, Z., Ni, Z., Bi, K., Chen, M. & Chen, Y. Interfacial thermal resistance in multilayer graphene structures. *Phys. Lett. A* **375**, 1195–1199 (2011).
151. Magampa, P. P., Manyala, N. & Focke, W. W. Properties of graphite composites based on natural and synthetic graphite powders and a phenolic novolac binder. *J. Nucl. Mater.* **436**, 76–83 (2013).
152. Schelling, P. K., Phillpot, S. R. & Keblinski, P. Comparison of atomic-level simulation methods for computing thermal conductivity. *Phys. Rev. B* **65**, 144306 (2002).
153. Hwang, Y. J.; Ahn, Y. C.; Shin, H. S.; Lee, C. G.; Kim, G. T.; Park, H. S.; Lee, J. K. Investigation on characteristics of thermal conductivity enhancement of nanofluids. *Curr. Appl. Phys.* **6**, 1068–1071 (2006).
154. Shaikh, S., Lafdi, K. & Ponnappan, R. Thermal conductivity improvement in carbon nanoparticle doped PAO oil: An experimental study. *J. Appl. Phys.* **101**, 064302 (2007).
155. Zhang, Z. & Lockwood, Frances, E. ENHANCING THERMAL CONDUCTIVITY OF FLUIDS WITH GRAPHITE NANOPARTICLES AND CARBON NANOTUBE. *WO Pat. WO/2003/106,600* (2003). at
<<http://www.wipo.int/patentscope/search/en/WO2003106600>>
156. Xu, Y. & Chung, D. D. L. Increasing the specific heat of cement paste by admixture surface treatments. **29**, 1117–1121 (1999).
157. Lee, N. J., Yoo, J. W., Choi, Y. J., Kang, C. J., Jeon, D. Y., Kim, D. C., Seo, S., Chung, H. J. The interlayer screening effect of graphene sheets investigated by Kelvin probe force microscopy. *Appl. Phys. Lett.* **95**, 222107 (2009).
158. Yu, W. & Choi, S. U. S. The role of interfacial layers in the enhanced thermal conductivity of nanofluids: A renovated Hamilton-Crosser model. *J. Nanoparticle Res.* **6**, 355–361 (2004).
159. Tavman, I., Aydogdu, Y. & Kök, M. Measurement of heat capacity and thermal conductivity of HDPE/expanded graphite nanocomposites by differential scanning calorimetry. *Arch. Mater. ...* **50**, 56–60 (2011).
160. Desai, S. & Njuguna, J. Enhancement of thermal conductivity of materials using different forms of natural graphite. *IOP Conf. Ser. Mater. Sci. Eng.* **40**, 012017 (2012).

161. Shahil, K. M. F. & Balandin, A. a. Graphene-multilayer graphene nanocomposites as highly efficient thermal interface materials. *Nano Lett.* **12**, 861–7 (2012).
162. Zhu, H., Zhang, C., Tang, Y., Wang, J., Ren, B., Yin, Y. Preparation and thermal conductivity of suspensions of graphite nanoparticles. *Carbon N. Y.* **45**, 226–228 (2007).
163. Zhang, Y., Mann, V., Reed, D., Walton, A. Hydrogen storage properties of nanostructured graphite-based materials. *2009 Int. Conf. Sustain. Power Gener. Supply* 1–4 (2009). doi:10.1109/SUPERGEN.2009.5348032
164. Putnam, S. A., Cahill, D. G., Braun, P. V., Ge, Z. & Shimmin, R. G. Thermal conductivity of nanoparticle suspensions. *J. Appl. Phys.* **99**, 084308 (2006).
165. Lindemann, A. Application Note: New Sample Holder for Low-Viscosity Liquids Part 1 – Principle and Test Results of Water. 1–3 (2013).
166. Berman, R. The thermal conductivity of some polycrystalline solids at low temperatures. *Proc. Phys. Soc. Sect. A* **1029**, (1952).
167. Abdallah, W., Buckley, J. & Carnegie, A. Fundamentals of wettability. *Technology* 44–61 (1986). at <http://www.geodiamond.com/~media/Files/resources/oilfield_review/ors07/sum07/p44_61.pdf>
168. Attension. Wettability | Attension Tensiometers. 2013 at <<http://www.attension.com/applications/measurements/wettability>>
169. PerkinElmer Inc. Thermogravimetric Analysis - A Beginner ' s Guide. (2013). at <http://www.perkinelmer.com/CMSResources/Images/44-74556GDE_TGABeginnersGuide.pdf>
170. Sinhamahapatra, A., Giri, A. K., Pal, P., Pahari, S. K., Bajaj, H. C., Panda, A. B. A rapid and green synthetic approach for hierarchically assembled porous ZnO nanoflakes with enhanced catalytic activity. *J. Mater. Chem.* **22**, 17227–17235 (2012).
171. Zhang, Y., Hu, W., Li, B., Peng, C., Fan, C., Huang, Q. Synthesis of polymer-protected graphene by solvent-assisted thermal reduction process. *Nanotechnology* **22**, 345601 (2011).
172. Ding, J. N., Liu, Y. B., Yuan, N. Y., Ding, G. Q., Fan, Y., Yu, C. T. The influence of temperature, time and concentration on the dispersion of reduced graphene oxide prepared by hydrothermal reduction. *Diam. Relat. Mater.* **21**, 11–15 (2012).
173. Du, F. P., Wang, J. J., Tang, C. Y., Tsui, C. P., Zhou, X. P., Xie, X. L., Liao, Y. G. Water-soluble graphene grafted by poly(sodium 4-styrenesulfonate) for enhancement of electric capacitance. *Nanotechnology* **23**, 475704 (2012).
174. Gogoi, P., Boruah, M., Bora, C. & Dolui, S. K. Jatropha curcas oil based alkyd/epoxy resin/expanded graphite (EG) reinforced bio-composite: Evaluation of the thermal, mechanical and flame retardancy properties. *Prog. Org. Coatings* 1–7 (2013). doi:10.1016/j.porgcoat.2013.08.006

175. Guo, Y., Guo, S., Ren, J., Zhai, Y., Dong, S., Wang, E. Functionalized Graphene Nanosheets with High Supramolecular Recognition Capability: Synthesis and Host– Guest Inclusion for Enhanced Electrochemical. *ACS Nano* **4**, 4001–4010 (2010).
176. Jeong, H. K., Lee, Y. P., Jin, M. H., Kim, E. S., Bae, J. J., Lee, Y. H. Thermal stability of graphite oxide. *Chem. Phys. Lett.* **470**, 255–258 (2009).
177. Li, Y., Zou, J., Zhou, S., Chen, Y., Zou, H., Liang, M., Luo, W. Effect of expandable graphite particle size on the flame retardant, mechanical, and thermal properties of water-blown semi-rigid polyurethane foam. *J. Appl. Polym. Sci.* **39885**, n/a–n/a (2013).

4. EXPERIMENTAL METHODS

Four graphite powder samples were obtained, each supplied by a different manufacturer. The details of these powder samples are briefly summarised in Table 4-1.

Table 4-1: Details of graphite nanopowder samples purchased

<i>Supplier</i>	<i>Product code</i>	<i>Approximate particle size</i>	<i>Particle morphology</i>	<i>Purity (%)</i>	<i>Origin</i>
<i>US Research Nanomaterials, Inc.</i>	1058	400 nm-1.2 μm	flaky	99.9	Natural
<i>Mk NANO</i>	MKN-CG-050	50nm	flaky	99.5	Synthetic
<i>Nanostructured & Amorphous Materials, Inc.</i>	1250HT	400nm	flaky	99.9	Natural
<i>Pebble Bed Modular Reactor Project (PBMR, SA)</i>	Nuclear grade graphite (NGG), GPN-B-G01	14.9 μm^a	Unknown	>99	Natural

For each of the samples listed in Table 4-1, three different physical measurements were undertaken. These included:

- a) A spectroscopic vibrational analysis (IR and Raman)
- b) A Cu-K α & Co-K α powder X-ray diffraction (XRD) analysis
- c) A molecular porosimetry (BET) surface analysis

The data produced by the XRD analysis in combination with that of the molecular porosimetry analysis would be used to determine the crystallite shape, size, surface area and crystallographic structure of each of the samples. Each sample can then be represented (with a reasonable amount of accuracy, on the atomic scale), within a computational modelling environment (with a defined model size). Using the information produced by the experiments, an appropriate sample would be prepared for further experimental analysis, such as:

- a) A thermo-gravimetric analysis (TGA)
- b) A differential scanning calorimetry (DSC) Analysis
- c) A laser flash analysis (LFA)
- d) Computational modelling

^a Particle Size distribution analysis was undertaken by Dr Heidi Rolfes, Chemical Engineering Department, University of Pretoria, South Africa, using a *Malvern Mastersizer 3000*. Water was used as a dispersant, whilst ethanol was used to wet the sample and *Triton X-100* was used as a surfactant. Two runs were performed, one utilising sonication and the other not.

4.1. MOLECULAR RESOLUTION POROSIMETRY ANALYSIS

The molecular resolution porosimetry analysis of each of the graphite powder samples, listed in Table 4-1, was carried out using the Quantachrome NOVA 1000e gas adsorption analyser, along with the Quantachrome sample cell seal kit, at the University of Pretoria. The NOVAVin2-P software was used. Nitrogen (N₂) was used as the adsorbate. Outgassing of the samples was carried out at 80°C for approximately two hours. Porosimetry data was generated using seven relative pressure points (P/P₀) between the values of 0.025 and 0.3. A multipoint BET (MBET) analysis of the porosimetry data generated was used to determine the total specific surface area of the powders^b.

4.2. POWDER X-RAY DIFFRACTION (XRD) ANALYSIS

All four samples were prepared for XRD analysis using a back loading preparation method, without further micronising. The samples were each analysed using a Bruker D8 Advance powder diffractometer with 2.2kW of incident Ni-filtered Cu-K α radiation ($\lambda = 1.5406 \text{ \AA}$). A LynxEye detector with 3.7° of active area was used. A fixed divergence slit (0.2 mm, 0.1°), a receiving slit (0.1 mm) and Soller slits (2.5°) were applied in the primary and secondary sides of the beam path. An angular range of $8^\circ \leq 2\theta \leq 132^\circ$ with a step size 0.008° 2 θ and a 5-sec. residency (i.e. scan step) time was utilised^c.

The phases were identified using Bruker DIFFRAC.EVA software for all samples. The relative mean crystallite size and the unit cell lattice parameters were estimated using DIFFRAC.TOPAS V4.2 software, applying the Rietveld method and the Scherrer equation.

4.3. FOURIER TRANSFORM INFRARED (FTIR) AND RAMAN VIBRATIONAL SPECTRA CHARACTERIZATION

The (transmittance) infrared spectrum of each of the graphite powder samples listed in Table 4-1 was determined using the Vertex 70v (Bruker) Spectrometer^d, containing the sample within a macro-sample compartment with a Diamond ATR cell. The diameter of the contact area was 2 mm. The sample compartment was evacuated during the data acquisitions. Spectra were

^b A cross correlating analysis was performed at NECSA on a graphite nanopowder sample, to confirm the accuracy of the instrument at the University of Pretoria.

^c The powder XRD analysis was carried out by Maria Atanasova at the Council for Geoscience, Pretoria.

^d FTIR and Raman analysis was performed by the author, under the supervision of Dr J.Nel and Dr L.Prinsloo, Physics Department, University of Pretoria, South Africa.

recorded with 32 acquisitions at a resolution of 4cm^{-1} and over a spectral range of 400 to 4000cm^{-1} wave numbers.

The Raman analysis was carried out using the Horiba Jobin Yvon T64000 software. A green laser, with an excitation wavelength of 514nm , a beam current of 10mW and a lens with magnification strength of 100, was used on all four of the samples. The total acquisition time was 100 seconds and the spectral range was 50 to 3500cm^{-1} . The samples, as received, were each placed on a glass test plate and flattened (by pressing down onto the sample with a second glass test plate) to decrease scattering of the emitted radiation, allowing for stronger Raman spectra to be obtained.

4.4 THERMO-GRAVIMETRIC ANALYSIS (TGA)

A TGA analysis of graphite powder and water mixture samples^e using the SDT Q600 V20.9 module, manufactured by TA Instruments, was carried out. A $50\text{ }\mu\text{L}$ platinum crucible was used to contain the samples. Nitrogen was selected as the purge gas, with a flow rate of $20\text{mL}/\text{min}$, to eliminate the possibility of oxidation. Demineralised water was used in the graphite-water mixtures, allowing for consistency between the various samples prepared and to avoid the presence of metallic elements that could alter the thermal interaction of the graphite-water mixture. Before any graphite-water mixtures were analysed, TGA analyses of (demineralised) water were performed with a heating rate of $1\text{ to }2^\circ\text{C}/\text{min}$, in order to determine the characteristic TGA-curves of bulk water. These characteristic curves were superimposed with the TGA curves produced by the graphite-water samples, allowing one to observe how the presence of the graphite powder influences the rate at which water is expelled from the sample. Isothermal runs were also conducted at a temperature of $40\text{ to }60^\circ\text{C}$ for prolonged periods (under computer control), allowing for the effective release of excess water and the observation of the point at which the minimum amount of “surface” water (which is not necessarily a monolayer) is present in the graphite-water sample. This process provided an effective water surface-wetting (mass ratio) parameter for graphite.

4.5 DIFFERENTIAL SCANNING CALORIMETRY (DSC)

A differential scanning calorimetric analysis was performed on samples containing a mixture of nuclear grade graphite (NGG) and de-ionised water, using the C80 Calvet calorimeter,

^e TGA analysis undertaken by Mr. Andrew Pienaar, Department of Applied Chemistry, NECSA, Pelindaba, South Africa.

manufactured by SETARAM Instrumentation^f. A sapphire sample was also analysed, as a reference, for heat capacitance calculation purposes. The graphite and graphite-water samples were analysed inside a Hastalloy sample vessel. The sample vessel was hermetically sealed using Hastalloy caps and polymer O-rings. After each of the samples were loaded, the sample vessels were heated to and held at the desired starting temperature to allow for equilibration, after which the samples were heated at a rate of 0.5°C /min.

4.6 LASER FLASH ANALYSIS (LFA)

For the purposes of this thesis, LFA measurements were not carried out. This is due to the lack of availability of a LFA apparatus within the country or overseas. These measurements will be carried out at a later stage and form part of a second publication. For a complete description of the laboratory parameters required, refer to Annexure C.

^f DSC analysis undertaken by Mr. Andrew Pienaar, Department of Applied Chemistry, NECSA, Pelindaba, South Africa.

5. EXPERIMENTAL RESULTS AND DISCUSSION

5.1. MOLECULAR RESOLUTION POROSIMETRY ANALYSIS

The results of the molecular resolution porosimetry analysis of all four graphite powder samples are summarised in the table below.

Table 5-1: Experimentally determined surface area of graphite nanopowder samples⁸

Supplier	Product code	Approximate particle size	Surface area (m ² /g)
US Nano	1058	400 nm -1 200 nm	13.573
Mk Nano	MKN-CG-050	50 nm	15.382
Nano Amor	1250HT	400 nm	16.064
NGG	GPN-B-G01	14 950 nm	5.1560

5.2. POWDER X-RAY DIFFRACTION (XRD) ANALYSIS

The results of the Cu-K_α XRD analysis of all four samples are shown in Figure 5-1 below.

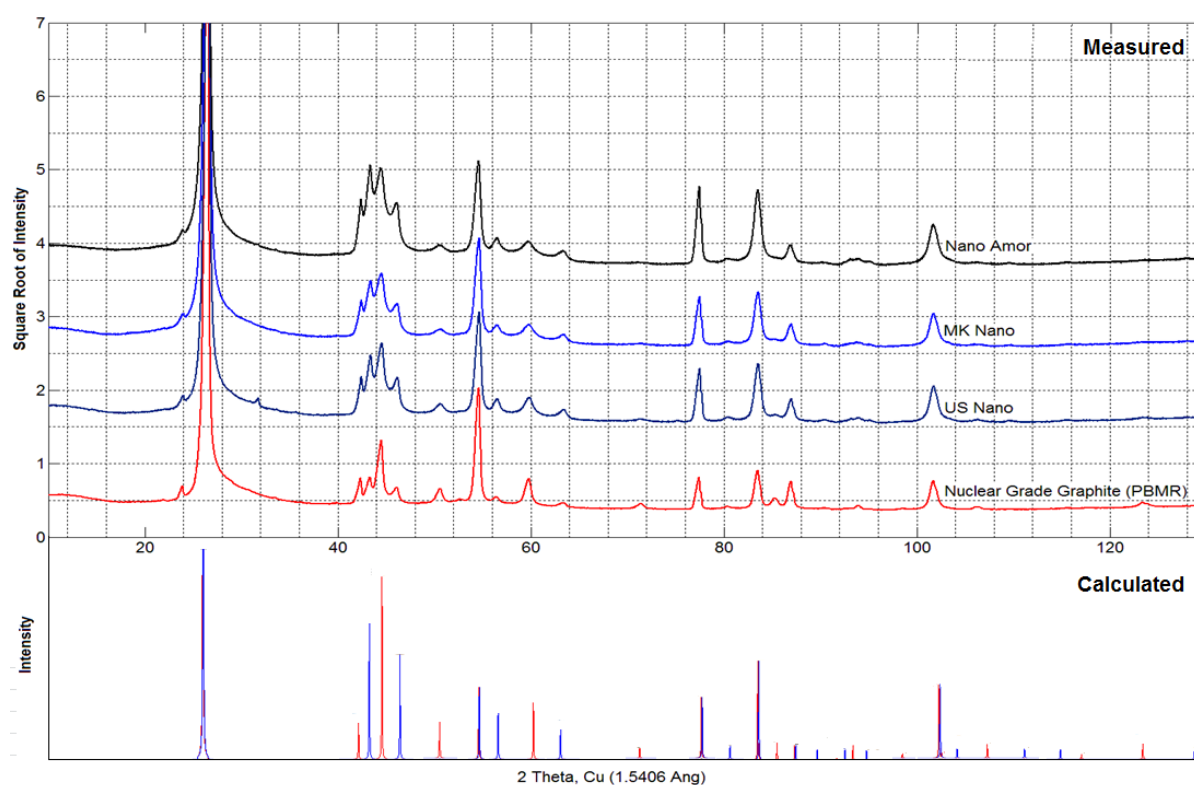


Figure 5-1: XRD Analysis of all graphite powder samples (top), followed by the calculated diffraction pattern (bottom) produced using PowderCell

⁸ Specific surface areas of each of the graphite powders are similar to that observed by several authors^{39–44}.

Table 5-2^h: Experimentally observed diffraction indices for all four graphite samples applying Cu K_{α1}-radiation at $\lambda=1.5406 \text{ \AA}$. Reflections with a relative intensity >0.4 are listed

Diffraction Index	NGG		MK Nano		Nano Amor		US Nano	
	2θ	$\sqrt{\text{Intensity}}$	2θ	$\sqrt{\text{Intensity}}$	2θ	$\sqrt{\text{Intensity}}$	2θ	$\sqrt{\text{Intensity}}$
#{009}	23.9	0.7002	24.03	1.051	23.93	1.186	23.98	0.9347
R{003}/H{002}	26.53	10	26.61	10	26.56	10	26.61	10
#{0,0,12}							31.77	0.8965
H{100}	42.35	0.8127	42.48	1.229	42.42	1.604	42.44	1.18
R{101}	43.33	0.8114	43.41	1.497	43.38	2.067	43.4	1.483
H{101}	44.51	1.32	44.52	1.593	44.43	2.028	44.58	1.642
R{102}	46.15	0.6818	46.15	1.179	46.13	1.555	46.16	1.176
H{102}	50.62	0.6607	50.67	0.8369	50.48	0.986	50.59	0.8191
#{0,1,11}	52.65	0.5219						
H{004}	54.62	2.036	54.67	2.067	54.6	2.122	54.67	2.064
R{104}	56.45	0.5551	56.55	0.8966	56.52	1.079	56.53	0.8893
H{103}	59.82	0.7976	59.8	0.8999	59.71	1.032	59.85	0.9074
R{105}	63.4	0.4731	63.47	0.7614	63.31	0.904	63.47	0.7397
H{104}	71.38	0.4612	71.57	0.6421	71.19	0.7537	71.47	0.6124
#{0,0,27}*							75.33	0.5935
H{110}/R{110}	77.45	0.8149	77.51	1.275	77.49	1.776	77.51	1.295
R{107}	80.43	0.4221	80.47	0.6762	80.39	0.8008	80.42	0.6445
H{112}	83.55	0.9138	83.58	1.34	83.57	1.734	83.62	1.362
H{105}/H{006}	85.31	0.5388					85.35	0.6743
H{006}	86.99	0.7646	86.99	0.9021	86.84	0.9841	87.02	0.8873
R{108}	90.43	0.4046	90.44	0.6411	90.3	0.747	90.59	0.6071
#{024}*					93.1	0.7926	93.2	0.6183
H{201}	94	0.437	94.13	0.6571	94.01	0.7953	94.05	0.6344
R{202}			95.21	0.6292	95.23	0.7589	95.14	0.6028
H{202}	98.61	0.3941						
H{114}/R{116}	101.7	0.7675	101.7	1.051	101.7	1.26	101.7	1.06
H{203}	106.3	0.418	106.5	0.6309	106.3	0.7499	106.3	0.6093
R{205}	109.7	0.3883	109.7	0.62	109.6	0.7359	109.7	0.5932
R{10,10}	115.4	0.4029	115.8	0.6369	115.6	0.7513	115.6	0.6013
H{204}	117.6	0.4068						
H{107}	123.4	0.4791	123.7	0.6658	123.8	0.7808	123.4	0.6358
R{207}	128.2	0.4278	128.5	0.6765	127.8	0.8016	128.1	0.6392

^h # Nitrated-graphite phase: ICSD-28417 (Space group R-3m). * Higher order reflections display a discrepancy in their absolute diffraction index positions, due to the trace composition of this phase, which should not be used as an unambiguous phase identification.

When comparing the patterns produced by each of the samples, it can be seen that the crystallinity of the NGG sample is high and/or has a larger constituency for at least one crystallite phase --- particle size of the NGG sample is also far greater (Table 5-1). Hence, the Cu-K α PXRD pattern of the NGG sample was analysed (XRD captured using Co-K α radiation to resolve unnecessary peak overlap of the two phasesⁱ) in more detail. The XRD-pattern of the NGG sample was superimposed with that of known hexagonal and rhombohedral graphite unit cells, obtained from various crystallographic databases. The Rietveld refinement performed on all four graphite samples yielded the respective phase compositions listed in Table 5-3.

Table 5-3: Phase compositions of four graphite samples, derived from Rietveld analysis (2H refers to hexagonal phase, 3R refers to rhombohedral phase)

Sample ID	Rietveld analysis R (wt) %	Cu K- α radiation --- Phase constituencies (% m/m)			
	Space Grp. C-axis polymorph	P63mc (H) c=6.73 Å	R-3mR c=33.45 Å	P63/mmc (H) c=12.30 Å	R-3mR c=10.05 Å
NanoAmorph	6.13	99.43	0.20	0.36	0.01
MK-Nano	3.74	98.94	0.69	0.36	0.01
US Nano	5.28	87.56	12.05	0.38	0.002
NNG	8.08	99.55	0.24	0.20	0.002

A significant amount of peak broadening and a slight mismatch between the library pattern peaks and the sample pattern peaks is observed when analysing the XRD pattern produced by the NGG sample. This suggests that a degree of amorphous character may exist, along with crystalline phases of graphite present within the powder, also attributed to small graphitic crystallite sizes, particle disorder and the presence of lattice strain⁸⁻¹². A more trivial explanation of the peak-position mismatch may lie in the fact that the positions of the peaks are dictated by the structure of the graphite unit cell. Due to the known variability of graphitic lattice parameters (Table 5-7) and phases present, it is simply not possible to obtain a single, characteristic, powder pattern of graphite with no variability in peak positions (or intensities).

Severe diffraction peak overlap is observed between the hexagonal phases of space groups 194 (P63/mmc) and 186 (P63/mc). Graphite phase 186 is considered a subgroup of phase 194. A minute elevation in the carbon C-axis coordinate of 0.005 off from the unit-cell origin and a subsequent unit-cell shift of a quarter in C-axis (noted for both carbon-atoms in the asymmetric unit), is required to reach the special positions of: C1= $\frac{1}{3}, \frac{2}{3}, 1/4$ and C2=0,0,1/4 lapsing into space group 194. With similar unit cell dimensions, it is fair to assume that these two hexagonal phases will not be sufficiently resolved by applying powder X-ray diffraction techniques, other

ⁱ Performed by Mrs Wiebke Grote, Geology Department, University of Pretoria.

than focusing on extreme order reflections which will lack adequate intensity. The hexagonal phases are therefore reported here as the single phase of hexagonal space group 194 (P63/mmc). For the sake of completion, both phases (186 and 194) are reported with respect to their calculated diffraction indices in Table 5-3.

In order to determine which of the lattice planes within the polycrystalline structure of the NGG particles were responsible for the variation in peak positions within the XRD pattern, the expected Bragg angles (θ) for a hexagonal as well as rhombohedral unit cell of graphite were calculated using the PowderCell software program, which calculates the peak positions based on the following equations, used in combination with Bragg's Law (equation 5).

For a hexagonal unit cell ⁹:

$$\frac{1}{d^2} = \frac{4}{3a^2}(h^2 + hk + k^2) + \frac{l^2}{c^2} \quad (2)$$

For a rhombohedral unit cell ⁹:

$$\frac{1}{d^2} = \frac{(h^2 + k^2 + l^2) \sin^2 \alpha + 2(hk + kl + hl)(\cos^2 \alpha - \cos \alpha)}{a^2(1 - 3 \cos^2 \alpha + 2 \cos^3 \alpha)} \quad (3)$$

Where: d = Inter-planar spacing (Å)

h, k, l = Miller indices

a = Basal (a or b) unit cell lengths (Å)

By combining each of the two equations above with Bragg's Law, one is able to calculate the expected Bragg angles, listed in Table 5-4 and plotted in Figure 5-2. Highlighted cells indicate peak overlap.

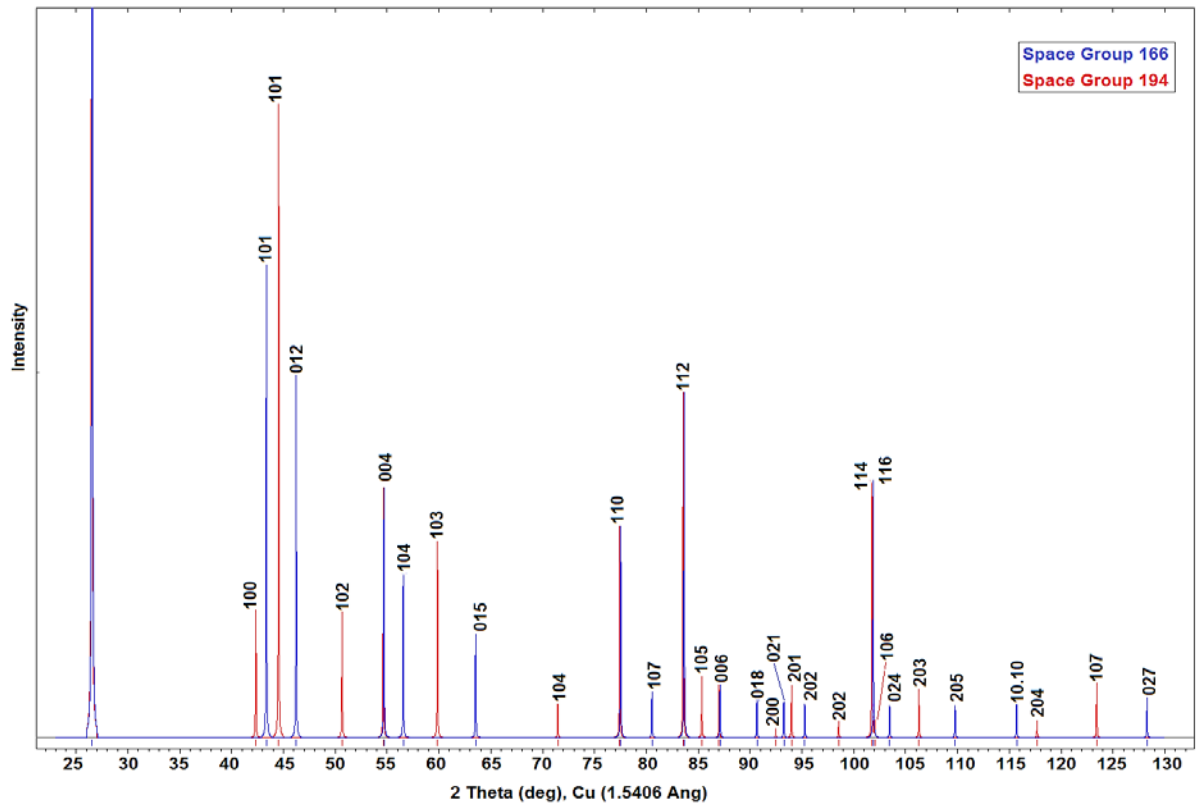


Figure 5-2: Cu-K α XRD powder pattern calculated using PowderCell, for both unrefined space groups.

Table 5-4: Two-Theta (2θ) X-ray diffraction peak positions for the hexagonal and rhombohedral graphite phases from Cu $K\alpha_1$ -radiation at $\lambda=1.5406\text{\AA}$, calculated using the PowderCell software. Only symmetry unique reflections with a relative intensity >0.2 are listed

Phase			<i>Hexagonal (194, $P6_3/mmc$)</i>			<i>Hexagonal (186, $P6_3/mc$)</i>			<i>Rhombohedral (166, $R-3m$)</i>		
h	k	l	2θ Angle ($^\circ$)	Relative Intensity	d (\AA)	2θ Angle ($^\circ$)	Relative Intensity	d (\AA)	2θ Angle ($^\circ$)	Relative Intensity	d (\AA)
0	0	2	26.53	100	3.36	26.23	100	3.395			
0	0	3							26.56	100	3.354
1	0	0	42.34	3.53	2.13	42.21	3.48	2.139			
1	0	1	44.53	17.39	2.03	44.37	17.08	2.04	43.36	12.92	2.085
1	0	2	50.66	3.47	1.8	50.38	3.47	1.81	46.22	10.04	1.962
0	0	4	54.64	6.83	1.68	53.97	6.9	1.698			
1	0	3	59.85	5.37	1.54	59.4	5.35	1.555			
1	0	4	71.46	0.94	1.32	70.8	0.97	1.33	56.55	4.48	1.626
1	1	0	77.44	5.8	1.23	77.18	5.66	1.235	77.51	5.81	1.231
1	1	2	83.56	9.47	1.16	83.17	9.23	1.161			
1	1	3							83.64	9.47	1.155
1	0	5	85.44	1.69	1.14	84.43	1.68	1.146	63.54	2.86	1.463
0	0	6	87.09	1.44	1.12	85.79	1.42	1.132	54.69	6.83	1.677
0	0	9							87.11	1.44	1.118
1	0	8							90.66	1	1.083
2	0	0	92.48	0.24	1.07	92.14	0.23	1.07			
2	0	1	93.99	1.42	1.05	93.62	1.37	1.057	93.25	0.96	1.06
2	0	2	98.55	0.45	1.02	98.07	0.43	1.02	95.27	0.93	1.044
1	1	4	101.75	7.05	0.99	100.95	6.81	0.999			
1	1	6							101.88	10.22	0.992
1	0	6	102.04	0.44	0.99	100.72	0.46	1			
2	0	3	106.28	1.31	0.96	105.61	1.26	0.967			
2	0	4	117.68	0.47	0.9	116.7	0.45	0.905	103.45	5.08	0.981
2	0	5							109.76	4.97	0.942
1	0	10							115.7	4.87	0.91
1	0	7	123.42	1.5	0.88	121.37	1.41	0.883	80.54	1.3	1.192
2	0	7							128.28	4.72	0.856

In order to determine the mean crystallite size for each of the four graphite samples, the Rietveld refinement method, embedded with the Double Voigt approach ^j, was used for the micro-structure analysis. The Rietveld refinement method was also used to determine the

^j Balzar, Davor. 1999. Voigt-Function Model in Diffraction Line-Broadening Analysis. *In Microstructure Analysis from Diffraction, International Union of Crystallography, 1999.*, edited by R. L. Snyder, H. J. Bunge & J. Fiala.

lattice parameters of each of the four graphite samples. Finally, Bragg's Law was used to determine the inter-planar spacing of the graphene sheets for each of the four graphite samples.

Due to the fact that:

- (i) the strongest peak is produced by both the hexagonal (002) and rhombohedral (003) planes of graphite; and
- (ii) the weight percentage concentration of the hexagonal graphite phase was determined to be significantly larger than that of the rhombohedral phase (Table 5-3);

the calculations performed to determine the mean crystallite sizes and unit cell lattice parameters were based upon the presence of only one phase, hexagonal graphite, being present within the sample ¹³. This reduction was necessary in order to simplify the problem of determining the amount of surface area provided by each of the carbon layers that constitute the graphite crystallite (carried out further on in the chapter). However, a proportional correction can be applied, if necessary, to account for the rhombohedral phase component.

The Scherrer and Bragg equations (embedded in the overall Double Voigt method) used for the calculation of the mean crystallite size, L , and inter-planar spacing, d , respectively, are given below.

The Scherrer equation is as follows:

$$L = \frac{\lambda K}{\beta \cos \theta} \quad (4)$$

where λ is defined as the wavelength of the incident radiation (Cu-K α , 1.541 Å), β the full peak width at half maximum (in radians), θ the Bragg angle and K the Scherrer constant, equal to 0.89 (for crystallites whose shape is assumed to be spherical).

Bragg's Law is stated as follows:

$$d = \frac{\lambda}{2 \sin \theta} \quad (5)$$

where λ is defined as the wavelength of the incident radiation, θ the Bragg diffraction angle and d as the inter-planar spacing (Å).

Table-5-5: Calculated (mean) crystallite size and inter-layer distance of each graphite powder sample using XRD

Sample code	Bragg diffraction angle (degrees)	Mean crystallite size, L (nm)		Inter-layer spacing, d
		Scherrer	Rietveld	d (Å) [002]
US Nano 1058	13.305	23.29	23.6	3.347
Mk Nano CG-050	13.305	21.23	20.75	3.347
Nano Amor 1250HT	13.28	23.50	20.4	3.353
NGG	13.265	23.83	23.94	3.357

Table-5-6: Calculated X-ray lattice parameters of each graphite powder sample using XRD (Rietveld refinement)

Sample code	Unit cell dimensions (hexagonal)	
	a (Å)	c (Å)
US Nano 1058	2.467	6.765
Mk Nano CG-050	2.466	6.763
Nano Amor 1250HT	2.465	6.773
NGG	2.465	6.744

When considering published lattice parameters for hexagonal graphite, it is observed that for all four samples the results of the XRD analysis produced using the Rietveld refinement and Bragg's Law are in close agreement with published figures. The percentage error between each of the experimentally determined and published lattice parameters were determined and summarised in Table 5-7.

Table-5-7: Percentage errors between experimentally determined and published lattice parameters

Literature	Lattice parameter (This analysis)	Literature Source				
		RRUFF (2012) ¹⁴	Volkova, et al. (2011) ¹³	WYCKOFF (1963) ¹⁵ ; Kwiecińska and Petersen (2004) ¹⁶ ; Gray et al. (2009) ¹⁷	Criddle and Stanley (1993) ¹⁸ ; Trucano and Chen (1975) ¹⁹	Hatton et al. (2011) ²⁰
Sample	a (Å)	2.450	2.456–2.460 (avg. 2.458)	2.460	2.464	2.470
US Nano 1058	2.467	0.694	0.732	0.285	0.122	0.121
Mk Nano CG-050	2.466	0.653	0.773	0.244	0.081	0.162
Nano Amor	2.465	0.612	0.814	0.203	0.041	0.202
NGG	2.465	0.612	0.814	0.203	0.041	0.202
Sample	c (Å)	6.713	6.698–6.708 (avg. 6.703)	6.710	6.711	6.790
US Nano 1058	6.765	0.775	0.925	0.820	0.805	0.368
Mk Nano CG-050	6.763	0.745	0.895	0.790	0.775	0.398
Nano Amor	6.773	0.894	1.044	0.939	0.924	0.250
NGG	6.744	0.462	0.612	0.507	0.492	0.677
Sample	d (Å){002}	3.331	3.349–3.354 (avg. 3.352)	3.330 -3.354 (avg. 3.342)	-	-
US Nano 1058	3.347	0.480	0.149	0.150	-	-
Mk Nano CG-050	3.347	0.480	0.149	0.150	-	-
Nano Amor	3.353	0.660	0.030	0.329	-	-
NGG	3.357	0.781	0.149	0.449	-	-

When correlating the calculated dimensions of the hexagonal unit cell to those published in literature, a variance no greater than approximately 1 percent is observed. When considering the d (i.e. inter-planar) lattice parameter, the smallest percentage error is that of the NGG sample whose crystallite size is the largest of all the graphite powder samples. This may be explained by a study performed by Kaneko et al. (1992)^{21,22} on micro-crystalline graphite structures which indicated that for a crystallite size of less than 5 nm a larger inter-planar distance (i.e. d – spacing) is observed when compared to that of bulk or macro-crystalline graphite structures, attributed to weaker alignment of the graphene layers and a greater averaging estimate.

The specific surface areas determined from the MBET were also used in conjunction with the mean crystallite sizes (calculated using the XRD results) to determine the surface area per

graphitic crystallite and per corresponding graphene layer. The procedure for this calculation is described below, specifically for the case of the NGG sample and the hexagonal unit cell. The results of the calculation for the remaining samples are tabulated thereafter.

The following data was used for the calculation:

Table-5-8: Data used in the calculation of the crystallite surface area

Nuclear grade graphite (NGG)			
Constant	Symbol	Value	Units
Avogadro's number	N_A	6.022E+23	Atoms/mol
Neutral atomic mass of carbon	M_{C-12}	12.011	g/mol
No. of atoms per unit cell (Space group 194 P6 ₃ /mmc)	Z_u	4	#
Unit cell lattice parameter (Cell edge)	a	2.465	Å
Unit cell lattice parameter (Cell edge)	c	6.744	Å
Unit cell lattice parameter (Angle)	α	120	Degrees
Mean crystallite size (Scherrer and Rietveld average)	$L_a = L_c$	238.85	Å
Specific surface area	SSA	5.156E+18	nm ² /g

First, the volume of the hexagonal unit cell (see Figure 5-4), V_u , is determined using the formula

$$V_u = ac(\perp h) \quad (6)$$

where $\perp h$ is the orthonormal distance between the two vertical faces of the unit cell. To determine this distance simple trigonometry is applied.

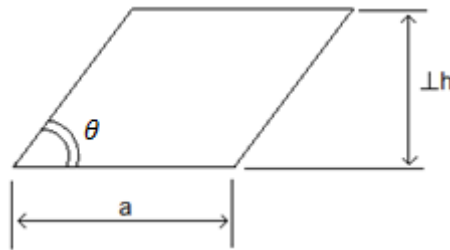


Figure 5-3: Basal plane of hexagonal unit cell

$$\begin{aligned}
 \perp h &= a \sin \theta \\
 &= 2.465 \sin 60 \\
 &= 2.1347 \text{ Å}
 \end{aligned} \quad (7)$$

Thus

$$\begin{aligned}
 V_u &= ac(\perp h) \\
 &= (2.465)(6.744)(2.1347) \\
 &= 35.488 \text{ Å}^3
 \end{aligned} \quad (8)$$

The volume of the crystal (V_c) is determined in a similar manner by assuming that the crystal is of a shape similar to that of the unit cell.

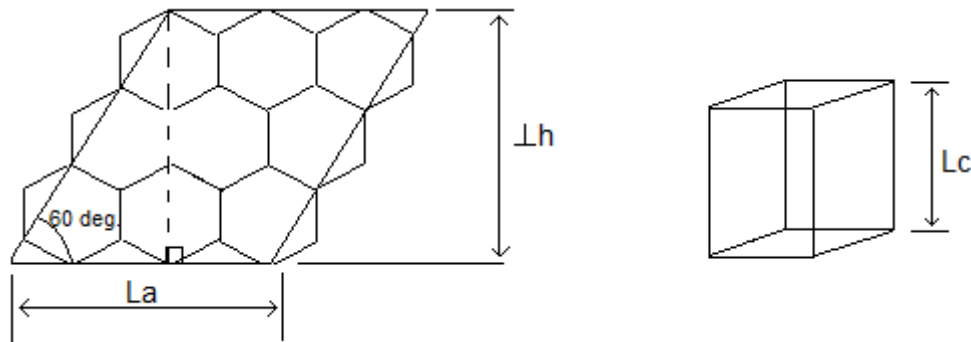


Figure 5-4: Assumed shape of graphite crystallite

Hence,

$$\begin{aligned}
 V_c &= L_a L_c (\perp h) \\
 &= (238.85)^2 (238.85 \sin 60) \\
 &= 11\,800\,661.9 \text{ \AA}^3 \\
 &= 11\,800.6619 \text{ nm}^3
 \end{aligned}
 \tag{9}$$

The mass of the unit cell, m_u , is then determined using Avagadro's Law.

$$\begin{aligned}
 m_u &= \frac{Z_u M_{C-12}}{N_A} \\
 &= \frac{(4)(12.011)}{6.022 \times 10^{23}} \\
 &= 7.97808 \times 10^{-23} \text{ gram}
 \end{aligned}
 \tag{10}$$

The number of unit cells, n_u , present within a single crystal is then determined as:

$$\begin{aligned}
 n_u &= \frac{V_c}{V_u} \\
 &= \frac{11\,800\,661.9}{35.488} \\
 &= 332\,525.0198 \cong 332\,525
 \end{aligned}
 \tag{11}$$

Using the above results, the mass of a single graphite crystal, m_c , may be determined.

$$\begin{aligned}
 m_c &= m_u n_u & (12) \\
 &= (7.97808 \times 10^{-23})(332\,525) \\
 &= 2.65285 \times 10^{-17} \text{ gram}
 \end{aligned}$$

The total planar surface area (presented by the combined collection of the two-dimensional graphene sheets) of a single graphite crystal, PSA_T , is determined as:

$$\begin{aligned}
 PSA_T &= (SSA)m_c & (13) \\
 &= (5.156 \times 10^{18})(2.65285 \times 10^{-17}) \\
 &= 136.7809 \text{ nm}^2 \\
 &= 13\,678.09 \text{ \AA}^2
 \end{aligned}$$

The number of unit cells in the vertical direction of the crystallite, referred to as n_v , are:

$$\begin{aligned}
 n_v &= \frac{L_c}{c} & (14) \\
 &= \frac{238.85}{6.744} \\
 &= 35.42 \cong 35 \text{ unit cells}
 \end{aligned}$$

The final step of this calculation involves the assumption that the hexagonal unit cell at the base of a crystal provides two planes (with a single plane being defined as a fictitious surface lying either in-between two “graphene” sheets or as a combination of two fictitious surfaces lying at the top and bottom of the basal planes and intercalated surfaces of the supercell structure), n_p , on which molecules (such as H_2O molecules) may be adsorbed, with an additional two planes for each of the hexagonal unit cells stacked above it. This is illustrated in Figure 5-5.

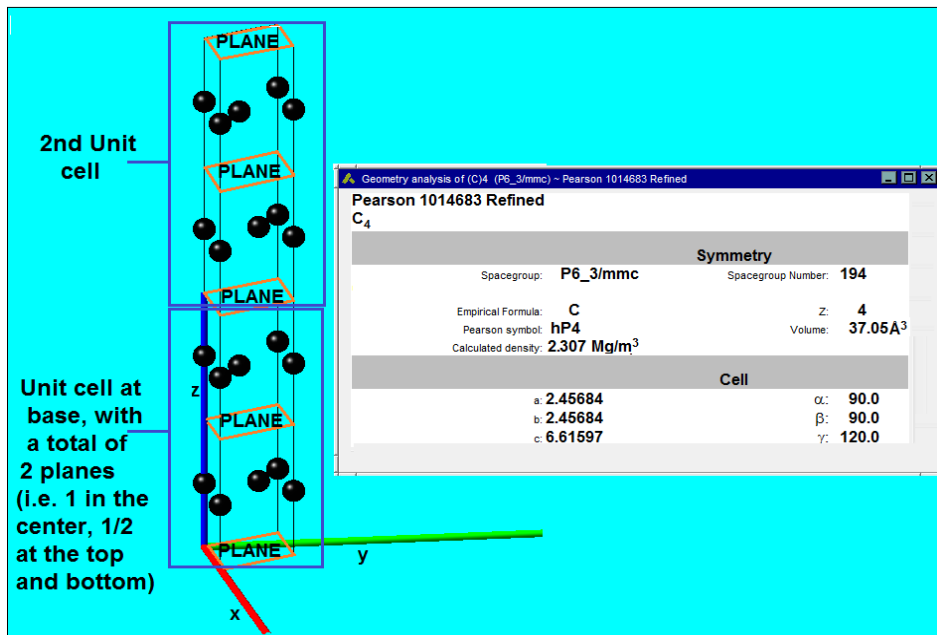


Figure 5-5: Two hexagonal unit cells, stacked vertically on top of one another

Thus, it follows that the number of planes, n_p , present within a single crystal (containing hexagonal unit cells) is calculated by

$$\begin{aligned}
 n_p &= 2 + 2(n_v - 1) \\
 &= 2 + 2(35 - 1) \\
 &= 70 \text{ planes}
 \end{aligned}
 \tag{15}$$

The resulting planar surface area (for all planes), **PSA**, is calculated as

$$\begin{aligned}
 PSA &= \frac{PSA_T}{n_p} \\
 &= \frac{13\,678.09}{70} \\
 &= 195.401 \text{ \AA}^2
 \end{aligned}
 \tag{16}$$

The calculated **crystallite (PSA_T)** and **planar (PSA)** surface areas for all four samples are shown in Table 5-9.

Table 5-9: Calculated crystallite surface areas for the four graphite powder samples

Sample name	$V_u(\text{\AA}^3)$	$V_c(\text{\AA}^3)$	n_p (#)	$PSA_T (\text{\AA}^2)$	$PSA (\text{\AA}^2)$
US Nano 1058	35.656	11 460 441	70	33 893	484
Mk Nano CG-050	35.617	8 008 809	62	27 594	445
Nano Amor 1250HT	35.649	9 158 708	64	32 925	514
NGG	35.488	11 800 662	70	13 678	195

From the data generated before and presented in Table 5-9 it is clear that the NGG sample is the most crystalline material of all the samples, indicated by its more defined diffraction peaks and the larger number of crystallographic planes. The use of the NGG sample will also allow for the smallest possible representative computational model (in comparison to the other samples), due to its low planar surface area. The other three samples exhibit a slightly lower degree of crystallinity. The XRD analysis performed, in combination with Rietveld refinement, was used to determine the crystallite size and the unit cell lattice parameters of each graphite powder sample.

Corresponding crystallite and BET (measured) surface areas

By using the data obtained from the MBET analysis of all four graphite powder samples in conjunction with data obtained from the PXRD analysis of the same samples, the surface area of each crystal and corresponding graphene planes for each of the graphite powder samples was

calculated. These calculated results may be used in determining the appropriate *minimum size* of a computational model (using the same configuration and definitions that were used to formulate equation 15) of the graphite surface, which must have a planar area close to (or greater than) that of the planar surfaces of the graphite samples' crystallites (i.e. *PSA*).

Bragg's Law was used to determine the distance between the two-dimensional graphene sheets. It was found that this inter-planar distance, d , ranged from 3.347 Angstrom to 3.357 Angstrom.

Hence, when considering the information above, the crystallographic structure of each of the four graphite powder samples is known with an adequate level of accuracy and as a result may now be accurately modelled using the VASP 5.3 and LAMMPS software. However, due to its higher level of crystallinity, the nuclear grade graphite sample was selected as the most appropriate sample to be used throughout the modelling process and for any further experimentation (such as TGA, DSC and LFA).

5.3. FOURIER TRANSFORM INFRARED (FTIR) AND RAMAN VIBRATIONAL SPECTRA CHARACTERISATION

Below are the FTIR (transmittance) patterns of all four of the graphite powder samples, with the background pattern already subtracted:

- a) The SGL Group, US Research Nanomaterials Inc. (US Nano)
- b) mk NANO Incorporated (mk Nano)
- c) Nanostructured and Amorphous Materials Inc. (Nano Amor)
- d) Nuclear grade graphite (NGG)

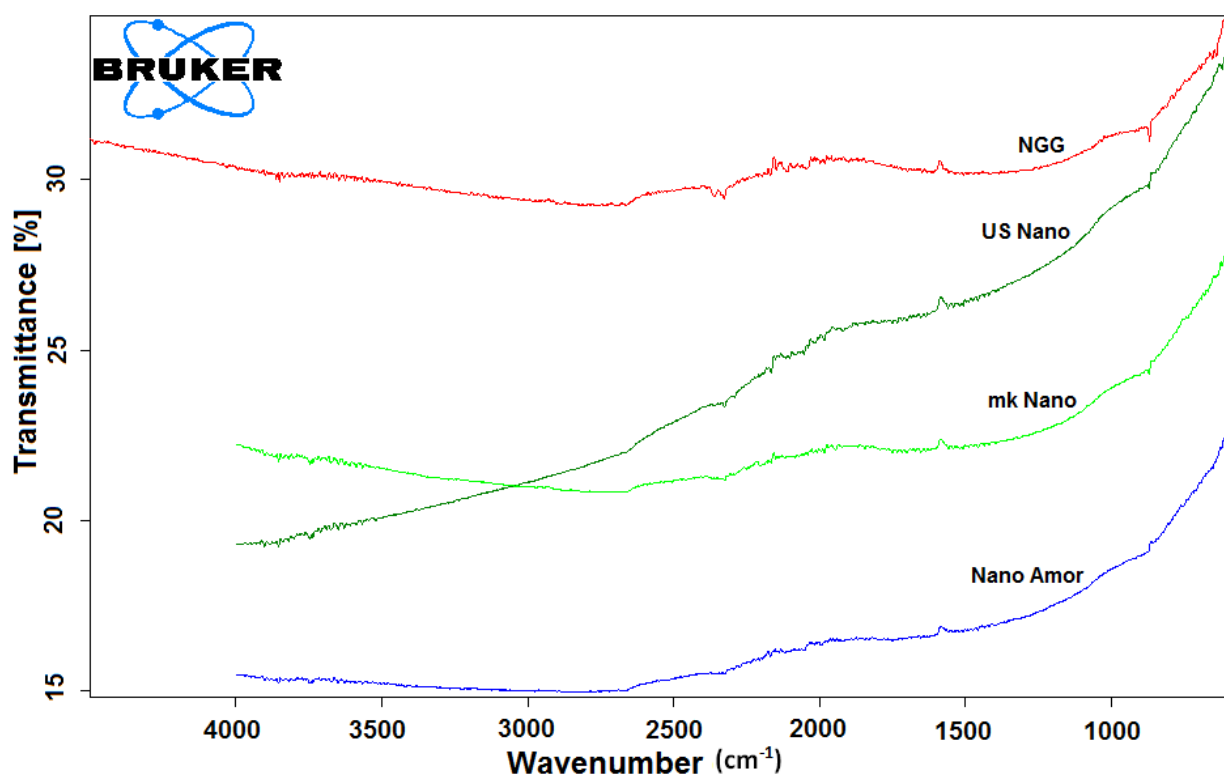


Figure 5-6: FTIR patterns of the four graphite powders supplied by (i)US Research Nanomaterials Inc. (ii)mkNANO Inc. (iii)Nanostructured & Amorphous Materials Inc. and (iv)PBMR SA

From Figure 5-6, the difference in the shape of the transmittance patterns between the diamond cell (i.e. background) and each of the graphite powder samples (when neglecting the presence of the peak at approximately 1600 cm^{-1} -- attributed to the presence of carboxyl functional groups ²³), is insignificant, with no high intensity infrared peaks being detected for any of the samples. These results are expected as graphite is known to absorb most of the incident infrared radiation and are in agreement with those of work done by Friedel and Carlson (1972) ²⁴. The difference in the slope of each of the sample patterns may simply be attributed to the fact that each of the samples are of a different particle size.

Figure 5-7 shows the Raman patterns of the four graphite powders (listed previously).

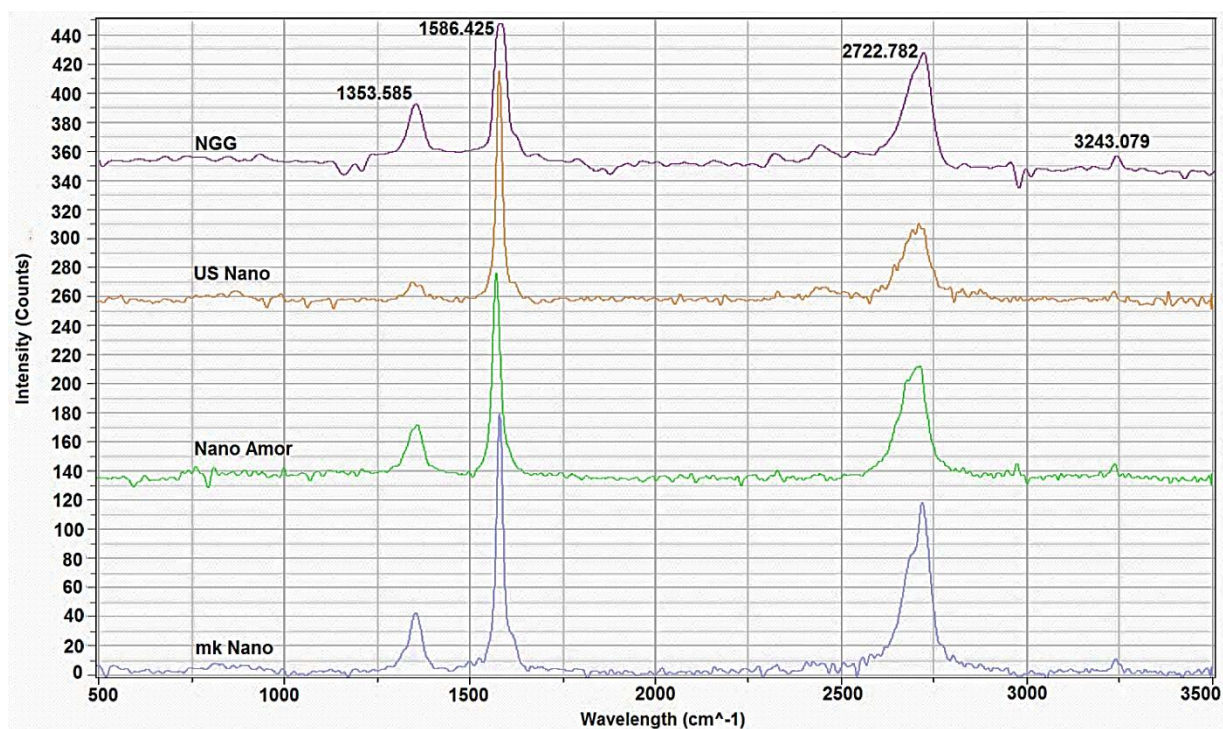


Figure 5-7: Raman patterns of the four graphite powders supplied by the PBMR SA, US Research Nanomaterials Inc., mK NANO and Nanostructured and Amorphous Materials Inc

Table 5-10: Raman frequency lists for each of the graphite powder samples

Sample	Raman frequency list (cm^{-1})
NGG	1353.6 ; 1586.4 ; 2722.8 ; 3243.1
US Nano	1346.0 ; 1578.7 ; 2708.9 ; 3235.9
Nano Amor	1358.0 ; 1570.0 ; 2712.38 ; 3231.3
Mk Nano	1353.4 ; 1579.6 ; 2718.3 ; 3241.0

By comparing the Raman patterns produced by each of the four graphite powders in Figure 5-7, it is observed that they are consistent with the Raman patterns of other graphite powders published in literature ^{7,25}.

5.4.THERMO-GRAVIMETRIC ANALYSIS (TGA)

As discussed in the last paragraph of section 5.2, the nuclear grade graphite (NGG) was selected as the most appropriate graphite sample to be used for further experimental work. Table 5-11 gives a description of the composition of the various (water and graphite-water) samples that were prepared and the instrumental program applied to each of the experimental runs.

Table 5-11: Sample compositions and instrumental parameters used in the TGA analysis

#	Mass NGG (%)	Total mass (mg)	Instrumental program			
			T_i , °C	T_f , °C	Time, minutes	ΔT
1	0 (100% water)	66.312	Ambient	150	125	1 °C.min ⁻¹
2	0 (100% water)	50.2		150	65	2 °C.min ⁻¹
3	5.555	72.9		200	180	1 °C.min ⁻¹
4	5.708	45.9		200	90	2 °C.min ⁻¹
5	28.227	58.1		133	110	1 °C.min ⁻¹
6	34.37	49.52		150	65	2 °C.min ⁻¹
7	0 (100% water)	46.76		40	300	1 x step increase
8	0 (100% water)	46.5		60	35	1 x step increase
9	25.463	56.16		50	200	2 °C.min ⁻¹
10	26.919	52.75		40	300	1 x step increase
11	28.168	58.72		40	73	2 °C.min ⁻¹
12	28.962	55.9		40	120	1 °C.min ⁻¹

When analysing the TGA results (Figure 5-8 and Figure 5-9), it is observed that (when considering the curves for the water samples only), the presence of the graphite powder within the graphite-water sample clearly delays the expulsion of water from the sample. This can be seen when considering the position of the points indicated on the two figures, which shows (in the case of graphite-water mixtures) when the trend of the curve deviates from that of the demineralised water TGA curve. These points may also indicate the final point of release of bulk water and the onset of the release of water from (or in close proximity to) graphite particle surfaces and of water that lies within the intercalated graphite spaces. The protrusions observed at the start of the analyses of sample numbers 1, 7, 8 and 10 are a result of the platinum crucible being inserted into the heating chamber while the crucible is still cooling down to the temperature of the surrounding environment.

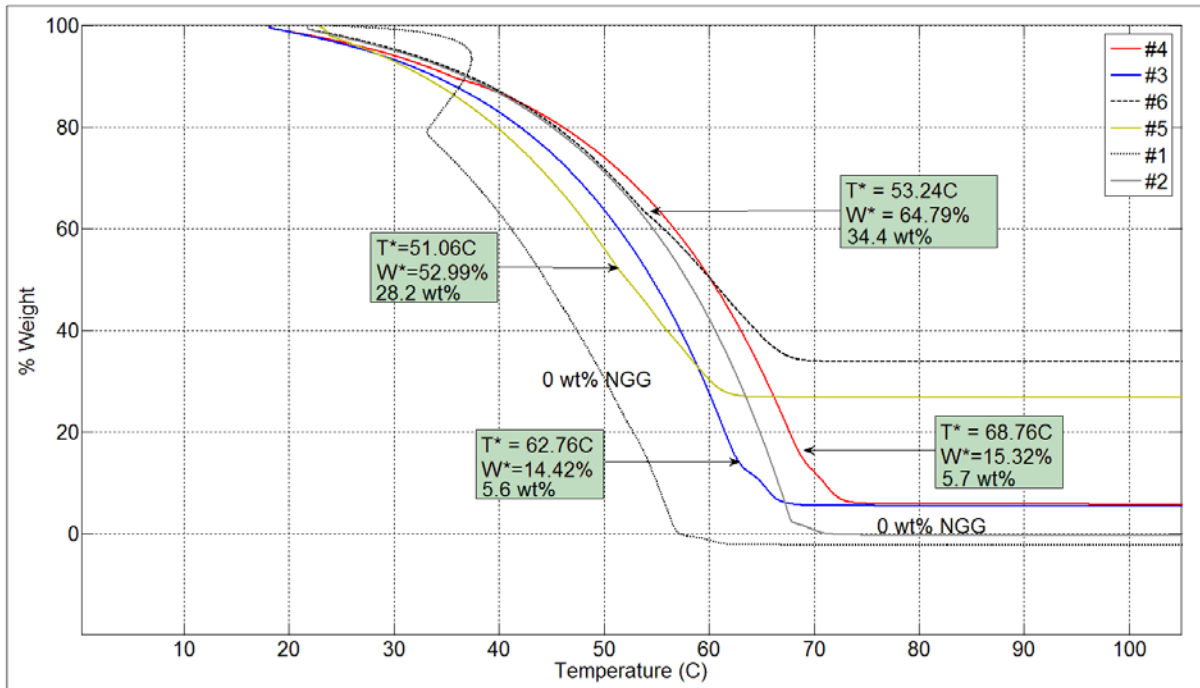


Figure 5-8: Results of TGA analysis for samples 1 through to 6. NGG concentrations are also indicated (by weight percentage). T* and W* indicates the final point of release of bulk water.

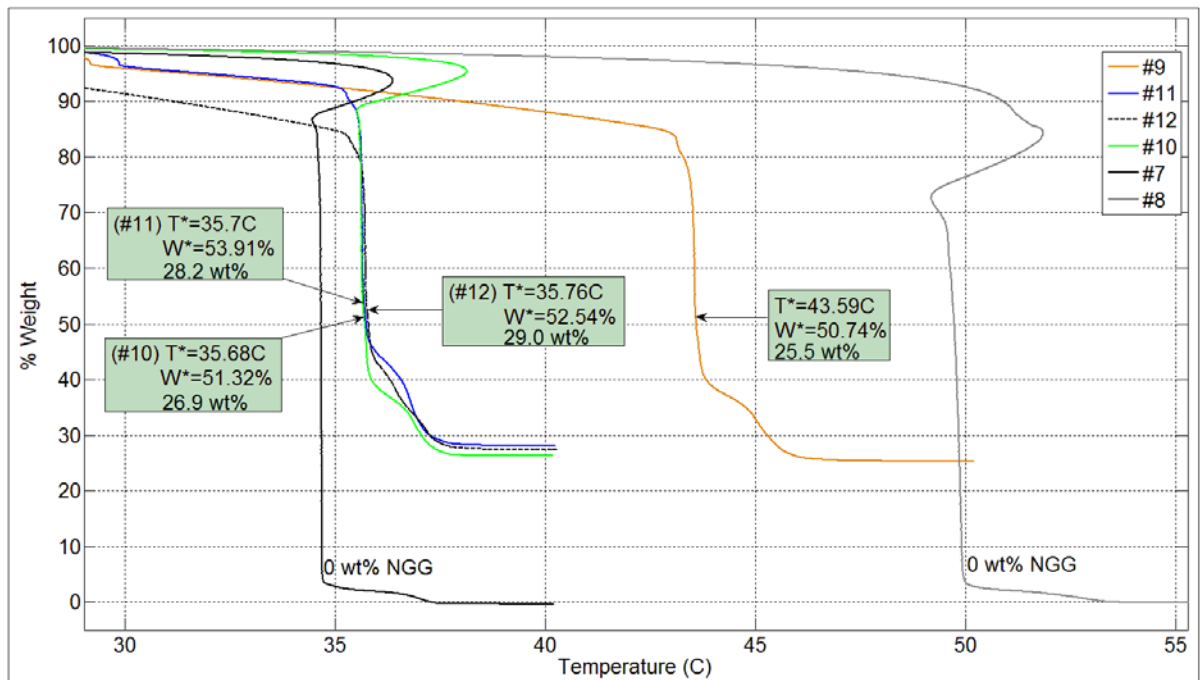


Figure 5-9: Results of TGA analysis of samples 7 through to 12. NGG concentrations are also indicated (by weight percentage). T* and W* indicates the final point of release of bulk water.

The positions of W*, relative to the point at which no further mass loss is observed, were then compared to the mass fraction of graphite powder present within each of the graphite-water mixtures, the results of which are illustrated in Figure 5-10 below. The positions of these points

were confirmed by means of differential thermo-gravimetric analysis (DTGA). (Refer to Annexure B)

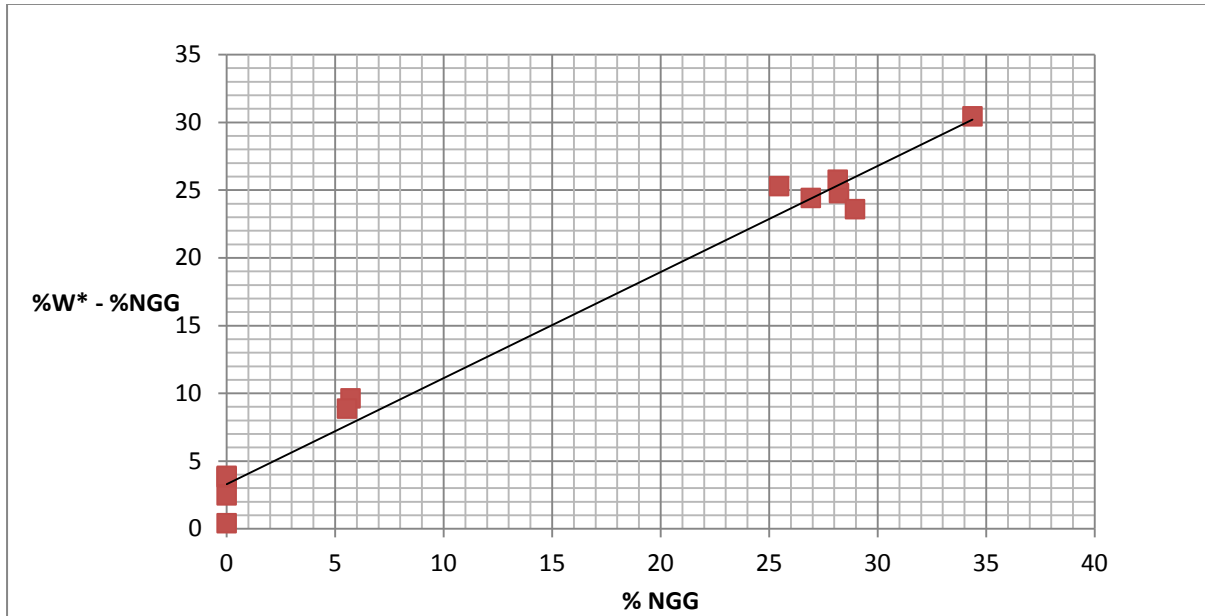


Figure 5-10: Graph indicating the relationship between the fraction of graphite present within the graphite-water mixture and the point at which the expulsion of water (indicated by W^* in Figure 5-9) from the mixture is delayed

Furthermore, from this data, one can determine how much water (per milligram of NGG and referred to as the specific wetting value – or mass fraction, given symbol “ ζ ”) is required to prepare samples of only “surface wetted” graphite.

Table 5-12: Processed data indicating how much demineralised water, per milligram of NGG, is required in order to prepare samples of only “surface wetted” graphite and its dependence on temperature.

Sample #	Mass of NGG in sample (mg)	Total sample mass (mg)	T^* (C)	W^* (%)	Total sample mass at W^* (mg)	Mass of water at T^* (mg)	$\zeta \left(\frac{mg H_2O}{mg NGG} \right)$
3	4.050	72.9	62.76	14.42	10.512	6.462	1.596
4	2.620	45.9	68.76	15.32	7.032	4.412	1.684
5	16.400	58.1	51.06	52.99	30.787	14.387	0.877
6	17.020	49.52	53.24	64.79	32.084	15.064	0.885
9	14.300	56.16	43.59	50.74	28.496	14.196	0.993
10	14.200	52.75	35.68	51.32	27.071	12.871	0.906
11	16.540	58.72	35.7	53.91	31.656	15.116	0.914
12	16.190	55.9	35.76	52.54	29.370	13.180	0.814

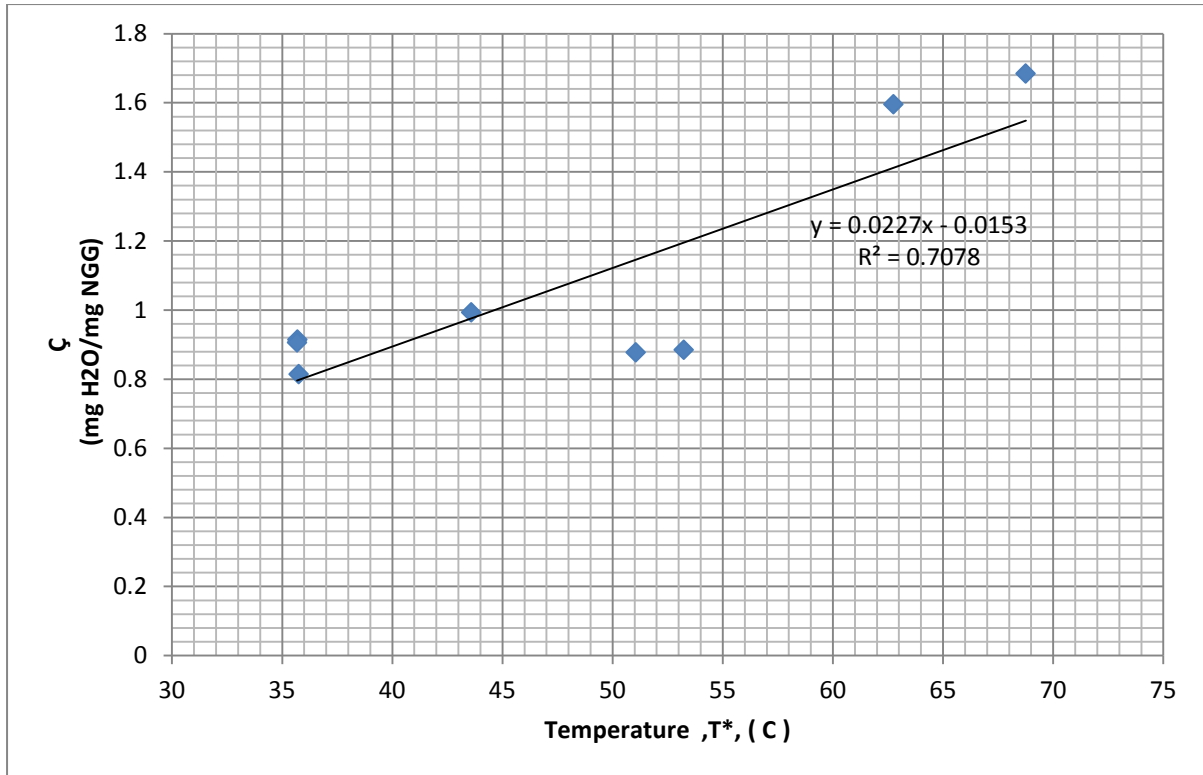


Figure 5-11: Relationship between Ç (mass ratio) and T*

Based upon the evidence above, one may conclude that the interfacial water molecules present on the graphite particle surfaces and graphite inter-/intra-particle spaces may very well be adsorbed on the surface and behave differently (and require more energy to be liberated) than the bulk water molecules. Furthermore, the amount of water required to adequately “wet” the surfaces of the graphite particles is related to the temperature of the graphite-water mixture.

5.5. DIFFERENTIAL SCANNING CALORIMETRY (DSC)

A DSC analysis was carried out in order to determine the heat capacitance values of various dry and “wetted” graphite samples, prepared using NGG. This was done to not only elucidate the effect the presence of water intercalated on graphite surfaces has on thermo-physical properties, but also for comparison with heat capacitance measurements performed at a later stage, using a laser flash analysis (Annexure C). The sample compositions prepared (according to the specific wetting values determined by TGA) and then analysed using DSC are described in Table 5-13, along with the temperature range applied to the instrumental program.

Table 5-13: Prepared sample compositions (containing de-ionised water and nuclear grade graphite) and instrumental parameters used in DSC. It must be noted that only a fraction of each of the (wet) samples listed below was used

#	Mass NGG (mg)	ζ (mg H ₂ O/mg NGG)	Initial temperature, T_i (°C)	Final temperature, T_f (°C) ^k
1	106	0 (clean graphite)	25	75
2	832	0.67	26	36
3	516	0.89	36	46
4	266	1.12	46	56
5	1163	1.34	55	65
6	1274	1.58	65	75

The basic principle employed in a TGA is also employed in a DSC, where the heat flow into the sample (at constant pressure) is measured over a period of time. By integration, the total amount of thermal energy (ΔQ) transferred to (or from) the sample for a specific thermal event taking place between two points in time (t_1 and t_2) is determined.

$$\Delta Q = \int_{t_1}^{t_2} \left(\frac{dQ}{dt} \right)_{\text{sample}} dt \text{ Joules} \quad (17)$$

The specific (isobaric) heat capacity is then determined by dividing the total amount of thermal energy (expressed in Joules) transferred by the change in the sample temperature (ΔT), over the specified time period (expressed in seconds, from t_1 to t_2), multiplied by the sample mass (m) expressed in grams.

$$C_p = \Delta Q / (m \times \Delta T) \quad (18)$$

A second, more direct method to obtaining the heat capacitance (using the same symbolic meaning as above), as a direct function of temperature is the following:

$$C_p = dQ / m \cdot dT \quad (19)$$

^k The smallest temperature range possible was used as an increase in pressure results in a deviation from the isobaric assumption.

This formula may also be expressed as a product of the heat flow rate (expressed in Watts) and the inverse of the heating rate utilised, expressed in degrees Celsius per second.

$$\frac{dQ(T)}{dT} = \frac{dQ}{dt} \times \frac{dt}{dT} \quad (20)$$

$$= \text{Heat Flow} \times \frac{1}{\text{Heating Rate}}$$

The result of the DSC analysis done for sapphire, required for the calculation of the instrumental correction factor, is shown below.

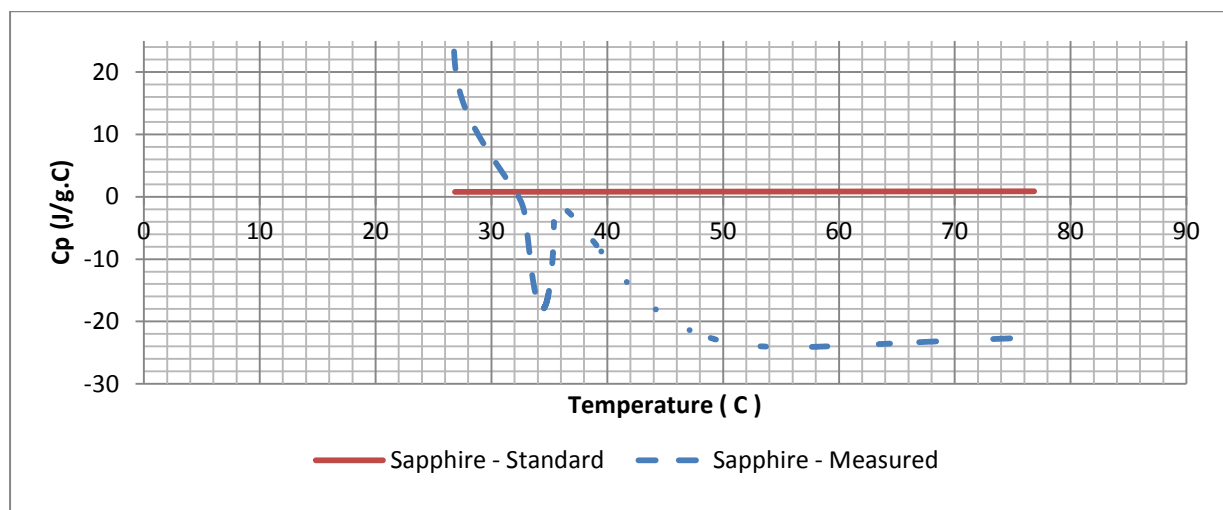


Figure 5-12: Calculated heat capacitance values of sapphire from DSC analysis, with referenced heat capacitance values indicated (red)

The referenced heat capacitance values of sapphire (which were consistently close to approximately 0.8 J/g.C)²⁶ were superimposed with those of the measured heat capacitance values of sapphire. Figure 5-12 indicates that, during DSC analysis, thermal equilibration of the sapphire sample is only reached after approximately 36°C. Measurements made at temperatures close to the surrounding ambient temperature may not easily reach thermal equilibration. Thus, when determining the appropriate correction factor to apply when calculating the heat capacitance of other samples (such as clean and wet graphite powder), one is only able to do so (reliably) for temperatures greater than 50°C. Despite this, the heat capacitance data produced for clean and wet graphite for a temperature range of 25°C to 75°C is still shown in Figure 5-13.

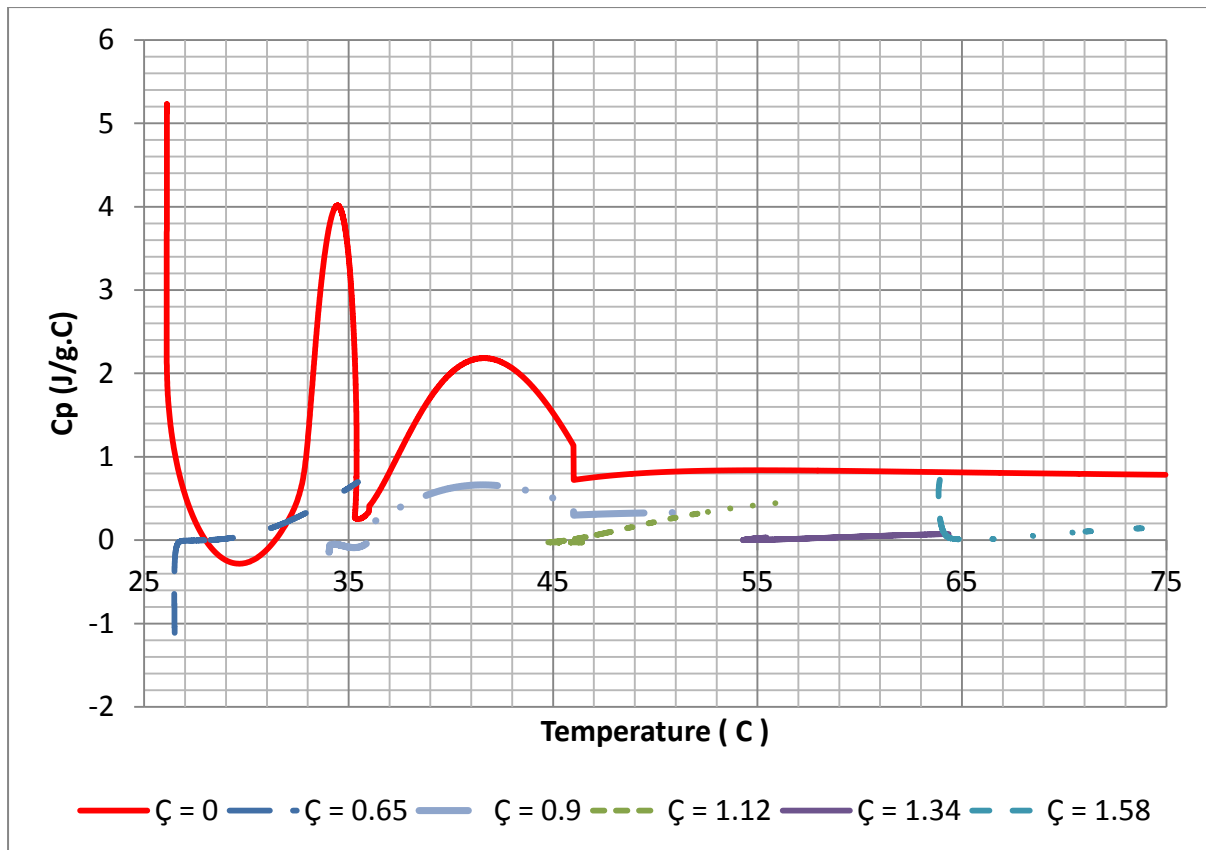


Figure 5-13: Calculated heat capacitance values for clean and wet NGG samples of various specific wetting values (ζ)

Table 5-14: Calculated specific (isobaric) heat capacities for "wetted" graphite samples, containing various concentrations of de-ionised water (with an average heat capacitance of approximately 4.18 J/g.K)

#	Mass NGG (mg)	ζ ($\frac{mgH_2O}{mg\ NGG}$)	$T_{average}$ ($^{\circ}C$)	C_p (J/g.K)
1	106	0 (clean graphite)	52.5	0.83
2	832	0.67	30	0.10
3	516	0.89	41	0.65
4	266	1.12	51	0.26
5	1163	1.34	60	0.04
6	1274	1.58	70	0.08

When considering published figures, the specific, isobaric, heat capacity (C_p) of bulk graphite powder has been shown to lie between 0.7 and 1.6 J/g.K, with weak linear temperature dependence up to 630 K ^{27,28}. When considering the DSC analysis results of pure nuclear grade graphite used in this study, a specific (isobaric) heat capacitance of approximately 0.8 J/g.K is observed, which is in good agreement with published values.

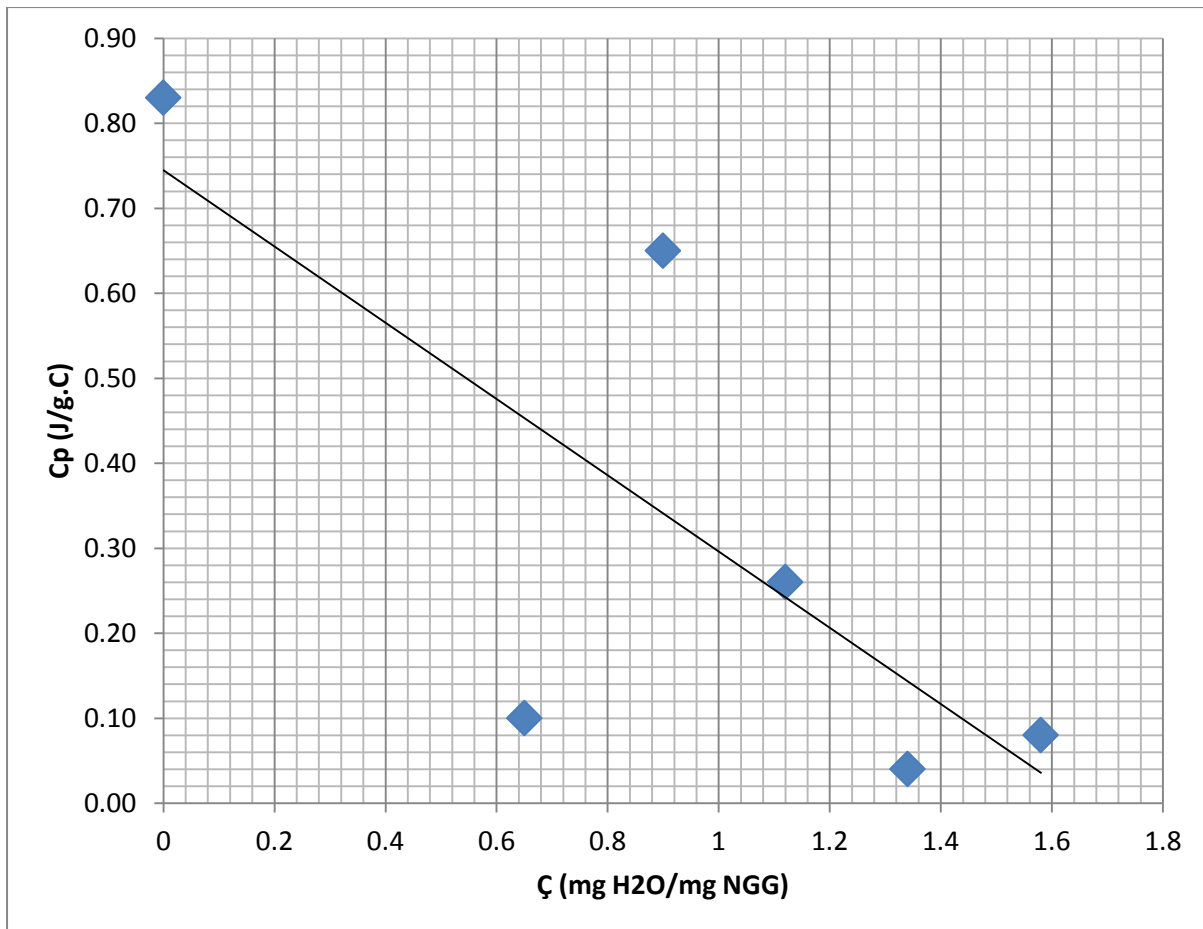


Figure 5-14: Heat capacitance values measured/calculated for dry and wet samples of NGG

NOTE: Scatter and degree of reproducibility

The degree to which the graphite particles remained “wetted” throughout each of the DSC experiments may not remain constant, as some of the graphite particles may conglomerate and separate from the water molecules, specifically for samples utilising large quantities of water. A much larger number of (DSC) data points would be required in order to confirm the reproducibility of the above results. However, due to the multitude of experiments that were required to fulfil the requirements of this thesis, it was not possible to focus intensely on any single experiment performed in this thesis. One can deduce that, based on the limited data produced in the DSC analysis, performing such an analysis on “wetted” graphite samples at furnace temperatures close to the ambient temperature makes it difficult for reliable data to be produced and may contribute to measurement error.

When making a comparison between the calculated heat capacities of the dry and wet NGG samples (using the average temperature-heat capacitance values), the dry samples have a larger heat capacitance. The wet graphite particles with large specific wetting values have a heat

capacitance an order of magnitude smaller than that of the dry graphite. This could imply that the presence of water intercalated on the surfaces of the graphite particles act as “heat sinks”, delaying the expulsion of thermal energy from the graphite particles.

6. COMPUTATIONAL MODELLING

The computational strategy followed was to equate the experimentally observed surface area (from BET) with the effective amount of water adsorbed on the graphite surface (from TGA) to define a graphite model size (with appropriate degrees of freedom) and group symmetry appointed, which can be used to calculate thermal conductivity.

Representation of the graphite surface

The first stage of the modelling process involved the selection of the appropriate hexagonal and rhombohedral unit cell, based on the powder XRD data produced by the NGG sample and its subsequent library matches, also derived from the Medea databases (*ICSD* and *Pearson*). For the purpose of modelling and specifically extended supercell environments (always opened then to space group P1), either the graphite structure at space group 186 or 194 can be used, since this transformation reflects a shift in the C-axis coordinate system, which will not alter the chemical nature and inter-planar d-spacing. But in the sense of crystallographic application such as TOPAS power diffraction refinement, the exact space group environment is crucial and determines the abundance of respective diffraction amplitudes at specific reflections and as result dictates the respective scaling applied when multi-phases are present during a Rietveld analysis. In the case of space group 166 a hexagonal setting R-3m:H or rhombohedral setting R-3m:R applies which also can be inter-related by a transformation along the C-axis, but again is determining the abundance of reflection amplitudes during a pXRD pattern analysis.

A structural refinement of the respective graphite unit cells (at full space group symmetry of: $P6_3/mmc$ and R-3m) was then undertaken using the VASP 5.3 software applying density functional theory (DFT). This was followed by the determination of the appropriate model size to be used to replicate the surface of a single graphite crystal – (as determined from XRD-Rietveld). Once the (in-plane) dimensions of the model were determined, VASP 5.3 and DFT were used once again to minimise the supercell structure (now at relaxed P1 Space Group symmetry) to ensure that the model created, equates to that of a chemically stable surface (based on the rule that the original single crystal unit cell and space group should again be deduced from this *large relaxed supercell – P1 symmetry – refinement*).

The partial atomic charges (NET charges) of each of the carbon atoms within the graphite surface models were then determined using the MOPAC code available within the MedeA software suite – calculated through a single point analysis.

Bulk water representation

At the same time, a single point energy analysis involving a specific number of water molecules (determined using the specific wetting values calculated from TGA) using MOPAC (PM7 Functional) was performed, in order to determine the partial atomic charge of each of the atoms within this bulk water model and create a realistic representation of bulk water. It was noted that the final water model should not display a significant dipole moment.

Thermal conductivity

Finally, the LAMMPS software module was used to determine the thermal conductivity properties of the “wetted” and “dry” graphite models, the results of which were correlated to those of previous publications. In future publications, these results will be correlated to experimental results, produced using a laser flash analysis (LFA).

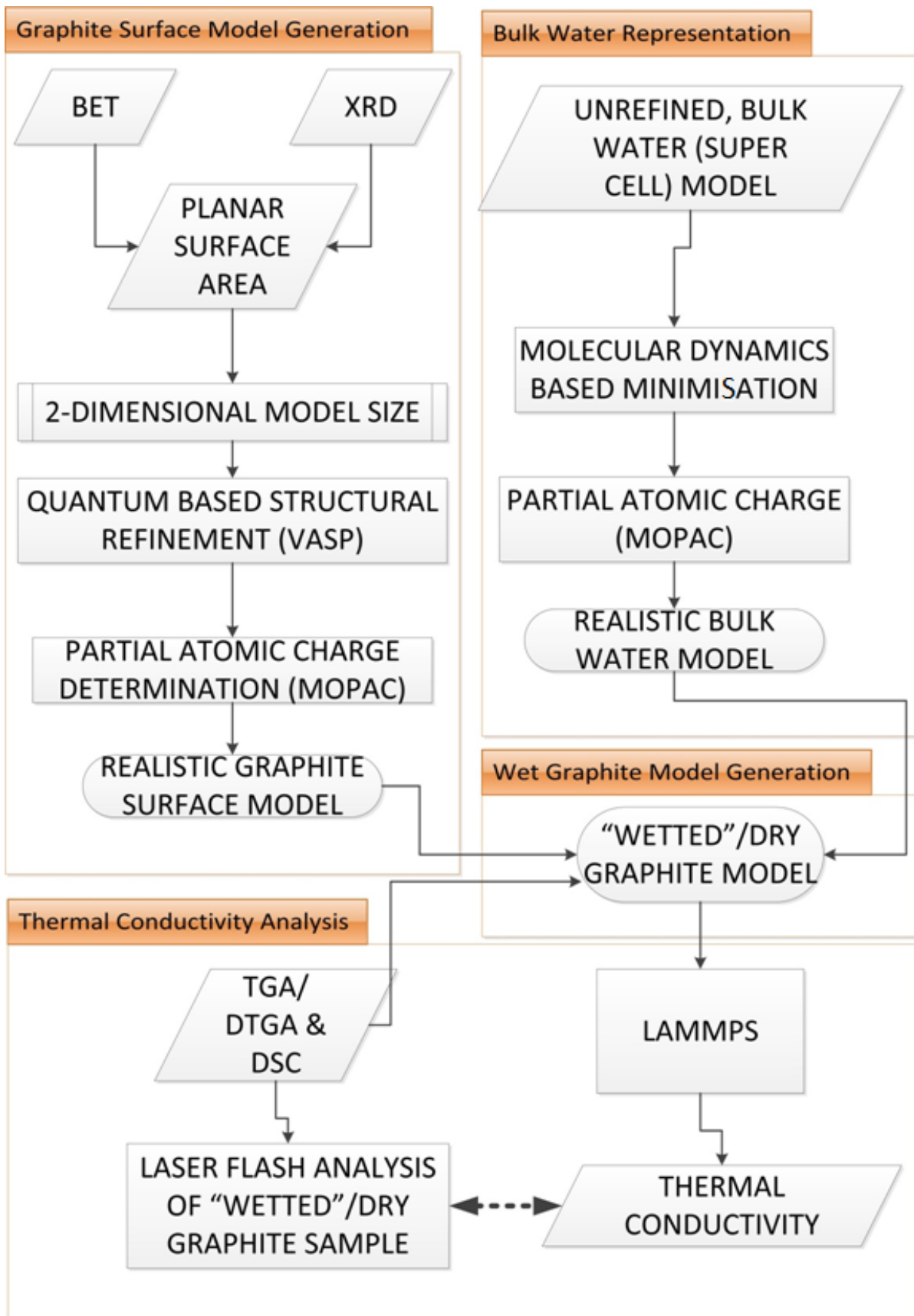


Figure 6-1: Methodology followed in the modelling process

6.1 GRAPHITE CRYSTAL SURFACE

6.1.1 STRUCTURE SELECTION

Reported (published) crystallographic models of the hexagonal and rhombohedral unit cells are available within the structure databases (ICSD and Pearson). A match has been confirmed (from the XRD-Rietveld and PDF-database) corresponding to any one of these structures, with the hexagonal structure being the major phase present in the NGG-sample.

Table 6-1: Unit cells selected from the crystallographic databases provided by the Medea software suite

XRD library match reference	PDF 00-041-1487					PDF 01-075-2078				
Space group no.	194*					166				
Crystal class	Hexagonal					Rhombohedral				
Space group	P63/mmc					R-3m				
Lattice parameters	a (Å)	c (Å)	α	γ	Z	a (Å)	c (Å)	α	γ	Z
	2.470	6.724	90°	120°	4	2.456	10.041	90°	120°	6
Medea database match	Pearson #1014683					Pearson #1251853				
Space group no.	194					166				
Crystal class	Hexagonal					Rhombohedral				
Space group	P63/mmc					R-3m				
Lattice parameters	a (Å)	c (Å)	α	γ	Z	a (Å)	c (Å)	α	γ	Z
	2.463	6.714	90°	120°	4	2.461	10.061	90°	120°	6

*The hexagonal unit cell with space group number 194 was selected for use in the modelling of the graphite surface, as it represents the dominant phase in the NGG sample.

VASP 5.3 (DFT) and a GGA-PBE exchange correlation functional including the PBE/PBESol functional (for solids) were used to perform structural refinement of all graphite structures above. A bulk structure relaxation was performed, using reciprocal space and a plane wave cut-off of 400eV. Spacing of the k-points was set at 0.3Ångstrom⁻¹(Brillouin mesh 3, 3) using an odd Brillouin zone grid size with the origin shifted to Γ . A Gaussian integration scheme with a smearing width of 0.1eV was selected. Convergence of the self-consistent-field was set at 1.0e⁻⁰⁵ eV. The result of this minimisation is shown in Table 6-2.

Table 6-2: Result of structure optimisation simulation

Structure library	Pearson #1014683, P6₃/mmc (194), hexagonal					Pearson #1251853, R-3m (166), rhombohedral				
Library lattice parameters	a (Å)	c (Å)	α	γ	Z	a (Å)	c (Å)	α	γ	Z
	2.463	6.714	90°	120°	4	2.461	10.061	90°	120°	6
VASP PBE lattice parameters	2.463	6.791	90°	120°	4	2.463	10.262	90°	120°	6
VASP refined density	2.237Mg/m ³					2.220Mg/m ³				

6.1.2 MODEL SIZE

To determine the appropriate model size, the planar surface area (*PSA*) in combination with the Void Finder Tool provided by Medea, was utilised. This facility allows one to analyse a given crystal for accommodating space, by dividing the cell into Voronoi cells around each atom. A Voronoi cell is defined as the volume encapsulating every point (at defined extents, usually dictated by *v/d* Waals interactive distances) that is closer to the atom's centre than to all other surrounding atoms. The physical size of various atomic species is taken into consideration through a set of covalent radii ²⁹.

Initially two small graphite crystal models were constructed, with a unit cell repetition transformed as [2,0,0],[0,2,0],[0,0,1] since the planar surface area depends on the in-plane dimensions of the crystal surface. Next, the amount of empty space within each crystal was determined.

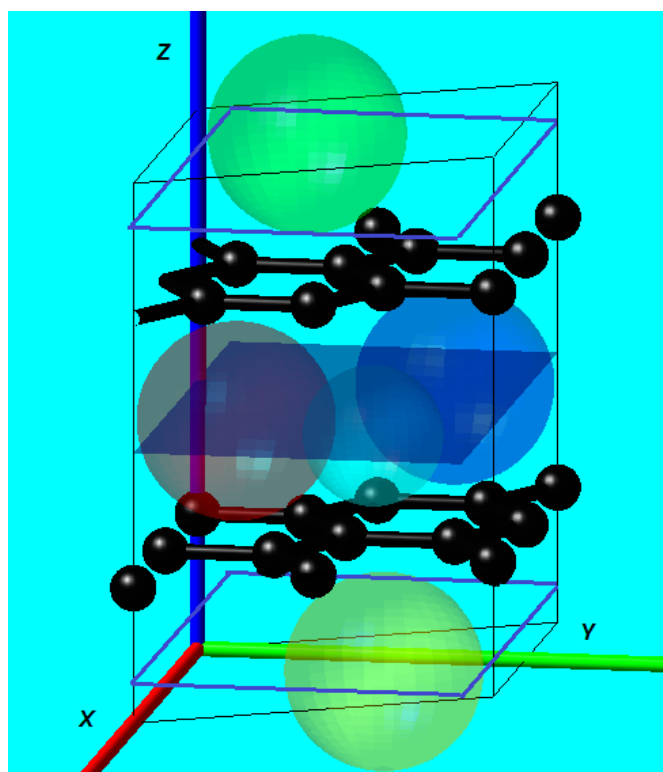


Figure 6-2: The majority of voids within the crystal are shown to pass through the centre of the planes defined when considering a 2x2x1 supercell built using the hexagonal unit cell

The planar surface area for the middle plane and a combination of the top and bottom planes provided by a crystallite of this size was calculated by determining the cross-sectional area of each of the voids associated with the planes. The average of the two calculated surface areas was then compared to the planer surface area obtained by the NGG sample (with $PSA \cong 200 \text{ \AA}^2$). This process was repeated, with an increase in the in-plane dimensions of each of the

(hexagonal and rhombohedral) based crystal models, until the void surface area calculated in *MedeA* came as close as possible to that of the planar surface area of the NGG sample.

The above process resulted in the selection of a custom graphite crystal for both the hexagonal and rhombohedral unit cells, transformed with lattice vectors $[7,0,0],[6,12,0],[0,0,1]$ which results in an orthogonal crystal space (confirmed by the *MedeA* software to reduce to the original full hexagonal and rhombohedral symmetry), with an average planar surface area of 217.8 and 268.9 Å², respectively, between the inner plane(s) and the consolidated top and bottom planes.

In order to quantify any finite size effects, other graphite models, with reduced in-plane dimensions, were created. To select other model sizes, the same principle (explained above) was applied. The reduced models allowed for a surface area greater than the required minimum planar surface area of approximately 200 Å². These models allowed for a sufficient number of atoms in each direction for effective thermal transport and a reduction in computational demand.

These (orthorhombic-shaped) graphite supercell models were minimised through the use of VASP5.3 (DFT), with the use of the GGA-PBEsol exchange correlation (and PBE) functional at P1 group symmetry and a plane wave cut-off of 400 eV. Spacing of the k-points was set at 0.3Ångstrom⁻¹, using an odd grid size and a Brillouin origin shifted to Γ . A Gaussian integration scheme with a smearing width of 0.1eV was selected. Convergence of the self-consistent-field was set at 1.0 e⁻⁰⁵ eV. The symmetry of these minimized structures produced by the VASP run were raised (reduced) to their original space groups and used to build extended supercell structures –extending the C-axis, to allow for greater connectivity between the carbon layers (seen in the context of heat conductance) when the structure is intercalated with water molecules. The model sizes utilised for the purposes of this thesis are shown in Table 6-3.

Table 6-3: Graphite model sizes utilised for computational modelling

Lattice vectors	Hexagonal space group			Rhombohedral space group		
	<i>a</i>	<i>b</i>	<i>c</i>	<i>a</i>	<i>b</i>	<i>c</i>
Models Size 1	[7,0,0]	[6,12,0]	[0,0,2]	[7,0,0]	[6,12,0]	[0,0,2]
Models Size 2	[5,0,0]	[3,6,0]	[0,0,4]	[5,0,0]	[3,6,0]	[0,0,3]
Models Size 3	[5,0,0]	[3,6,0]	[0,0,3]	[5,0,0]	[3,6,0]	[0,0,2]
Models Size 4	[5,0,0]	[3,6,0]	[0,0,2]	-	-	-

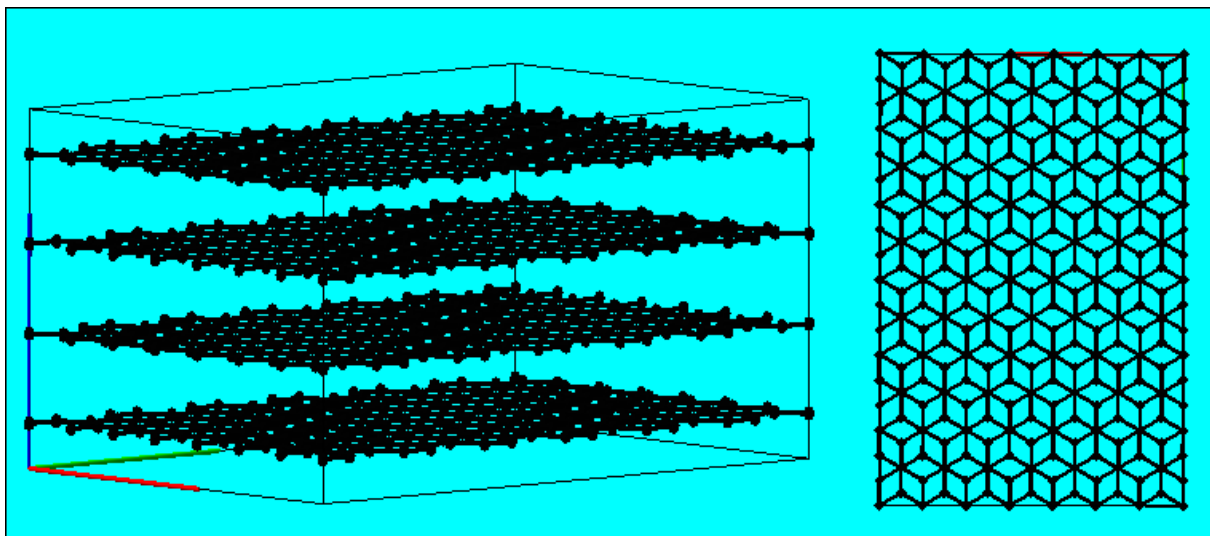


Figure 6-3: One of two final (orthorhombic shaped) graphite surface models, built using the hexagonal unit cell, extended to a super cell within MedeA

6.1.3 PARTIAL CHARGES

The two carbon atoms in the hexagonal unit cells are considered not to be equivalent and the partial charges for these carbons are calculated through a single-point calculation (using the restricted Hartree Fock scheme – for a closed electron shell system), using the MOPAC module within MedeA, (which solves the Schrodinger equation of an N-electron system by approximating the electronic wave function using the Slater determinant).

These partial charges would be used in the equilibrium molecular dynamics (EMD) simulation to predict thermal conductivity, applied to an orthorhombic shaped graphite supercell surface model. MOPAC (developed by Dr James J.P. Stewart, of Stewart Computational Chemistry) is a semi-empirical quantum code used for optimising the electronic structure of molecules and solids/surfaces. A flow chart technique shown in Figure 6-4 is used in MedeA for the convenient assignment of variable conditions, but also offers the flexibility to divide calculations into a sequence of stages, to be adjusted in subsequent refining of modelling conditions.

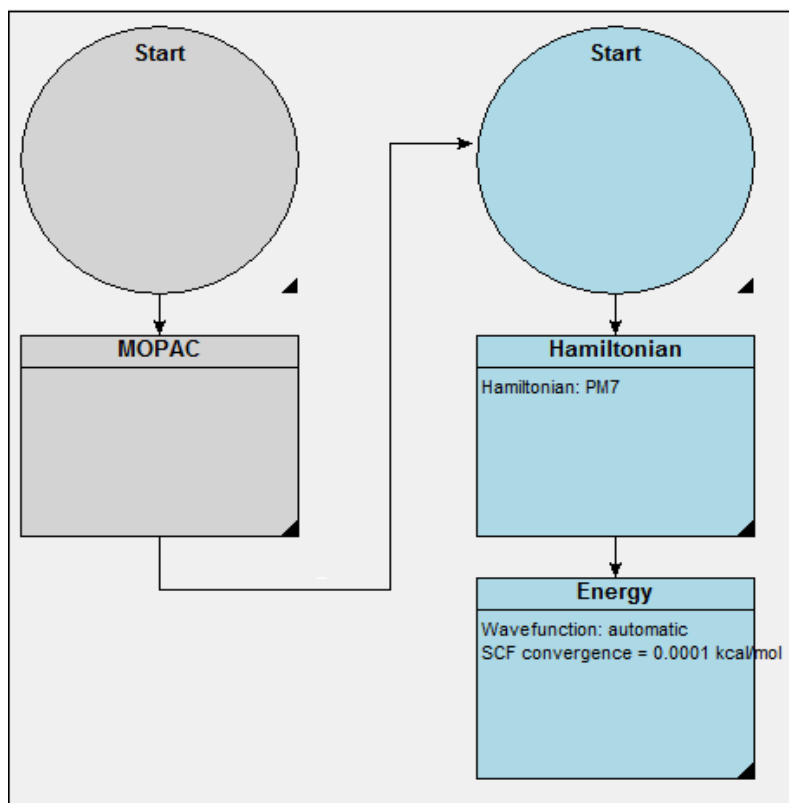


Figure 6-4: (MOPAC) Flow chart used to produce partial atomic charges.

The MOPAC-PM7 parameterisation was selected to produce the Hamiltonian. The atomic positions (as Cartesian co-ordinates) produced by the MOPAC.out file were converted to fractional positions in the orthogonal cell and raised (enhanced) in symmetry by the MedeA crystallographic interface, to offer the complete construction of a single unit cell -- a limitation in the MOPAC/MedeA interface software.

The SCF convergence scheme was selected automatically, with convergence being set at 0.0001 kcal/mol. It is important to note that, when utilising MOPAC within MedeA (specifically for a graphite structure such as the one in Figure 6-3), both the initial and finalised structures extracted and displayed by the MedeA environment are not directly related (with regards to atomic positioning) to the structure contained within the MOPAC.out file, which utilises a Cartesian atomic co-ordinate system.

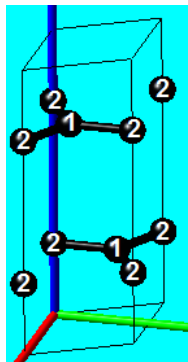
To determine which sum of atomic positions would result in the complete construction of a single unit cell when using the MOPAC module within MedeA, the atomic positions produced by the MOPAC.out file were visualised using a Cartesian co-ordinates system.

The co-ordinates of these atoms and their corresponding properties (such as their net partial charges) were extracted from the MOPAC.out file. Finally, by analysing the symmetry of the unit cell extracted, the unique atoms (derived by performing the appropriate symmetry operations,

could reproduce the entire unit cell) and their corresponding properties were selected. From this data it was observed that there existed a periodic distribution of charge within the hexagonal (194) based graphite surface model (Table 6-4); however, this was not the case with the rhombohedral based graphite surface model, in which the atomic partial charges (Table 6-5) were also calculated to be two orders of magnitude smaller than those of the hexagonal based surface model and all carbon atoms considered to be equivalent. Hence, the rhombohedral based surface model was considered as having a partial atomic charge of zero assigned to each of its carbon atoms.

This data (in combination with the application of a *pcff+* forcefield, appropriate for applications involving benzene-like ring structures ²⁹) was manually assigned to each of the atoms of the orthorhombic supercell graphite structures (used as the initial structure in the MOPAC run). The atom force field designation of type “cp” (for sp^2 hybridised carbon, which refers to the atomic bonding configuration) was assigned to each of the atoms. This allowed for a more realistic representation of the distribution of charge throughout the crystal structure.

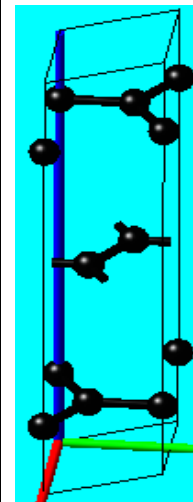
Table 6-4: (MOPAC) Calculated partial charges of carbon atoms comprising a single hexagonal unit cell within the orthorhombic - shaped supercell graphite surface (figures presented to four decimal places)

“Net atomic” charges and dipole distributions					“Mulliken” charges			Unit cell
Atom no.	Partial charge	No. of elec.	s-Pop	p-Pop	Atom no.	No. of elec.	Partial charge	
413	-0.0015	4.0015	1.0592	2.9423	413	4.0016	-0.0016	
415	0.0015	3.9985	1.0594	2.9391	415	3.9984	0.0016	
416	0.0016	3.9984	1.0594	2.9389	416	3.9982	0.0018	
422	-0.0016	4.0016	1.0592	2.9424	422	4.0018	-0.0018	
423	0.0015	3.9985	1.0594	2.9392	423	3.9984	0.0016	
424	0.0016	3.9984	1.0594	2.9390	424	3.9982	0.0018	
519	0.0015	3.9985	1.0594	2.9392	519	3.9984	0.0016	
520	0.0016	3.9984	1.0594	2.9390	520	3.9982	0.0018	
527	0.0015	3.9985	1.0594	2.9391	527	3.9984	0.0016	
528	0.0016	3.9984	1.0594	2.9390	528	3.9982	0.0018	

Atom numbers 413 and 422 correspond to one unique atomic position ($1/3, 2/3, 1/4$) at the crystallographic Wyckoff position **2c**, while the remaining atom numbers correspond to the second unique atomic position ($0, 0, 1/4$) with the Wyckoff position **2b**. A periodic repetition of the partial atomic charges tabulated above was observed throughout the hexagonal based surface model. Hence, by taking into account all the data produced by the MOPAC single point analysis of a supercell model to calculate the average net charge for each of the unique atomic positions, a net charge of -0.0015 e and +0.0015 e was assigned to each of the **2c** and **2b** atoms, respectively, within the (hexagonal-based) graphite surface model.

Table 6-5: (MOPAC) Calculated partial charges of carbon atoms comprising a single rhombohedral unit cell within the orthorhombic - shaped supercell graphite surface (figures presented to four decimal places)

"Net atomic" charges and dipole distributions					"Mulliken" charges			Unit cell
Atom no.	Partial charge	No. of elec.	s-Pop	p-Pop	Atom no.	No. of elec.	Partial charge	
30	0.0000	4	1.0593	2.9407	30	4.0000	0.0000	
31	-3.1E-05	4	1.0593	2.9407	31	4.0000	-0.0000	
32	0.0000	4	1.0593	2.9407	32	3.9999	0.0000	
33	-4.6E-05	4	1.0593	2.9407	33	4.0000	-3.6E-05	
34	0.0000	4	1.0593	2.9407	34	3.9999	0.0000	
35	-0.0000	4	1.0593	2.9407	35	4.0000	-6E-06	
36	0.0000	4	1.0593	2.9407	36	3.9999	0.0000	
37	0.0000	4	1.0593	2.9407	37	3.9999	0.0000	
38	-2E-05	4	1.0593	2.9407	38	4.0000	-6E-06	
39	-3.8E-04	4	1.0593	2.9407	39	4.0000	-1.9E-05	
40	0.0000	4	1.0593	2.9407	40	4.0000	0	
41	0.0000	4	1.0593	2.9407	41	4.0000	0	
42	-1E-05	4	1.0593	2.9407	42	4.0000	-2E-06	
43	-1.5E-05	4	1.0593	2.9407	43	4.0000	-1.8E-05	
44	-6E-06	4	1.0593	2.9407	44	3.9999	0.0000	



NOTE: Use of partial atomic charges in the thermodynamic calculations

- For the purposes of this thesis, only the Equilibrium Molecular Dynamics (EMD) approach utilising neutral models carrying no partial atomic charges were considered. Only van der Waals interactions were considered.
- The autocorrelation function utilised in the EMD software package of MedeA (v2.14) at the time did not take into account the Ewald summation of electrostatic interactions in the *pcff+* force field used to characterise the interatomic potentials. (Refer to Annexure D for a brief outline of the EMD approach)
- Models considering the partial atomic charges of each of the carbon, hydrogen and oxygen atoms were to be analysed (using both the EMD and NEMD approach) at a later stage and form part of a second publication. Simulations involving a larger number of "wetted" graphite models will also constitute a second publication.

6.2 BULK WATER

The required mass of water to be included into the graphite surface models (and the subsequent number of water molecules that would be needed to create the bulk water supercell) was calculated by multiplying the total mass of each of the orthorhombic supercell graphite surface models (using Avogadro's Law) by the specific wetting value, calculated earlier, as derived from TGA analysis. It was decided that a total of five bulk water models would be created, each of which corresponds to a specific temperature ("T*") and specific wetting value ("Ç") in Figure 5-11. The details of each of these models are shown in Table 6-6.

Table 6-6: Calculated size (using TGA data) of bulk water super cells required to represent graphite "wetted" surfaces

Temperature (T*)	°C	30	40	50	60	70
Specific wetting value(Ç)	mg H ₂ O/mg C	0.67	0.89	1.12	1.35	1.57
Total no. H ₂ O molecules	#	53	72	89	108	127
No. H ₂ O per plane (see Sect. 6.3)	#	26	36	44	54	64

A bulk water supercell was created, for each temperature presented in Table 6-6, using the molecular builder included in MedeA. The cell was then "cleaned" (which involves a preliminary minimisation process utilising molecular mechanics and a UNIVERSAL force field for organics) to achieve a local minima of the bulk water (as an initial estimate, optimised within the 3-D space permitted). A periodic copy of the supercell was created and its dimensions adjusted such that the lengths of the A- and B- axes were equal to that of the orthorhombic supercell graphite surface models and the length of the C-axis equal to 3 Angstrom (which is slightly less than the inter-planar distance between the carbon layers).

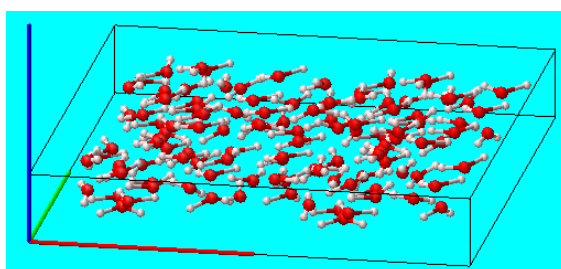


Figure 6-5: Average partial charges calculated for oxygen and hydrogen contained in a bulk water model, using MOPAC

MOPAC was then used (with the same parameters that were used in the charge determination of carbon atoms in the "dry" hexagonal graphite surface model) to determine the partial atomic charge of each of the atoms within the bulk water model. The average partial charges associated

with the oxygen and hydrogen atoms in bulk water, calculated by MOPAC, are given in Table 6-7.

Table 6-7: Average partial charges calculated for oxygen and hydrogen contained in a bulk water model, using MOPAC¹

Atom	Average net partial charge (e)	Average mulliken charge (e)
Oxygen	-0.751765	-0.813729
Hydrogen	0.375882	0.406864

By assigning the *pcff+* forcefield (with atom FF assignment types set as “o*” – [or oh’] for oxygen and “hw” for hydrogen) to the supercell and by using the data produced by the MOPAC.out file, the partial charges were assigned to each of the oxygen and hydrogen atoms in the bulk water supercell. This became the representative model for a bulk water cell, to be placed on the boundaries of – and intercalated with – the “dry” graphite model.

6.3 “WETTED” GRAPHITE MODEL

To create the graphite-water model, the “merge” tool within the MedeA builder was utilised, with the graphite surface models acting as the host structure and the bulk water supercell (Figure 6-5) as the guest “molecule”. A number of bulk water supercells (Table 6-6) were added onto the top and bottom surfaces of the graphite model and in between each of the carbon layers. An equal number of water molecules were inserted on the horizontal plane lying in between each layer and on the top and bottom surfaces (the combination of which is also referred to as a single plane) throughout the entire modelling process. Once water cells were added into the graphite models, the resulting model was replicated along the C-axis, periodically.

¹ Using a (VASP minimised) bulk water model containing 14 H₂O molecules, MOPAC was used (with the same parameters that were used in the charge determination of carbon atoms in the hexagonal-based supercell graphite surface model) to determine the partial atomic charge of each of the atoms within the bulk water model.

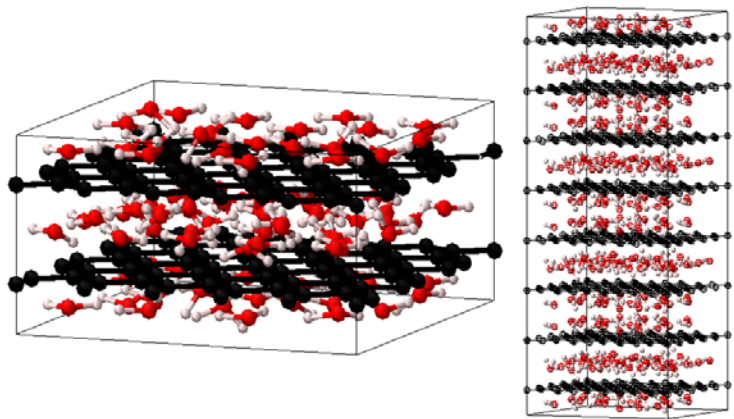


Figure 6-6: Hexagonal-based, “wetted” graphite surface models

6.4 THERMO-PHYSICAL ANALYSIS

The thermal conductivity module within MedeA was used to calculate the thermal conductivity of both “dry” and “wetted” graphite surface models, based on the hexagonal and rhombohedral unit cell.

A calculation process flow was constructed (shown in Figure 6-7), which consisted of a number of molecular dynamics (LAMMPS) analyses, with the PCFF+ force-field assigned, prior to the thermal conductivity calculation. The parameters used in each of the simulation stages are also shown.

The EMD (Green-Kubo) and (at a later stage) the NEMD approach were considered to calculate the thermal conductivity of the (dry and wet) graphite models. However, the NEMD method (unavailable to the author at the time) is seen as the most appropriate method due to the fact that this approach is ^{30,31}:

- (i) applicable to all systems;
- (ii) capable of handling non-homogeneous structures, such as those intercalated with water; and
- (iii) capable of dealing with systems with and without electrostatic terms.

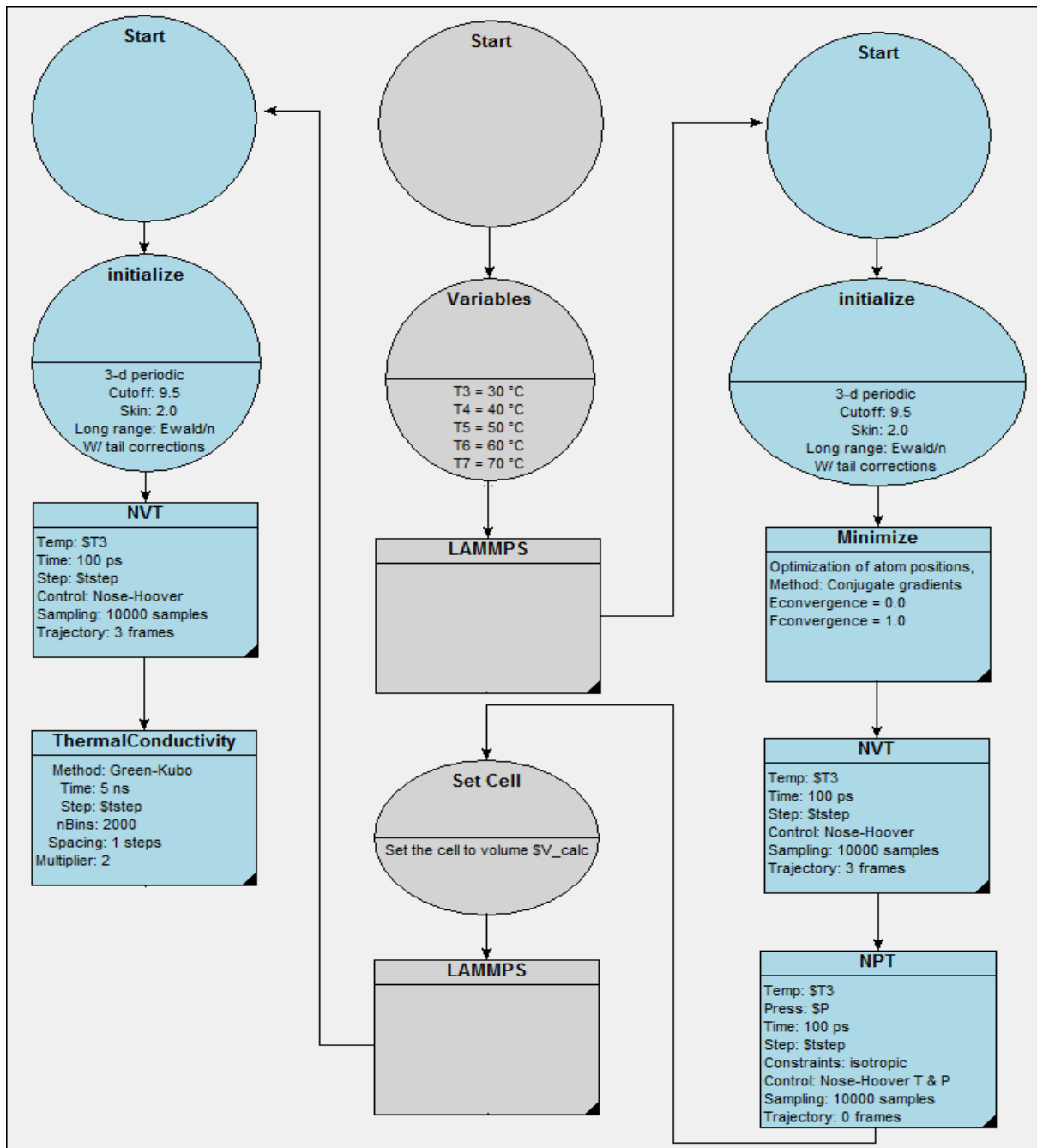


Figure 6-7: Flow chart used to determine the thermal conductivity of each “wetted” graphite surface

6.5 COMPUTATIONAL RESULTS AND INTERPRETATION

The graphs below illustrate some the results obtained for all thermal conductivity simulations, utilising the EMD (Green-Kubo) approach. For graphical representations of all the data produced, refer to Annexure A.

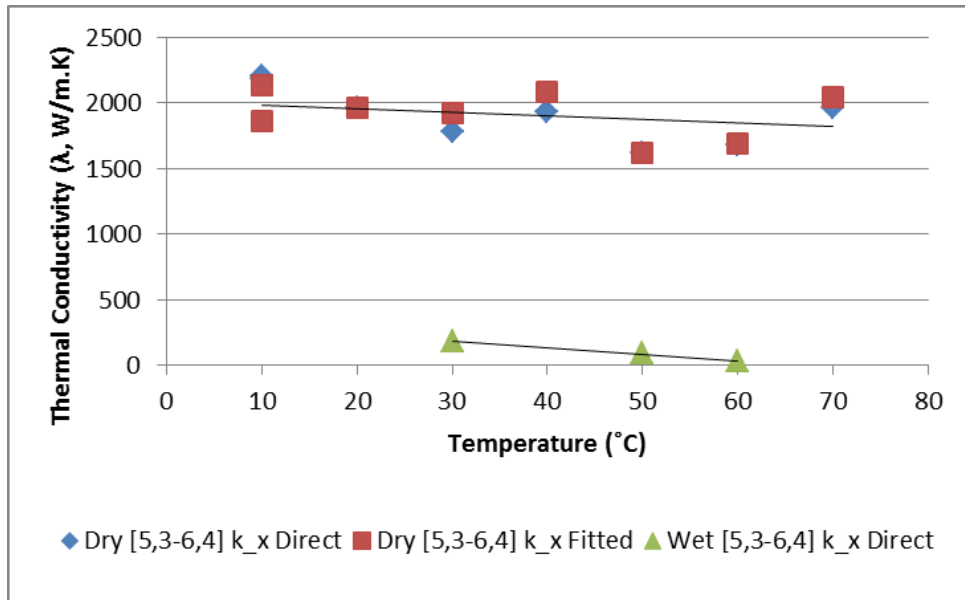


Figure 6-8: Thermal conductivity results obtained for the dry and wet, hexagonal (i.e. 194), graphite model with lattice vectors $a[5,0,0]$, $b[3,6,0]$ and $c[0,0,4]$. Only the direct integral values for intra-planar thermal conductivities along the “X-axis” are shown for the wet graphite models.

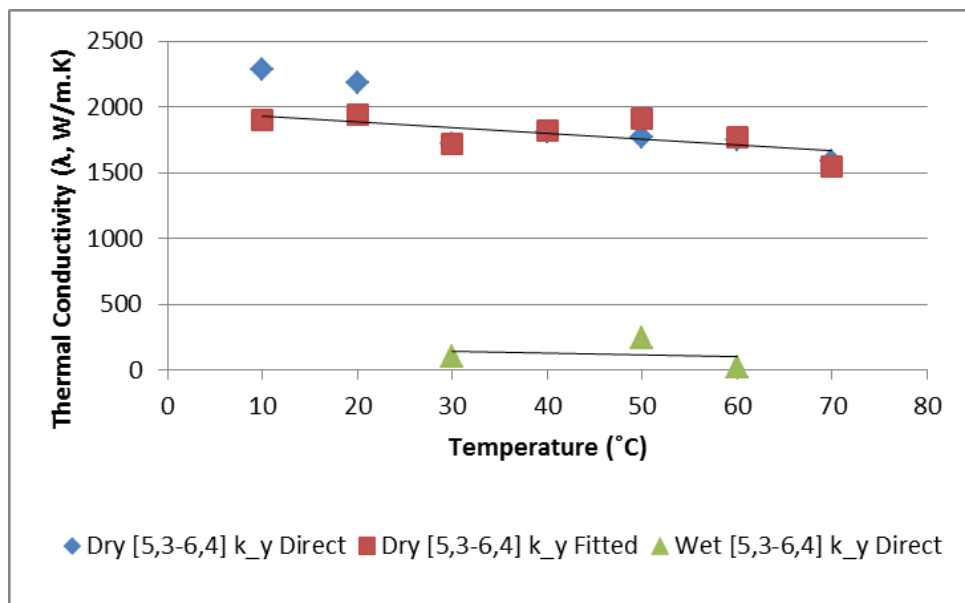


Figure 6-9: Thermal conductivity results obtained for the dry and wet, hexagonal (i.e. 194), graphite model with lattice vectors $a[5,0,0]$, $b[3,6,0]$ and $c[0,0,4]$. Only the direct integral values for intra-planar thermal conductivities along the “Y-axis” are shown for the wet graphite models.

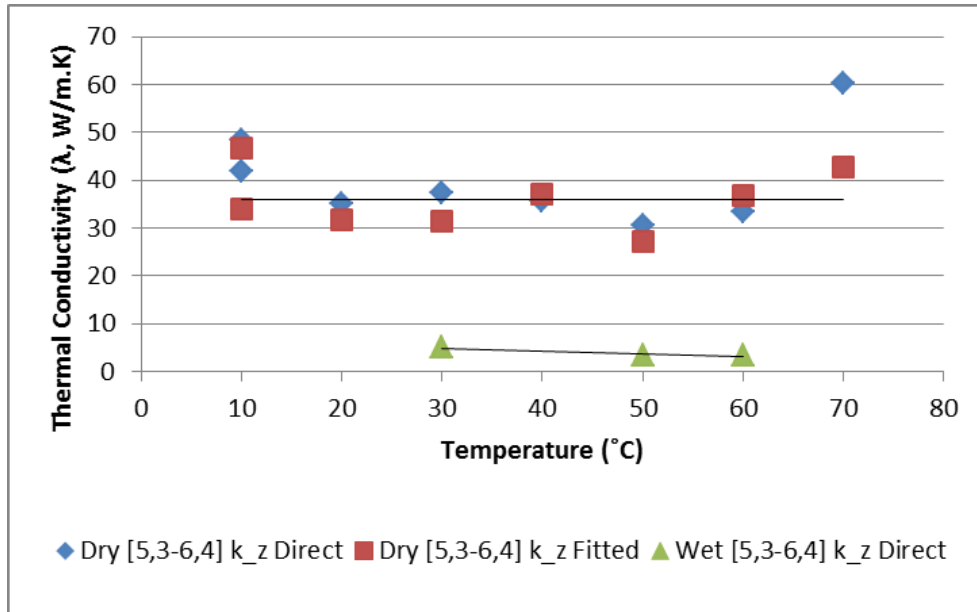


Figure 6-10: Thermal conductivity results obtained for the dry and wet, hexagonal (i.e. 194), graphite model with lattice vectors $a[5,0,0]$, $b[3,6,0]$ and $c[0,0,4]$. Only the direct integral values for inter-planar thermal conductivities along the “Z-axis” are shown for the wet graphite models.

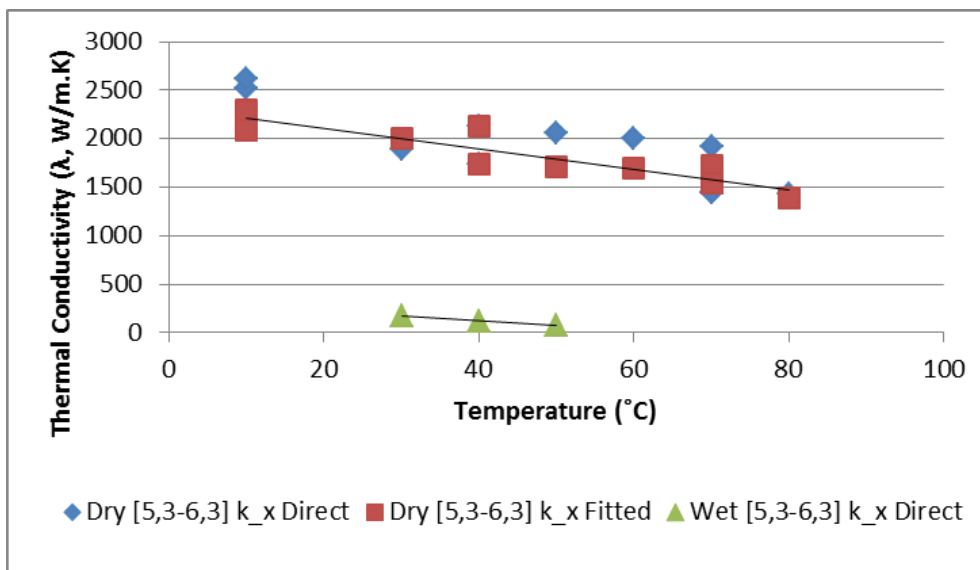


Figure 6-11: Thermal conductivity results obtained for the dry and wet, rhombohedral (i.e. 166), graphite model with lattice vectors $a[5,0,0]$, $b[3,6,0]$ and $c[0,0,3]$. Only the direct integral values for intra-planar thermal conductivities along the “X-axis” are shown for the wet graphite models.

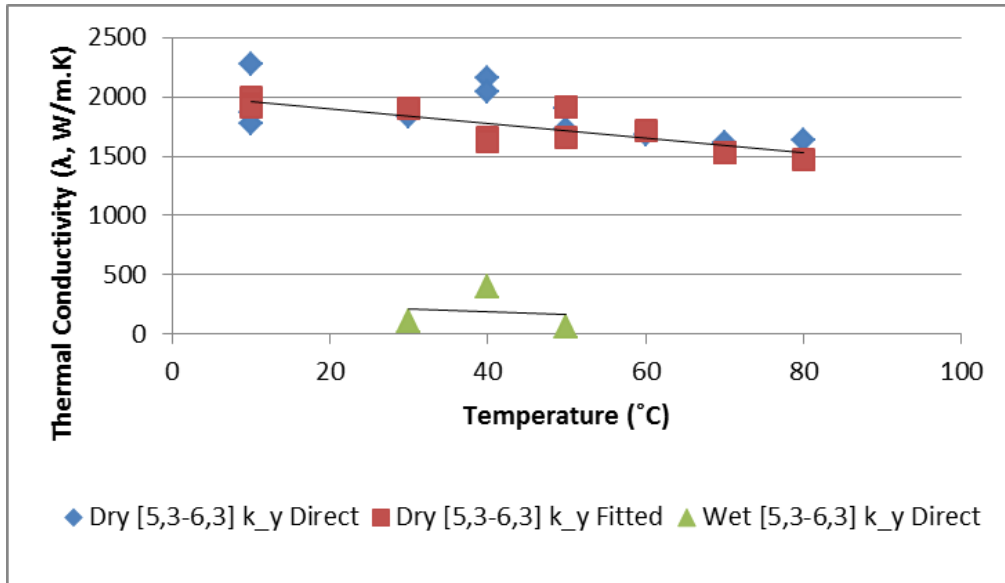


Figure 6-12: Thermal conductivity results obtained for the dry and wet, rhombohedral (i.e. 166), graphite model with lattice vectors $a[5,0,0]$, $b[3,6,0]$ and $c[0,0,3]$. Only the direct integral values for intra-planar thermal conductivities along the “Y-axis” are shown for the wet graphite models.

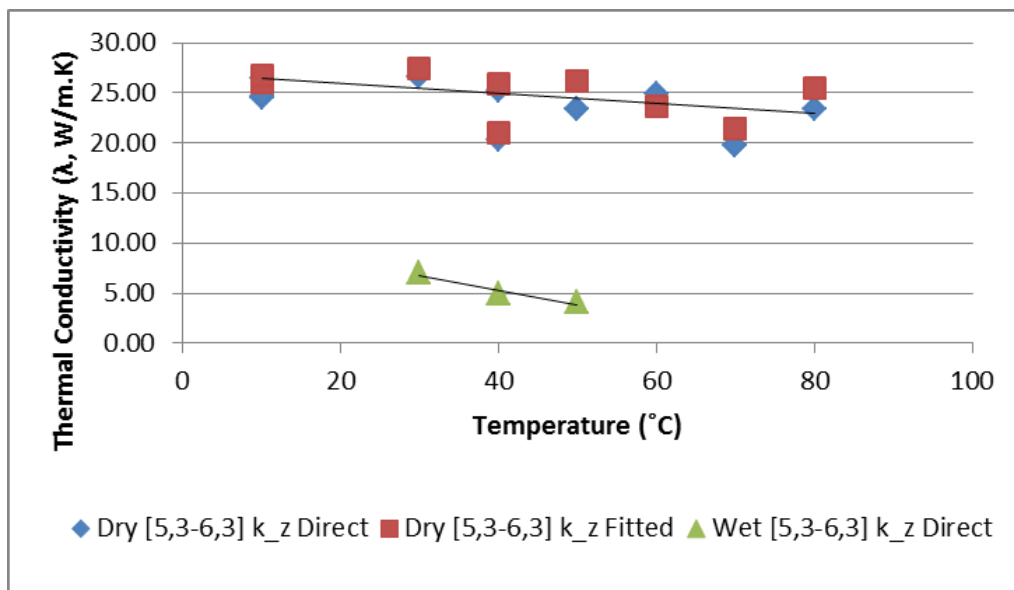


Figure 6-13: Thermal conductivity results obtained for the dry and wet, rhombohedral (i.e. 166), graphite model with lattice vectors $a[5,0,0]$, $b[3,6,0]$ and $c[0,0,3]$. Only the direct integral values for inter-planar thermal conductivities along the “Z-axis” are shown for the wet graphite models.

Intra-planar thermal conductivities were calculated to lie in the range of approximately 1500 to 2000 W/m.K for models with lattice vectors $\mathbf{a}[5,0,0]$ and $\mathbf{b}[3,6,0]$. When increasing the model size to lattice vectors $\mathbf{a}[7,0,0]$ and $\mathbf{b}[6,12,0]$, the thermal conductivity is calculated to be as low as 614 W/m.K. When only considering the average value of the calculated intra-planar thermal conductivities for all model sizes utilised, a value of approximately 1500 W/m.K is obtained.

Out-of-plane thermal conductivities are shown to be heavily dependent on the C-axis extension of the model. As the extension of the C-axis is increased from two repetitions to four repetitions, the calculated inter-planar thermal conductivity converges to a value of approximately 35 W/m.K. A comparison was made between inter-planar thermal conductivities produced using one model with lattice vectors $\mathbf{a}[5,0,0]$, $\mathbf{b}[3,6,0]$, $\mathbf{c}[0,0,2]$ and another larger model with lattice vectors $\mathbf{a}[7,0,0]$, $\mathbf{b}[6,12,0]$, $\mathbf{c}[0,0,2]$. From this comparison (refer to Annexure A) it can be seen that inter-planar thermal conductivities are heavily dependent on the intra-planar dimensions of the various models used. This is expected, as the EMD approach is known to be susceptible to finite size effects^{30,31}.

Table 6-8: Predicted thermal conductivities, for all dry hexagonal and rhombohedral models. The values reported below are the average values, calculated over the entire temperature range (refer to Annexure A for detail)

			Hexagonal space group – average (direct) λ , for entire temperature range			Rhombohedral space group – average (direct) λ , for entire temperature range			Avg. intra-planar	Avg. inter-planar
Direction of thermal energy transfer			λ_x	λ_y	λ_z	λ_x	λ_y	λ_z	λ_x/λ_y	λ_z
Transformation applied to unit cell										
a	b	c	W/m.K							
[7,0,0]	[6,12,0]	[0,0,2]	1 262	1 247	3.50	1 025	1 404	5.01	1235	4.26
[5,0,0]	[3,6,0]	[0,0,2]	1 664	1 601	25.76	1 741	1 752	26.94	1690	26.35
[5,0,0]	[3,6,0]	[0,0,3]	1 647	1 750	30.40	1 925	1 848	23.53	1792	26.96
[5,0,0]	[3,6,0]	[0,0,4]	1 914	1 869	40.37	-	-	-	1891	40.37

Although the thermal conductivities reported above all correlate with those of other authors (refer to Section 3.3.5), the wide range of reported values do not allow one to accurately predict the thermal conductivity of (dry) natural graphite nanopowders.

Table 6-9: Correlation of calculated (dry graphite) thermal conductivities (averaged over both space groups) to published figures also produced using computational modelling techniques

			Avg. calculated thermal conductivities		Published thermal conductivities					
			Avg. intra-planar	Avg. inter-planar	Hone, et al. (1999) ³²		Berber et al. (2000) ³³		Khadem and Wemhoff (2013) ³⁴	
Direction of thermal energy transfer			λ_x/λ_y	λ_z	λ_x/λ_y	λ_z	λ_x/λ_y	λ_z	λ_x/λ_y	λ_z
Transformation applied to unit cell										
a	b	c	W/m.K							
[7,0,0]	[6,12,0]	[0,0,2]	1235	4.26	1750-5800	NA	1000-3000	NA	450-800	9-55
[5,0,0]	[3,6,0]	[0,0,2]	1690	26.35						
[5,0,0]	[3,6,0]	[0,0,3]	1792	26.96						
[5,0,0]	[3,6,0]	[0,0,4]	1891	40.37						

Table 6-10: Correlation of calculated (dry graphite) thermal conductivities (averaged over both space groups) to published figures, produced using experimental techniques

			Avg. calculated thermal conductivities		Published thermal conductivities							
			Avg. intra-planar	Avg. inter-planar	Berman (1952) ³⁵		Liu et al. (2008) ³⁶		Wei et al. (2010) ³⁷		Prieto et al. (2011) ³⁸	
Direction of thermal energy transfer			λ_x/λ_y	λ_z	λ_x/λ_y	λ_z	λ_x/λ_y	λ_z	λ_x/λ_y	λ_z		
Transformation applied to unit cell												
a	b	c	W/m.K									
[7,0,0]	[6,12,0]	[0,0,2]	1235	4.26	200-300	50-80	351-568	74-80	100-600	5-15	499-523	27-38
[5,0,0]	[3,6,0]	[0,0,2]	1690	26.35								
[5,0,0]	[3,6,0]	[0,0,3]	1792	26.96								
[5,0,0]	[3,6,0]	[0,0,4]	1891	40.37								

The calculated thermal conductivities of each of the wet models are shown to be orders of magnitude lower than that of the dry graphite models. This is in line with the observation made using the heat capacitance measurements (performed using DSC). These measurements showed a decrease in the heat capacitance with the addition of water to the dry graphite samples, implying a lower thermal conductivity in comparison to dry graphite, due to the water molecules acting as “heat sinks” (refer to section 5.5), delaying the expulsion of thermal energy from the graphite surface(s).

6.6 SOURCES OF DISCREPANCY

From the data produced it is clear that measured thermal conductivities of natural polycrystalline graphite are significantly lower than those predicted using computational modelling techniques. The primary reason for this discrepancy may be attributed to the fact that computational modelling techniques utilise nano-scopic, periodic/crystalline, defect free structures at specific crystal-space densities, and not bulk densities, applicable to bulk graphite samples. Physical measurements made on graphite samples characterise the thermo-physical properties of macro-sized, polycrystalline, imperfect structures.

In most cases measurements made on bulk graphite samples involve the use of a chemical binder to form a solid graphite disk, utilised for physical measurement. The presence of the binder itself will have a significant effect on the overall thermo-physical properties of the sample.

Furthermore, when the thermal conductivities of bulk (polycrystalline) graphite samples are reported as being either intra-planar or inter-planar, this is by no means indicative of the thermal conductivity that would be expected when calculating the intra- and inter-planar thermal conductivities of a single graphite crystal.

By comparing the calculated thermal conductivities (produced using computational modelling) and the measured thermal conductivities of natural graphite, it is clear that each of the factors mentioned above further reduce the (intra- and inter-planar) thermal conductivities of each of the graphite crystallites that constitute the bulk, polycrystalline, graphite sample.

7. CONCLUSION

A complete structural characterisation of nano-scopic, natural, nuclear grade graphite was successfully performed, utilising multiple experimental techniques. From this, it was made clear that there is little understanding of the crystallographic structure of bulk natural graphite, which is still being debated to this day. This thesis has shown that if one is to completely characterise the structure of any nano-scopic sample, multiple structural characterisation techniques (such as the ones utilised in this thesis), are required.

Both dry and “wet” graphite models were successfully created and refined, utilising a combination of density functional theory and semi-empirical molecular dynamics. The thermal conductivity of each of the models created was then calculated, utilising the large-scale atomic/molecular massively parallel simulator (LAMMPS). The thermal conductivities calculated in this thesis, utilising “dry” models, are shown to be in-line with the computational results of other authors, with the in-plane and out-of-plane thermal conductivities calculated to lie in the range of 1000 to 2000 W/m.K and 3 to 40 W/m.K, respectively.

Calculated thermal conductivities of graphite intercalated with water molecules are shown to be orders of magnitude lower than that of the dry graphite models. Measurements made to determine the heat capacitance of both dry and wet graphite samples showed that the heat capacitance of wet graphite is reduced significantly in comparison to dry graphite. This may be interpreted as that wet graphite has a lower thermal conductivity as opposed to dry graphite, due to the water molecules acting as “heat sinks” (refer to section 5.5), delaying the expulsion of thermal energy from the graphite surface(s) and effectively “insulating” the graphite surface.

By comparing the calculated thermal conductivities and the thermo-physical measurements made using dry natural graphite, it is clear that several factors which distinguish the computational environment from the real-world scenario, further reduce the (intra- and inter-planar) thermal conductivities of graphite crystallites.

8. RECOMMENDATIONS

It is recommended that further experimentation takes place, utilising wet natural graphite samples, in order to further characterise the thermo-physical properties of “surface-wetted” natural graphite. This is to be done by means of differential scanning calorimetry (DSC), thermogravimetric analysis (TGA) and laser flash analysis (LFA). Such data regarding “surface-wetted” graphite samples (specifically those concerned with thermal conductivity) is currently unavailable and could constitute a second publication.

Once a detailed understanding of how the thermo-physical properties of graphite within a computational environment are related to those within the real world, only then can the investigation into the use of crystalline solids solvated within a (semi-electrolytic) fluid, begin.

9. REFERENCES

1. Choi, C., Jung, M. & Oh, J. Preparation and characterization of lubricating oil-based nanofluids containing carbon nanoparticles. *Korean J. Mater. Res.* **19**, 156–162 (2009).
2. Choi, C., Jung, M., Ahn, K. & Oh, J. Thermal and tribological properties of lubricating oil-based nanofluids. in *Soc. Tribol. Lubr. Eng. - 2008 Annu. Meet. Exhib. Ext. Abstr.* 1 (2008). at <<http://0-www.scopus.com.innopac.up.ac.za/record/display.url?view=basic&eid=2-s2.0-77954894548&origin=resultlist>>
3. Wang, J. J., Zheng, R. T., Gao, J. W. & Chen, G. Heat conduction mechanisms in nanofluids and suspensions. *Nano Today* **7**, 124–136 (2012).
4. Zhang, Z. & Lockwood, Frances, E. ENHANCING THERMAL CONDUCTIVITY OF FLUIDS WITH GRAPHITE NANOPARTICLES AND CARBON NANOTUBE. *WO Pat. WO/2003/106,600* (2003). at <<http://www.wipo.int/patentscope/search/en/WO2003106600>>
5. Zhu, H., Zhang, C., Tang, Y., Wang, J., Ren, B., Yin, Y. Preparation and thermal conductivity of suspensions of graphite nanoparticles. *Carbon N. Y.* **45**, 226–228 (2007).
6. Yu, W. & Choi, S. U. S. The role of interfacial layers in the enhanced thermal conductivity of nanofluids: A renovated Hamilton-Crosser model. *J. Nanoparticle Res.* **6**, 355–361 (2004).
7. Ferrari, A., Meyer, J., Scardaci, V., Casiraghi, C., Lazzeri, M., Mauri, F., Piscanec, S., Jiang, D., Novoselov, K., Roth, S., Geim, A. Raman Spectrum of Graphene and Graphene Layers. *Phys. Rev. Lett.* **97**, 1–4 (2006).
8. Roduner, E. *Nanosopic materials: size-dependent phenomena*. 285 (The Royal Society of Chemistry, 2006).
9. Pecharsky, V. & Zavalij, P. *Fundamentals of powder diffraction and structural characterization of materials*. 751 (Springer Science and Business Media, 2008). doi:10.1007/978-0-387-09579-0
10. Petersen, T., Yarovsky, I., Snook, I., McCulloch, D. G. & Opletal, G. Microstructure of an industrial char by diffraction techniques and Reverse Monte Carlo modelling. *Carbon N. Y.* **42**, 2457–2469 (2004).
11. Teplykh, A. E., Bogdanov, S. G., Dorofeev, Yu. A., Pirogov, A. N., Skryabin, Y. N., Makotchenko, V. G., Nazarov, A. S., Fedorov, V. E. Structural state of expanded graphite prepared from intercalation compounds. *Crystallogr. Reports* **51**, S62–S66 (2006).
12. DiJulio, D. D. & Hawari, a. I. Examination of reactor grade graphite using neutron powder diffraction. *J. Nucl. Mater.* **392**, 225–229 (2009).

13. Volkova, S., Il'icheva, O. M. & Kuznetsov, O. B. X-ray study of the graphite-bearing rocks from the Pestpaksha ore occurrence and structural features of graphite. *Lithol. Miner. Resour.* **46**, 363–368 (2011).
14. RRUFF. Graphite R050503 - RRUFF Database: Raman, X-ray, Infrared, and Chemistry. at <<http://rruff.info/Graphite/R050503>>
15. WYCKOFF, R. W. G. Crystal Structures. *Inter- Sci.* **1**, (1963).
16. Kwiecińska, B. & Petersen, H. . Graphite, semi-graphite, natural coke, and natural char classification—ICCP system. *Int. J. Coal Geol.* **57**, 99–116 (2004).
17. Gray, D., Mccaughan, A. & Mookerji, B. Crystal Structure of Graphite , Graphene and Silicon. *Phys. Solid State Appl.* **2**, 3–5 (2009).
18. Criddle, A. J. & Stanley, C. J. *Quantitative data file for ore minerals*. 211 (Chapman & Hall, 1993).
19. Trucano, P. & Chen, R. Structure of graphite by neutron diffraction. *Nature* 136–137 (1975).
20. Hatton, A., Engstler, M., Leibenguth, P. & Mücklich, F. Characterization of Graphite Crystal Structure and Growth Mechanisms Using FIB and 3D Image Analysis. *Adv. Eng. Mater.* **13**, 136–144 (2011).
21. Kaneko, K., Ishii, C., Ruike, M. & Kuwabara, H. Origin of superhigh surface area and microcrystalline graphitic structures of activated carbons. *Carbon N. Y.* **30**, 1075 (1992).
22. Kaneko, K. & Ishii, C. Superhigh surface area determination of microporous solids. *Colloid Surfaces* **67**, 203 (1992).
23. Chen, G. *et al.* Preparation and characterization of graphite nanosheets from ultrasonic powdering technique. *Carbon N. Y.* **42**, 753–759 (2004).
24. Friedel, R. A. & Carlson, G. L. Difficult carbonaceous materials and their infra-red and Raman spectra. Reassignments for coal spectra. *Fuel* **51**, 194–198 (1972).
25. Vidano*, R. P., Fischbach, O. B., Willis, L. J. & Loehr, T. M. OBSERVATION OF RAMAN BAND SHIFTING WITH EXCITATION WAVELENGTH FOR CARBONS AND GRAPHITES. *Solid State Commun.* **39**, 1–4 (1981).
26. Ditmars, D. A., Ishihara, S., Chang, S. S., Bernstein, G. & Bureau, N. Enthalpy and Heat-Capacity Standard Reference Material : Synthetic Sapphire (a-A1 2 0 3) from 10 to 2250 K. *J. Res. Natl. Bur. Stand. Washingt.* **87**, 159–163 (1982).
27. Pradhan, N. R., Duan, H., Liang, J. & Iannacchione, G. S. The specific heat and effective thermal conductivity of composites containing single-wall and multi-wall carbon nanotubes. *Nanotechnology* **20**, 245705 (2009).

28. International Atomic Energy Agency (IAEA). Characterization, Treatment and Conditioning of Radioactive Graphite from Decommissioning of Nuclear Reactors. (2006). at <http://www-pub.iaea.org/MTCD/Publications/PDF/te_1521_web.pdf>
29. Materials Desing Inc. *Materials Design and Exploration Analysis Software User's Guide, ver. 2.13.6 - Theoretical Background*.(MEDEA, 2013).
30. Schelling, P. K., Phillpot, S. R. & Keblinski, P. Comparison of atomic-level simulation methods for computing thermal conductivity. *Phys. Rev. B* **65**, 144306 (2002).
31. MEDEA®. *MEDEA® 2.14*. 414 (2013).
32. Hone, J., Whitney, M., Piskoti, C. & Zettl, a. Thermal conductivity of single-walled carbon nanotubes. *Phys. Rev. B* **59**, R2514–R2516 (1999).
33. Berber, S., Kwon, Y. & Tomanek, D. Unusually high thermal conductivity of carbon nanotubes. *Phys. Rev. Lett.* **84**, 4613–6 (2000).
34. Khadem, M. H. & Wemhoff, A. P. Molecular dynamics predictions of the influence of graphite stacking arrangement on the thermal conductivity tensor. *Chem. Phys. Lett.* **574**, 78–82 (2013).
35. Berman, R. The thermal conductivity of some polycrystalline solids at low temperatures. *Proc. Phys. Soc. Sect. A* **1029**, (1952).
36. Liu, Z., Guo, Q., Shi, J., Zhai, G. & Liu, L. Graphite blocks with high thermal conductivity derived from natural graphite flake. *Carbon N. Y.* **46**, 414–421 (2008).
37. Wei, X. H., Liu, L., Zhang, J. X., Shi, J. L. & Guo, Q. G. Mechanical, electrical, thermal performances and structure characteristics of flexible graphite sheets. *J. Mater. Sci.* **45**, 2449–2455 (2010).
38. Prieto, R., Molina, J. M., Narciso, J. & Louis, E. Thermal conductivity of graphite flakes–SiC particles/metal composites. *Compos. Part A Appl. Sci. Manuf.* **42**, 1970–1977 (2011).
39. Matsumoto, K., Li, J., Ohzawa, Y., Nakajima, T., Mazej, Z., Zemva, B. Surface structure and electrochemical characteristics of natural graphite fluorinated by ClF₃. *J. Fluor. Chem.* **127**, 1383–1389 (2006).
40. Sun, G., Li, X., Qu, Y., Wang, X., Yan, H., Zhang, Y. Preparation and characterization of graphite nanosheets from detonation technique. *Mater. Lett.* **62**, 703–706 (2008).
41. Shi, H., Barker, J., Saidi, M. & Koksang, R. Structure and lithium intercalation properties of synthetic and natural graphite. *J. Electrochem. ...* **143**, 3466–3472 (1996).
42. Welham, N. & Williams, J. Extended milling of graphite and activated carbon. *Carbon N. Y.* **36**, 1309–1315 (1998).
43. Kohs, W., Santner, H. J., Hofer, F., Schrottner, H., Doninger, J., Barsukov, I., Buqa, H., Albering, J. H., Moller, K. C., Besenhard, J. O., Winter, M. A study on electrolyte interactions

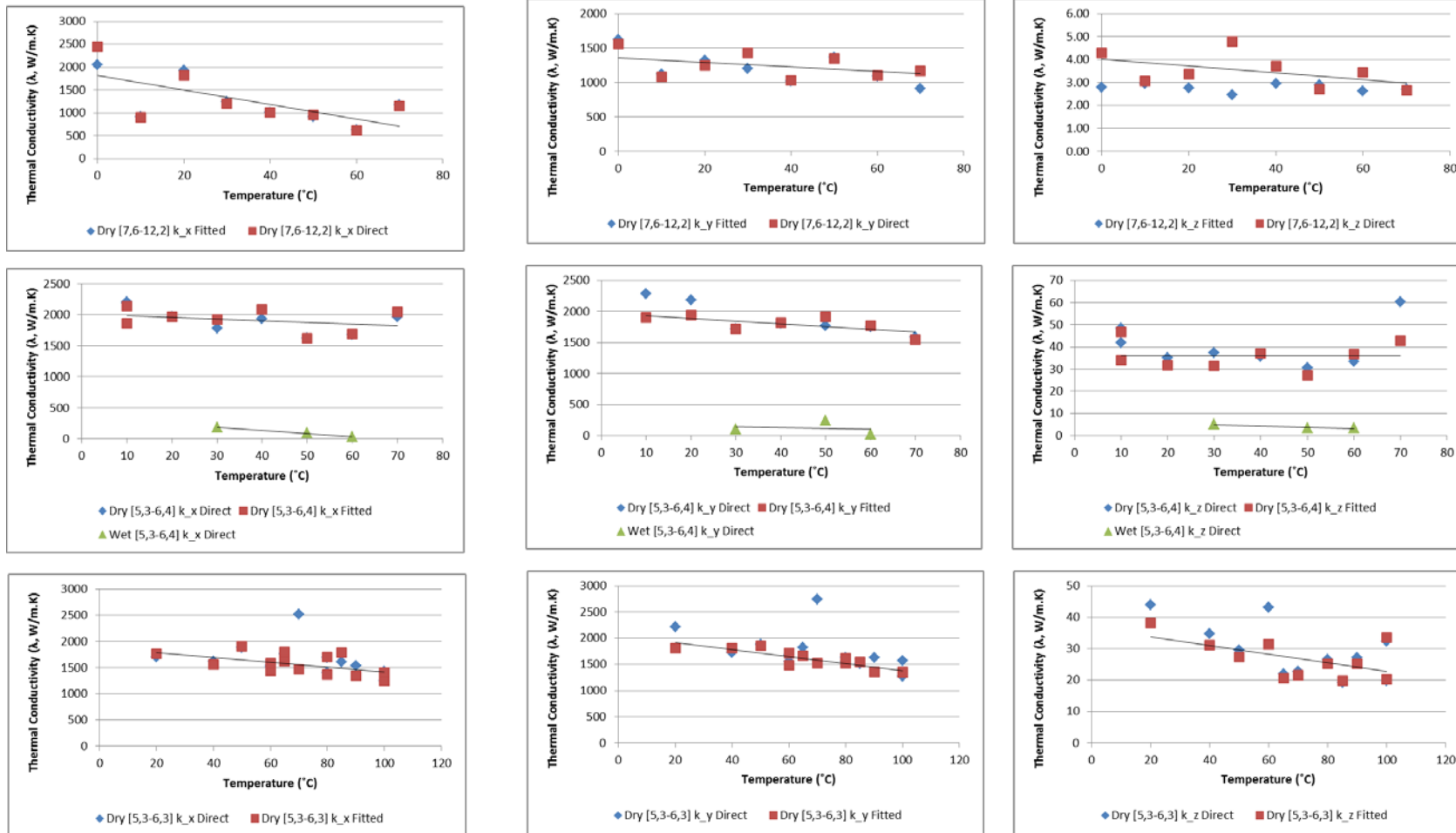
with graphite anodes exhibiting structures with various amounts of rhombohedral phase. *J. Power Sources* **119-121**, 528–537 (2003).

44. Lichty, P., Kreider, P., Kilbury, O., King, D., Weimer, A. W. Surface Modification of Graphite Particles Coated by Atomic Layer Deposition and Advances in Ceramic Composites. *Int. J. Appl. Ceram. Technol.* **10**, 257–265 (2013).

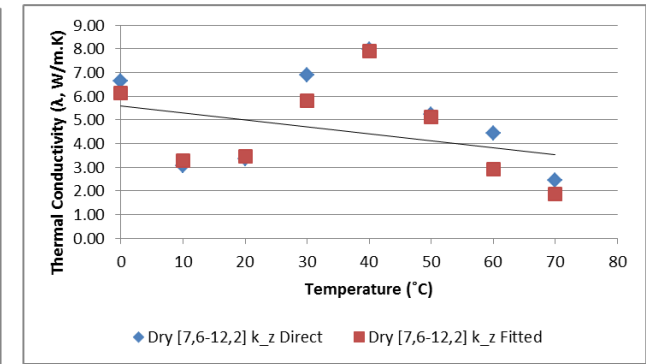
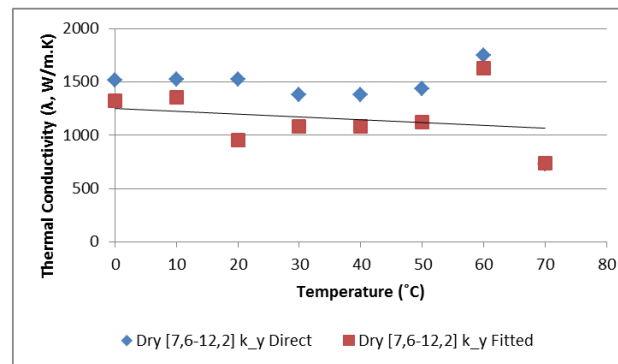
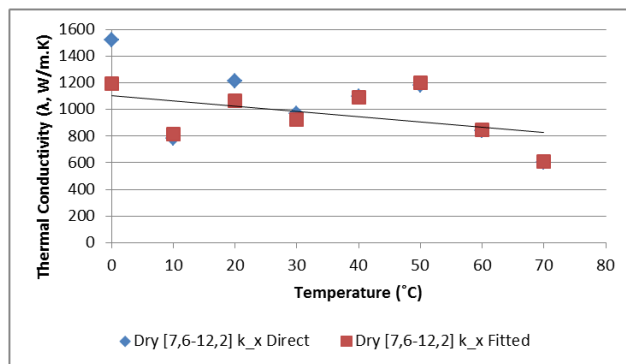
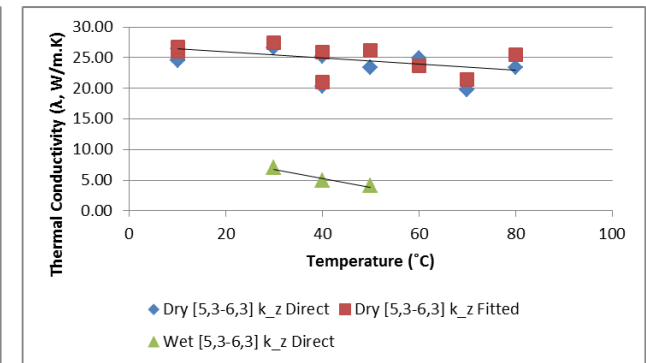
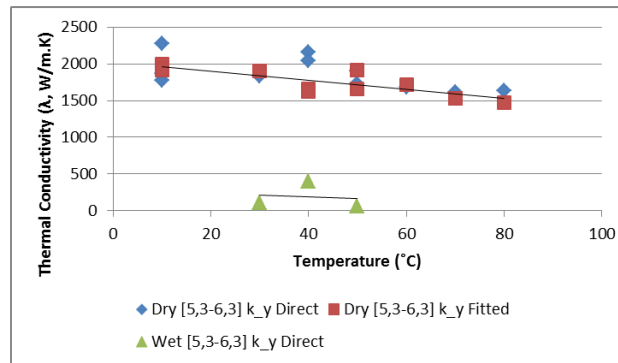
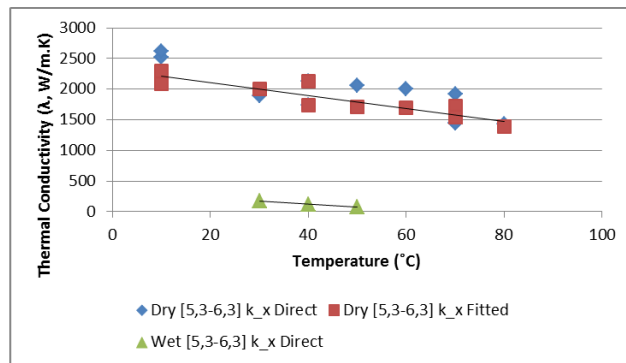
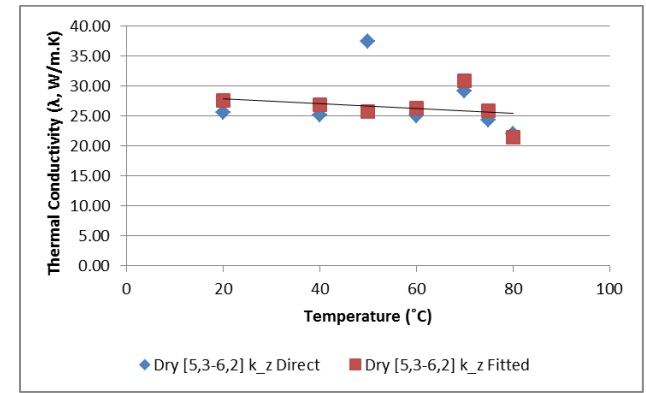
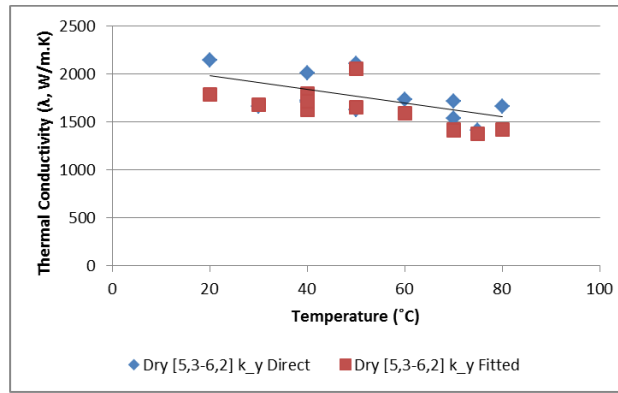
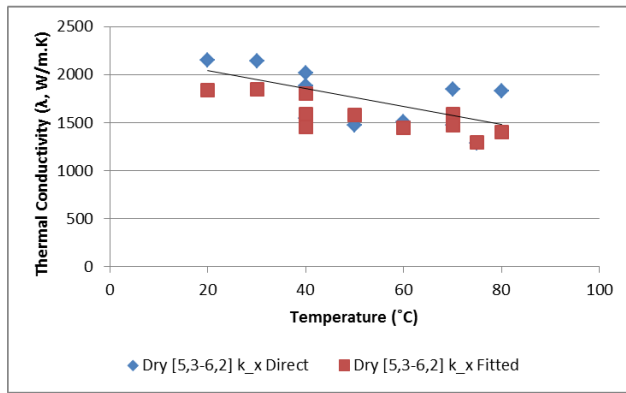
ANNEXURE

PART A – CALCULATED THERMAL CONDUCTIVITIES

Space group 194 (i.e. hexagonal) thermal conductivity results obtained through the use of computational modelling.

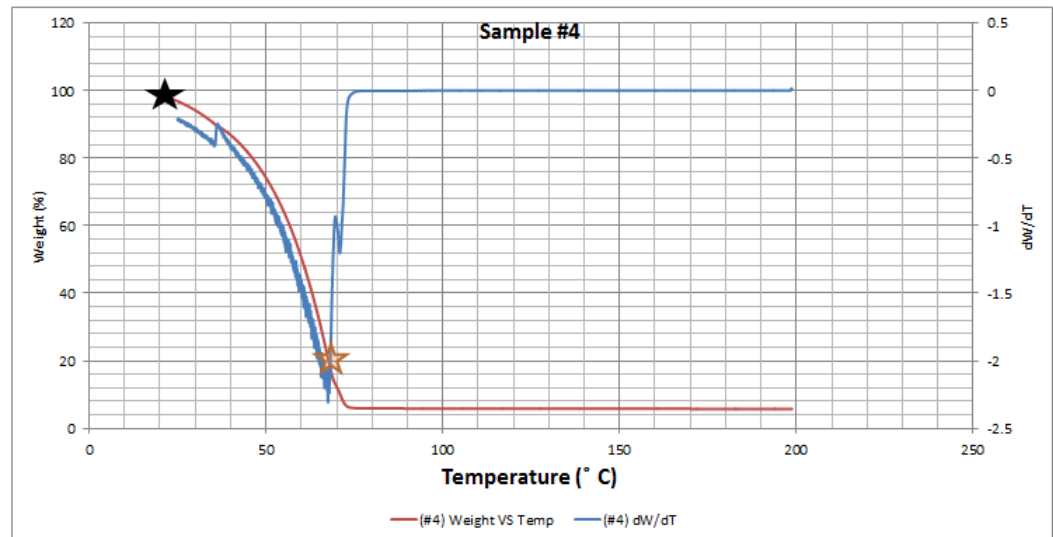
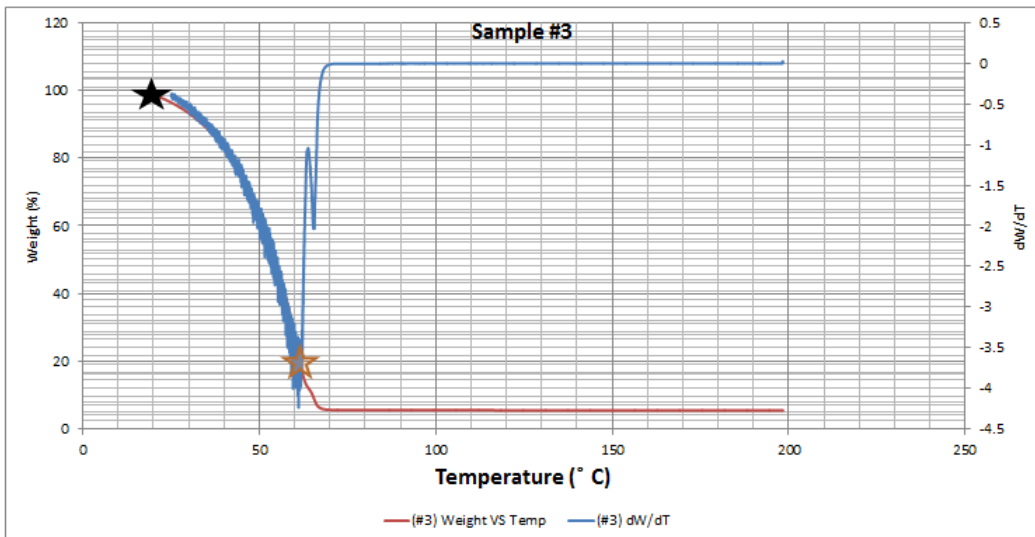
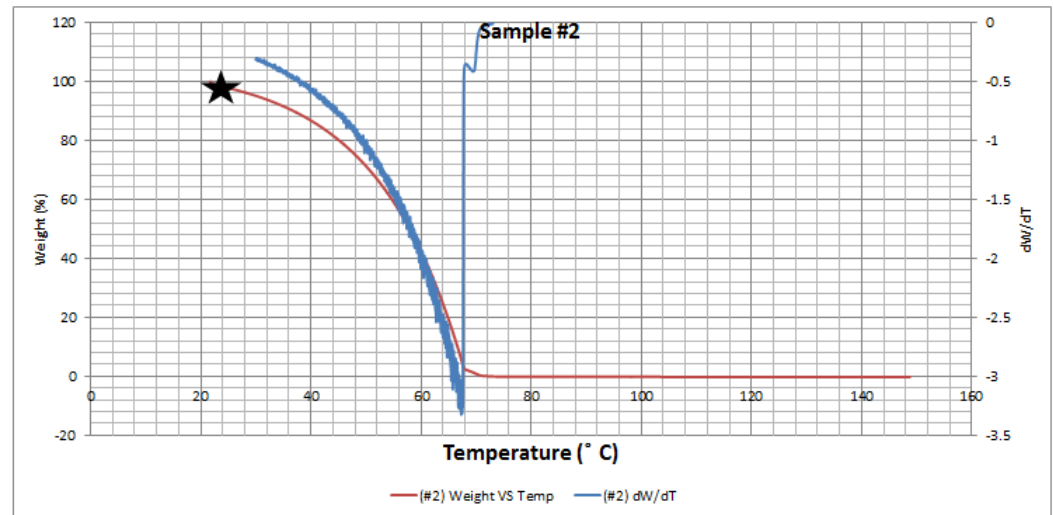
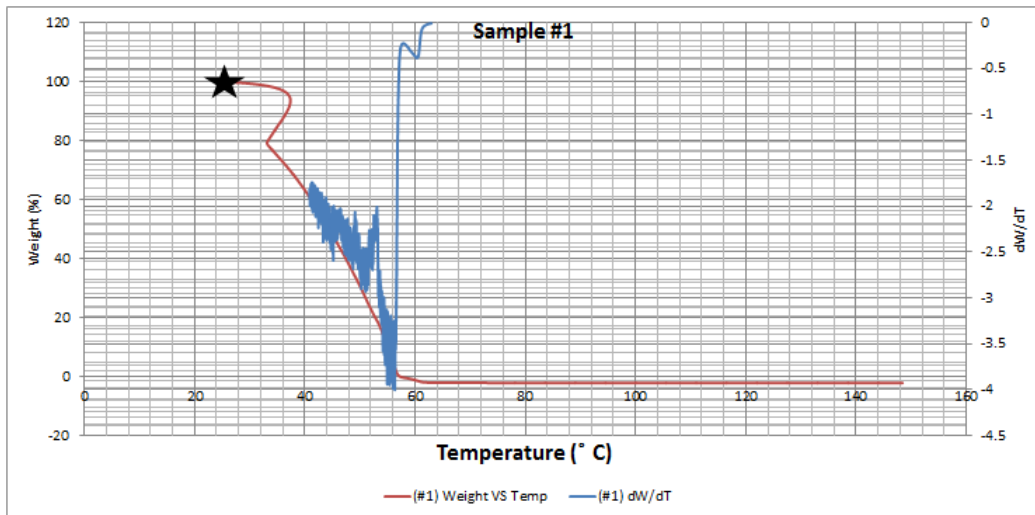


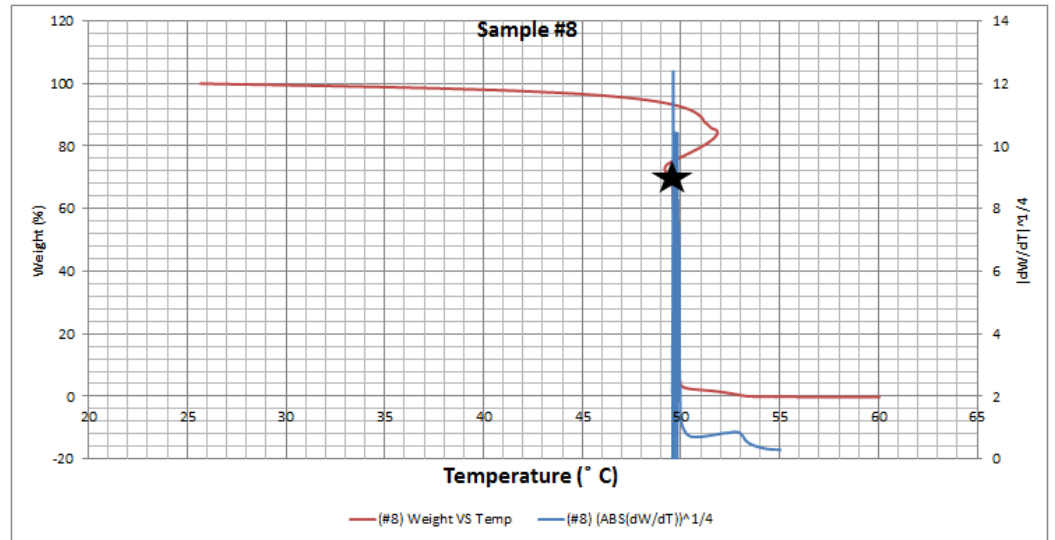
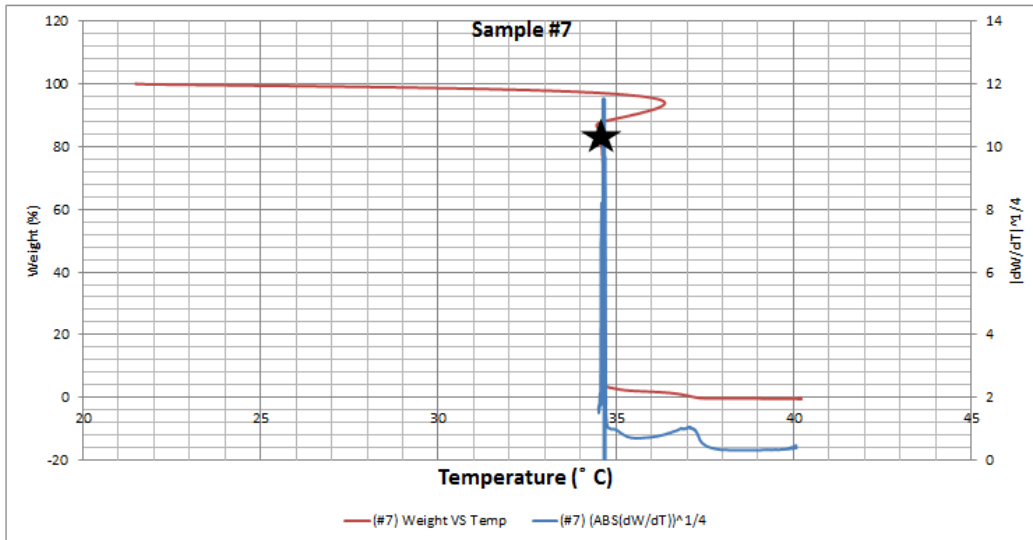
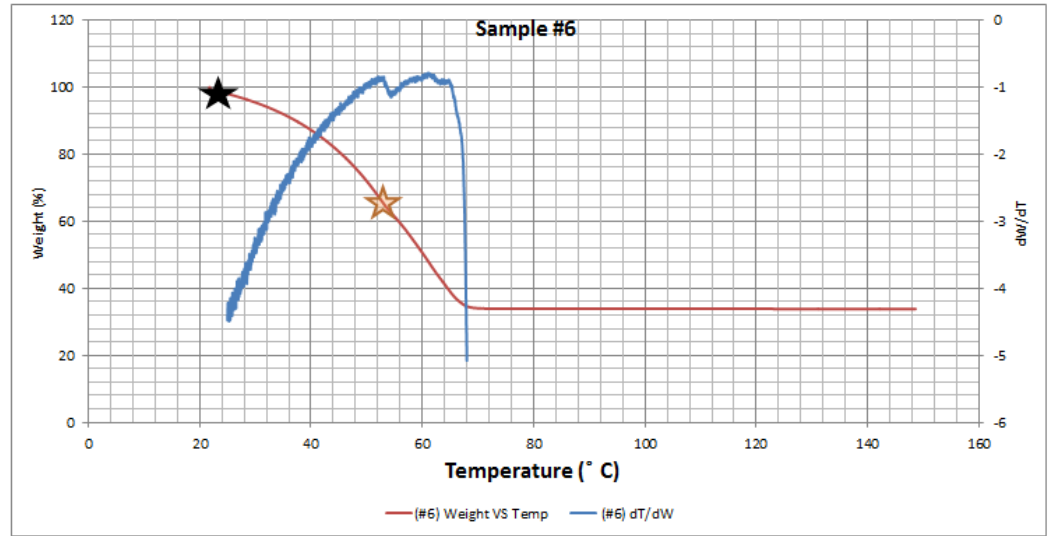
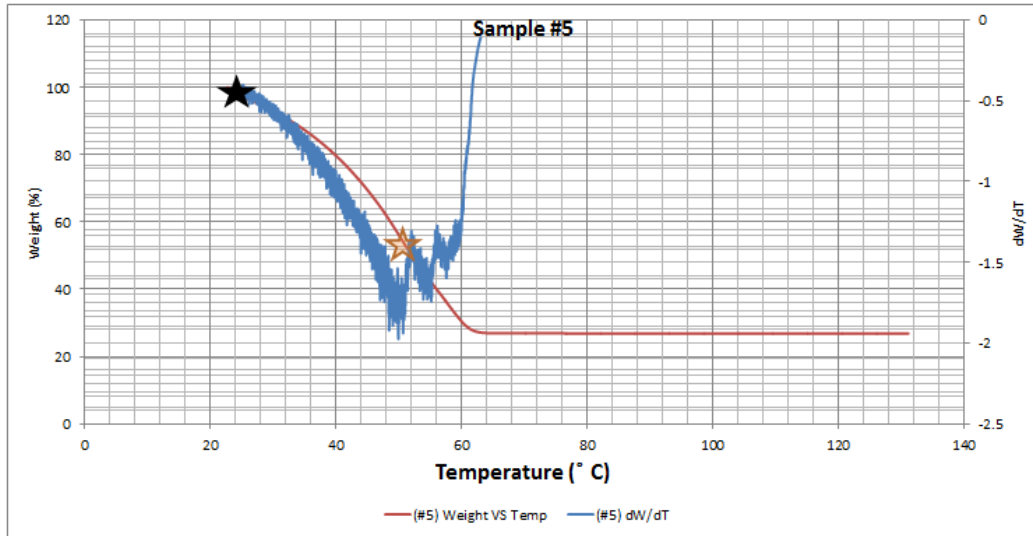
Space group 166 (i.e. rhombohedral) thermal conductivity results obtained through the use of computational modelling.

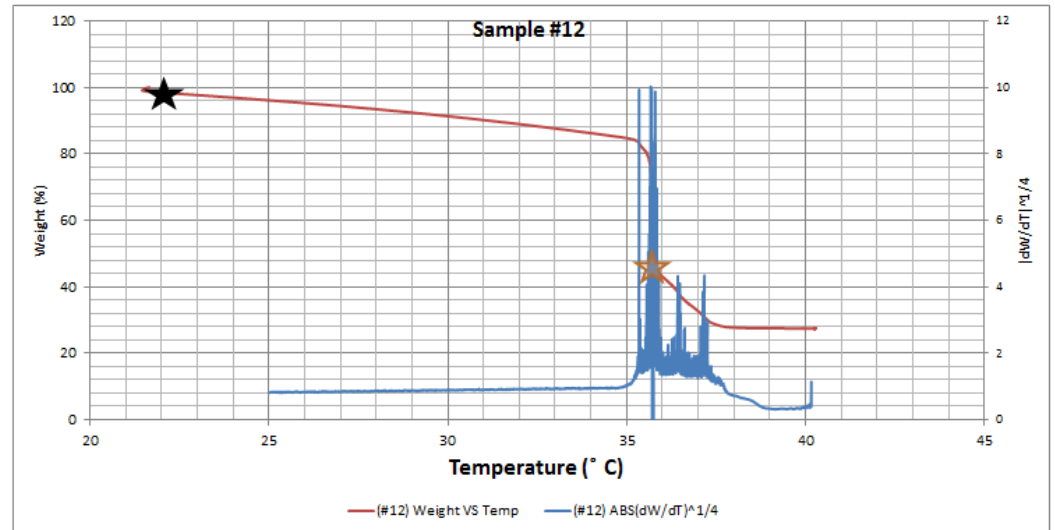
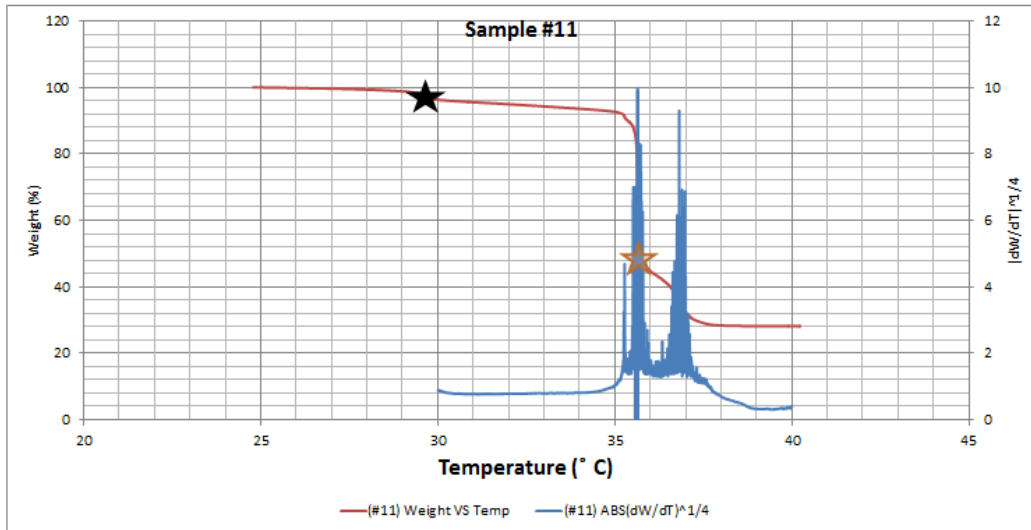
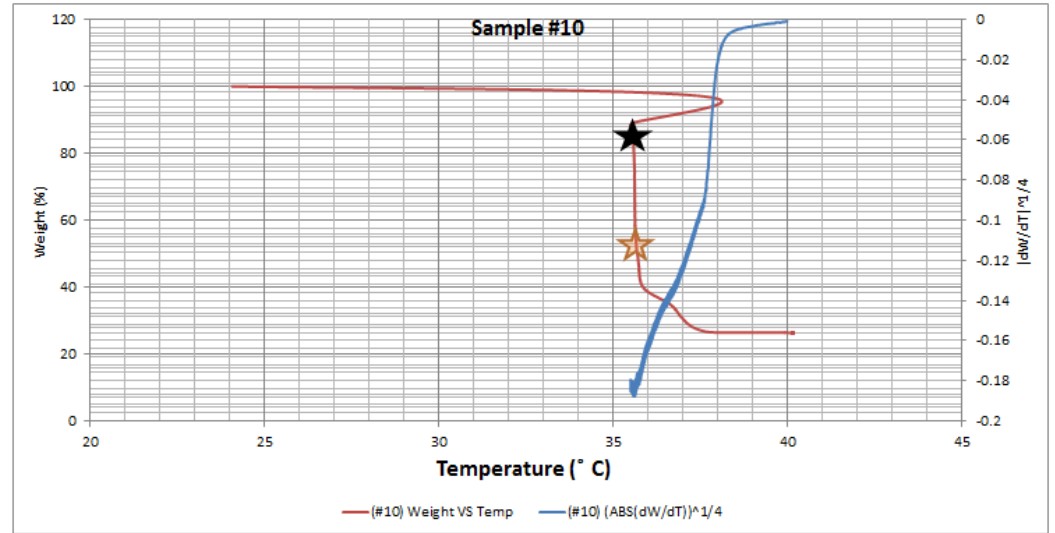
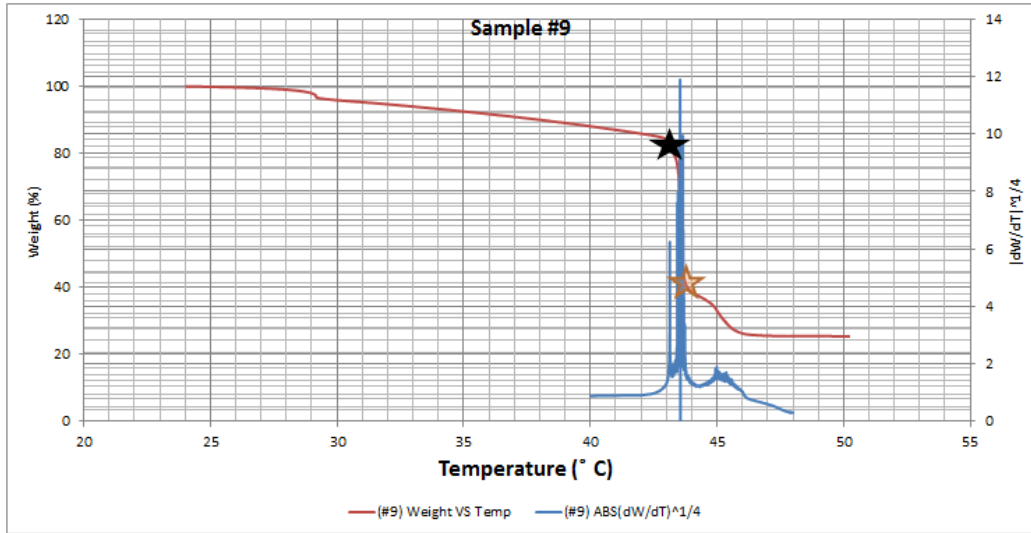


PART B – DIFFERENTIAL THERMO-GRAVIMETRIC ANALYSIS (DTGA) DATA PLOTS

★ Onset of bulk water expulsion ★ Offset of bulk water expulsion and onset of intercalated water expulsion







PART C – LASER FLASH APPARATUS LABORATORY PARAMETERS

Location: _____

Date: _____

Performed by: _____

Aim:

The aim of this experiment is to determine the thermal conductivity of multiple “surface-wetted” natural graphite samples.

Apparatus:

The Laser Flash Apparatus must operate in agreement with international standards such as DIN 30905 and DIN EN 821.

Instrument name: _____

Sample holder: Hermetically sealed, low-viscosity liquid sample holder (Fig. B-2)

Sample size: Diameter 10 to 13 mm and thickness 1 to 1.5 mm

Incident laser energy: > 20 J/pulse

Temperature measurement: Thermocouple or IR detection

Capabilities: Thermal diffusivity measurement

Methodology:

Calibration

Atmosphere: Air, helium or argon.

Atmospheric pressure: 1 bar

Temperature: Ambient to 80°C

Sample properties

Graphite:

Grade

Natural (99.98%), nuclear grade

Appearance

Black micro-powder

Hazard identification (Regulation (EC) No 1272/2008 [EU-GHS/CLP])

Eye irritation (Category 2)

Specific target organ toxicity - single exposure (Category 3)

Crystallographic structure (measured)

Hexagonal and rhombohedral

Particle size (measured)

16 to 20 μm

Thermal properties (literature)

The in-plane and out-of-plane thermal conductivity of natural polycrystalline graphite (at room temperature) has been estimated to lie in the range of 70-500 W/m.K and 1.5 to 38 W/m.K, respectively¹⁻⁵. The thermal diffusivity of Graphite is reported to lie in the range of 50 to 1000mm²/s, but is dependent on its density and crystal structure ⁶.

Water:

Quality

De-ionised, laboratory grade

Thermal properties (literature)

The thermal conductivity of water is known to lie in the range of 0.56 and 0.67 W/m.K, for a temperature range of 270 to 370 degrees Kelvin ⁷.

Samples for analysis

The samples stipulated in the table below are to be analysed. Each sample (or set of samples) is to be analysed at a specific temperature.

Table C-1: Sample compositions (containing de-ionised water and nuclear grade graphite) and measurement temperatures used in thermal conductivity measurement

Sample #	* ζ (mL H ₂ O/g NGG)	ζ (mL H ₂ O/mg NGG)	Measurement Temp. (°C)	Measurement Pressure (bar)	Repeats
1	0	0	30	1	X 1
2	0	0	40	1	X 1
3	0	0	50	1	X 1
4	0	0	60	1	X 1
5	0	0	70	1	X 1
6-10	0.67134	0.67	30	1	X 5
11-15	0.89178	0.89	40	1	X 5
16-20	1.12224	1.12	50	1	X 5
21-25	1.35270	1.35	60	1	X 5
26-30	1.57314	1.57	70	1	X 5

*Conversion based on water density at 20°C. ζ {mgH₂O / mg NGG} X 1.002 = ζ {mL H₂O / g NGG}

Sample preparation

Prior to the preparation of any sample, the (empty) sealed sample holder must be weighed and the mass noted. The volumetric capacity of the sample holder must also be determined and noted.

Dry samples (containers 1 to 5):

Dry graphite powder is to be placed in a sample holder that is capable of providing a hermetic seal. A sample holder such as those utilised for low-viscosity liquids is required. The material within the sample holder must be compressed, to ensure sufficient packing density. Compression of the sample material is to be performed manually, applying pressure using a flat (clean) glass plate. Sufficient material must be placed within the sample holder, such that a measurement sample with a diameter of 10 to 13 mm and thickness 1 to 1.5 mm (after compression) is obtained. The mass of the sealed, loaded, sample holder must be measured and noted. The mass of the empty sample holder must then be subtracted from the mass of the loaded sample holder. By using the calculated mass of sample material present in the sample holder and the volume of the sample holder, the density of the measurement sample is obtained.

Wet samples (containers 6 to 30):

Any sample container containing both graphite and water must be shaken vigorously (by hand) prior to their opening. This is to ensure a homogeneous mixture of water and graphite is placed within the sample holder. The same sample holder used for the analysis of the dry graphite samples (above) is required. Like the preparation of the dry samples, the wet sample material is to be manually compressed after being placed in the sample holder. HOWEVER, only a small amount of pressure is to be applied, using a flat hydrophobic surface to apply pressure. A microscope slide, either coated with epoxy or polytetrafluoroethylene (PTFE) ⁸, is recommended. Sufficient material must be placed within the sample holder, such that a measurement sample with a diameter of 10 to 13 mm and thickness 1 to 1.5 mm (after compression) is obtained. The density of the wet sample material which was loaded into the sample holder is to be determined in the same manner as for the dry graphite samples (above).

Theoretical background

A LFA involves the heating of a sample using a short laser pulse and the measurement of the rate at which the temperature on the reverse side of the sample (by either making use of an infrared camera or thermocouple), changes. This measurement is used to determine the thermal diffusivity (α) of the sample, using the $t_{1/2}$ method, where h is the sample thickness (in millimetres) and $t_{1/2}$ is the time (in seconds) taken for the rate of change in sample temperature to become constant. The thermal diffusivity of graphite is reported to lie in the range of 50 to 1000 mm²/s and is dependent on its density and crystal structure ⁹.

$$\alpha(T) \cong -\frac{\ln\left(\frac{1}{4}\right)}{\pi^2} \cdot \frac{h^2}{t_{1/2}(T)} \quad (\text{B-1})$$

With the density of the sample being known (by dividing the sample mass by the sample holder volume), the thermal conductivity is calculated as follows, with the density and heat capacitance being expressed using units of g/mm³ and J/g.K, respectively:

$$k(T) = \alpha(T) \cdot \rho(T) \cdot C_p(T) \quad (\text{B-2})$$

The density of the sample was considered to be constant during experimentation, as the sample was contained in a hermetically sealed sample holder.

Thermal measurement

The preparation and thermal analysis of wet graphite samples with a particularly high volume of water (numbers 21 to 30) must be carried out quickly and must not be left to stand for extended periods of time prior to measurement. If possible, the loaded sample holder must be shaken and inserted into the measurement chamber once it has reached thermal equilibrium. If this is not possible, the loaded sample holder must be shaken before it is placed inside the measurement chamber. This is done to prevent the sample from becoming a non-homogeneous mixture. Measurement of thermophysical properties are to be carried out in the following manner:

- i. It must be ensured that the measurement chamber reaches thermal equilibrium at the specified temperature (Table C-I).
- ii. Three consecutive measurements must be made. Each measurement must be made between three to five minutes apart.
- iii. Measurements of thermal diffusivity, α , and heat capacitance, C_p , are to be made on each of the samples. The thermal diffusivity is to be determined by means of the “ $t_{1/2}$ ” method.
- iv. From this data, the thermal conductivity is calculated.

$$k(T) = \alpha(T) \cdot \rho(T) \cdot C_p(T)$$

References

1. Liu, Z., Guo, Q., Shi, J., Zhai, G. & Liu, L. Graphite blocks with high thermal conductivity derived from natural graphite flake. *Carbon N. Y.* **46**, 414–421 (2008).
2. Prieto, R., Molina, J. M., Narciso, J. & Louis, E. Thermal conductivity of graphite flakes–SiC particles/metal composites. *Compos. Part A Appl. Sci. Manuf.* **42**, 1970–1977 (2011).
3. Wei, X. H., Liu, L., Zhang, J. X., Shi, J. L. & Guo, Q. G. Mechanical, electrical, thermal performances and structure characteristics of flexible graphite sheets. *J. Mater. Sci.* **45**, 2449–2455 (2010).
4. Wei, Z., Ni, Z., Bi, K., Chen, M. & Chen, Y. Interfacial thermal resistance in multilayer graphene structures. *Phys. Lett. A* **375**, 1195–1199 (2011).
5. Berman, R. The thermal conductivity of some polycrystalline solids at low temperatures. *Proc. Phys. Soc. Sect. A* **1029**, (1952).
6. Lichty, P. *et al.* Surface Modification of Graphite Particles Coated by Atomic Layer Deposition and Advances in Ceramic Composites. *Int. J. Appl. Ceram. Technol.* **10**, 257–265 (2013).

7. Ramires, M. L. . & de Castro, C. A. . Standard reference data for the thermal conductivity of water. *Am. Inst. Phys. Am. Chem. Soc.* (1995). at
<<http://scitation.aip.org/content/aip/journal/jpcrd/24/3/10.1063/1.555963>>
8. Thermo Fisher Scientific Inc. Diagnostic Slides. (2014). at
<<http://www.thermoscientific.com/en/product/diagnostic-slides.html>>
9. Lichty, P. et al. Surface Modification of Graphite Particles Coated by Atomic Layer Deposition and Advances in Ceramic Composites. *Int. J. Appl. Ceram. Technol.* 10, 257–265 (2013)

The information below is regarded as the property of the Thermoflow Research Group at The University of Pretoria, South Africa.



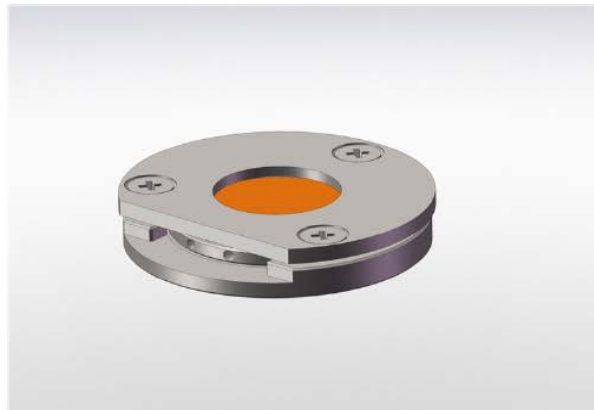
Date: 21/06/2014
Created By: Angelos Yiannou
Supervisor(s): Prof J Slabber, Dr J Pretorius & Prof J P Meyer
Contact: jannie.pretorius@up.ac.za ; a_yiannou@za.mhps.com

Note: The term "S.W.V" refers to a Specific Wetting Value. This value specifies the amount of water required, per gram of graphite, for the sample in question.

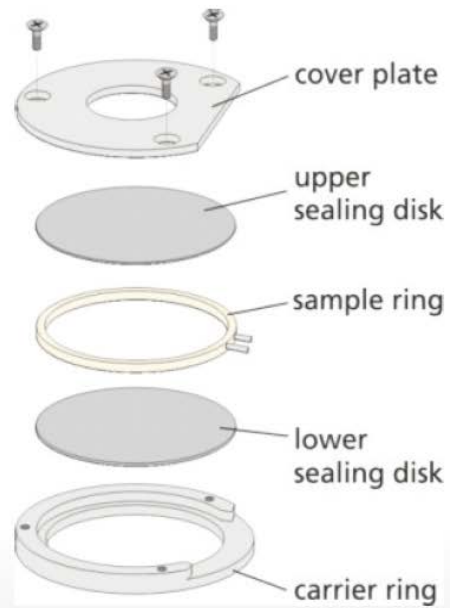
Sample Preparation Details																				
Set #	Sample #	Target S.W.V (mL H2O/g C)	S.W.V (g H2O/g C)	Empty bottle mass (no cap) (g)	Target Total Mass (g)	Actual Total Mass (g)	%Error	plus H2O (g) Target	Target Volume H2O (mL)	plus H2O (g) Actual	Actual Mass NGG present(g)	Actual Mass H2O added (g)	Target Mass H2O (g)	%Error (Mass H2O)	Actual S.W.V (g H2O/ g C)	% Error (S.W.V)	Measurement Temp (C)	Sample #		
Set 1	1	0	0	9.09	12.59	12.58	0.0794	12.5800	0.0000	12.5800	3.4900	0	0	0.0000	0.0000	0.0000	30.0000	1		
	2	0	0	9.27	12.77	12.77	0.0000	12.7700	0.0000	12.7700	3.5000	0	0	0.0000	0.0000	0.0000	40.0000	2		
	3	0	0	9.04	12.54	12.56	0.1595	12.5600	0.0000	12.5600	3.5200	0	0	0.0000	0.0000	0.0000	50.0000	3		
	4	0	0	9.39	12.89	12.9	0.0776	12.9000	0.0000	12.9000	3.5100	0	0	0.0000	0.0000	0.0000	60.0000	4		
	5	0	0	9.14	12.64	12.66	0.1582	12.6600	0.0000	12.6600	3.5200	0	0	0.0000	0.0000	0.0000	70.0000	5		
Set 2	6	0.67134	0.67	9.33	12.83	12.85	0.1559	15.2084	2.3631	15.1160	3.5200	2.266	2.3584	3.9179	0.6438	4.1097	30.0000	6		
	7	0.67134	0.67	9.31	12.81	12.83	0.1561	15.1884	2.3631	14.9190	3.5200	2.089	2.3584	11.4230	0.5935	11.5998	30.0000	7		
	8	0.67134	0.67	9.23	12.73	12.74	0.0786	15.0917	2.3564	15.0670	3.5100	2.327	2.3517	1.0503	0.6630	1.2478	30.0000	8		
	9	0.67134	0.67	9.07	12.57	12.56	0.0796	14.8983	2.3430	14.8730	3.4900	2.313	2.3383	1.0820	0.6628	1.2794	30.0000	9		
	10	0.67134	0.67	9.4	12.9	12.92	0.1550	15.2784	2.3631	15.2130	3.5200	2.293	2.3584	2.7731	0.6514	2.9671	30.0000	10		
Set 3	11	0.89178	0.89	9.1	12.6	12.59	0.0794	15.6961	3.1123	15.6540	3.4900	3.064	3.1061	1.3554	0.8779	1.5523	40.0000	11		
	12	0.89178	0.89	9.3	12.8	12.8	0.0000	15.9150	3.1212	15.8690	3.5000	3.069	3.115	1.4767	0.8769	1.6734	40.0000	12		
	13	0.89178	0.89	9.27	12.77	12.77	0.0000	15.8850	3.1212	15.8300	3.5000	3.06	3.115	1.7657	0.8743	1.9617	40.0000	13		
	14	0.89178	0.89	9.15	12.65	12.66	0.0791	15.7839	3.1301	15.7360	3.5100	3.076	3.1239	1.5333	0.8764	1.7299	40.0000	14		
	15	0.89178	0.89	9.23	12.73	12.73	0.0000	15.8450	3.1212	15.8430	3.5000	3.113	3.115	0.0642	0.8894	0.2637	40.0000	15		
Set 4	16	1.12224	1.12	9.04	12.54	12.56	0.1595	16.5024	3.9503	16.4400	3.5200	3.88	3.9424	1.5828	1.1023	1.7792	50.0000	16		
	17	1.12224	1.12	9.15	12.65	12.67	0.1581	16.6124	3.9503	16.5140	3.5200	3.844	3.9424	2.4959	1.0920	2.6906	50.0000	17		
	18	1.12224	1.12	9.15	12.65	12.66	0.0791	16.5912	3.9391	16.5600	3.5100	3.9	3.9312	0.7937	1.1111	0.9917	50.0000	18		
	19	1.12224	1.12	9.38	12.88	12.86	0.1553	16.7576	3.9054	16.7070	3.4800	3.847	3.8976	1.2982	1.1055	1.4952	50.0000	19		
	20	1.12224	1.12	9.27	12.77	12.77	0.0000	16.6900	3.9278	16.6420	3.5000	3.872	3.92	1.2245	1.1063	1.4216	50.0000	20		
Set 5	21	1.3527	1.35	9.06	12.56	12.55	0.0796	17.2615	4.7209	17.1450	3.4900	4.595	4.7115	2.4727	1.3166	2.6673	60.0000	21		
	22	1.3527	1.35	8.97	12.47	12.47	0.0000	17.1950	4.7345	17.1360	3.5000	4.666	4.725	1.2487	1.3331	1.4458	60.0000	22		
	23	1.3527	1.35	9.19	12.69	12.7	0.0788	17.4385	4.7480	17.3030	3.5100	4.603	4.7385	2.8596	1.3114	3.0534	60.0000	23		
	24	1.3527	1.35	9.37	12.87	12.89	0.1554	17.6420	4.7615	17.5910	3.5200	4.701	4.752	1.0732	1.3355	1.2707	60.0000	24		
	25	1.3527	1.35	9.12	12.62	12.61	0.0792	17.3215	4.7209	17.2350	3.4900	4.625	4.7115	1.8359	1.3252	2.0319	60.0000	25		
Set 6	26	1.57314	1.57	9.29	12.79	12.78	0.0782	18.2593	5.4903	18.1800	3.4900	5.4	5.4793	1.4473	1.5473	1.6440	70.0000	26		
	27	1.57314	1.57	9.1	12.6	12.59	0.0794	18.0693	5.4903	17.9500	3.4900	5.36	5.4793	2.1773	1.5358	2.3725	70.0000	27		
	28	1.57314	1.57	9.37	12.87	12.89	0.1554	18.4164	5.5375	18.2980	3.5200	5.408	5.5264	2.1424	1.5364	2.3378	70.0000	28		
	29	1.57314	1.57	9.34	12.84	12.84	0.0000	18.3350	5.5060	18.2100	3.5000	5.37	5.495	2.2748	1.5343	2.4699	70.0000	29		
	30	1.57314	1.57	9.16	12.66	12.66	0.0000	18.1550	5.5060	18.0290	3.5000	5.369	5.495	2.2930	1.5340	2.4880	70.0000	30		
MAX							0.1595	Average				3.504666667	MAX % Error				11.4230	MAX % Error		11.5998
								Deviation				0.01231079								

Figure C-1: Samples prepared for LFA measurement

NGB - Application Note 0 12 Part 1 - E - 01/12 - Technical specifications are subject to change.



1 Sample holder for low-viscosity liquids



2 Setup of the sample holder

1|2 NETZSCH-Gerätebau GmbH
Wittelsbacherstraße 42 · 95100 Selb · Germany
Tel.: +49 9287/881-0 · Fax: +49 9287/881505
at@netsch.com · www.netsch.com

NETZSCH

Figure C-2: Low viscosity liquid sample holder utilised in LFA measurements

PART D – BRIEF OUTLINE OF THE EMD APPROACH

The flow chart below describes the mathematical approach used to calculate the thermal conductivity of crystal structures using Equilibrium Molecular Dynamics (EMD) and the Green-Kubo approach.

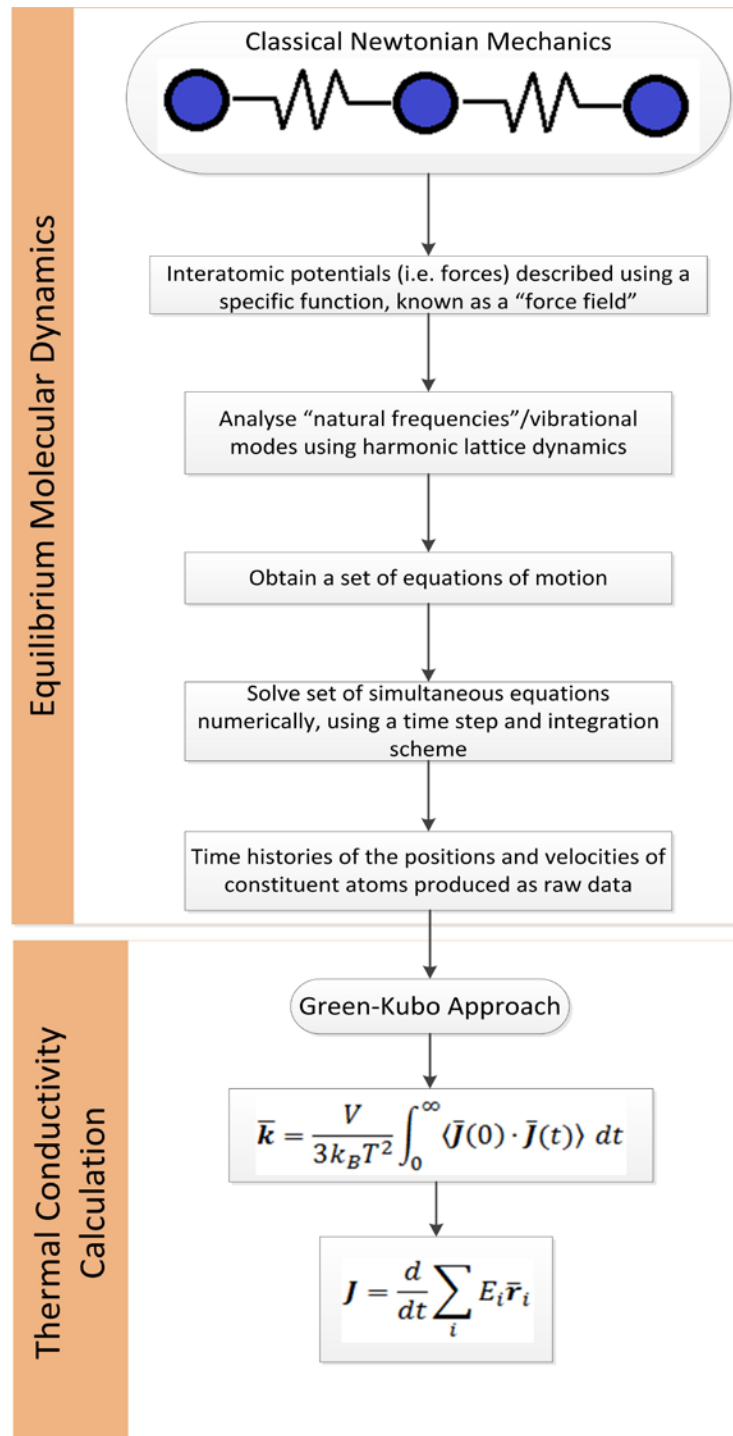


Figure D-1: Flowchart outlining the computational and mathematical approach to calculating the thermal conductivity of crystal structures, using Equilibrium Molecular Dynamics

In the flowchart of Figure D-1, the thermal conductivity vector is denoted by the symbol \mathbf{k} , the volume of the cell, V , the temperature of the atoms in the cell, T , and the heat current vector denoted by the symbol \mathbf{J} . The heat current vector is then described by a time dependant summation/integration of the total energy, E , multiplied by the displacement, \mathbf{r} , of each atom in the cell. The positions and the total (potential and kinetic) energy of each atom are obtained from the raw data produced by the EMD analysis of the structure.

A model size sufficient in all directions must be used, in particular in the direction perpendicular to the planar surface of the graphite crystal, in order for convergence of the heat current autocorrelation function, $\langle \bar{\mathbf{J}}(0) \cdot \bar{\mathbf{J}}(t) \rangle$.

Using equation B-2 of annexure C, the thermal conductivity calculated in the EMD simulation may be converted into a heat capacitance value. This calculated value can then be compared to the heat capacitance results produced by the DSC analysis of section 4.5, offering a direct correlation between molecular modelling and physical experimentation.